Bolometric detectors for EBEX: a balloon-borne cosmic microwave background polarimeter

A THESIS
SUBMITTED TO THE FACULTY OF THE GRADUATE SCHOOL
OF THE UNIVERSITY OF MINNESOTA
BY

Johannes Hubmayr

IN PARTIAL FULFILLMENT OF THE REQUIREMENTS
FOR THE DEGREE OF
Doctor Of Philosophy

December, 2009

Acknowledgements

This thesis would not exist without the help, tireless effort and inspiration of many people. I would like to acknowledge my thesis advisor Shaul Hanany, who warned me that "experimental physics is pain," but also demonstrated the rewards of this line of work. He taught me that progress is the result of dedication and the number of hours spent in the lab. His attention to detail is unparalleled. In addition, Shaul is one of the best public speakers I have seen and has transferred this knowledge to me. Whenever I am complimented on a presentation, it is the result of his teaching.

I would like to thank the entire EBEX collaboration. I believe our sense of family is something to be valued and aids our ability to work constructively together. No more clearly was this seen than in the EBEX field campaign. In Chappy's crane antics, Shaul and Ilan's skills on the cherry picker, Michael's bread, Kevin's daily hypothetical question starting "if the success of EBEX depended on..." and countless, tasteless jokes from everyone, we showed a camaraderie that made work fun. As a result, the two months of +14 hour work days breezed by and culminated in a successful test flight.

Trevor Lanting shared his knowledge of bolometers and frequency domain multiplexing in my first year working with the system. His time is greatly appreciated in that it accelerated my development of this system for EBEX. Matt Dobbs provided support throughout my thesis project, and to him I am very grateful. Kate Raach and François Aubin helped take the data that resulted in chapter 7 of this thesis. Thank you both.

On a personal level, I would like to acknowledge the love and support of my parents, sister and my wife Laura. Over Thanksgiving, we had a conversation on what makes a genius. I claimed genius can be developed with hours of work, while others thought it was something innate. The following day, after working on this thesis all day, my dad jokingly told me that the family decided I was, in fact, *not* a genius because I worked too much. I'll keep trying Dad.

Dedication

To all those that make use of this information. I wrote this for you.

Abstract

We discuss the design and performance of arrays of millimeter-wave, bolometeric detectors for EBEX, the E and B Experiment. EBEX is a balloon-borne telescope designed to measure the polarization in the cosmic microwave background (CMB) radiation with 8 arc-minute resolution at 150, 250 and 410 GHz during a 14-day long duration balloon flight in Antarctica. On June 11, 2009 EBEX launched an engineering test flight from NASA's Columbia Scientific Ballooning Facility (CSBF) achieving $\sim$ 10 hours at float altitudes of $\sim$ 115,000 ft. EBEX is the first experiment to successfully operate transition edge sensor (TES) bolometers read-out by superconducting quantum interference devices (SQUIDs) from a balloon platform. We present the EBEX instrument design, review TES bolometer and SQUID theory of operation and elaborate on frequency domain multiplexing. Following the analysis of the detector and readout system, we detail measurements that characterize the bolometers and conclude with a discussion of the EBEX receiver optical efficiency and in-flight bolometer loading during the engineering flight.

Contents

List of Tables

List of Figures

Chapter 1

Introduction

The era of precision cosmology, in which cosmological parameters are determined with an uncertainty better than 1%, is a reality. Enabled by advances in instrument technology, the results from precise astrophysical measurements have revolutionized our understanding of the universe. The expanding cosmos is in large part filled with unfamiliar forms of matter. Dark matter and dark energy form 96% of the energy content of the universe, whereas ordinary matter comprises only 4%. The source of all structure in the universe is thought to be due to quantum fluctuations in the first 10^{-34} seconds after the big bang that expand at super-luminal speeds to astronomical scales in a period of inflation.

This thesis discusses a balloon-borne, bolometric experiment called the E and B EXperiment (EBEX) which aims to measure the polarization in the cosmic microwave background (CMB) radiation with the goal of detecting gravity waves produced during inflation. Such a measurement would provide an unambiguous signature of the inflation paradigm, determine the energy scale of inflation and probe energy scales 13 orders of magnitude higher than state of the art terrestrial colliders at scales relevant for grand unified theories (GUTs).

1.1 Big bang, CMB and ΛCDM cosmology

Standard big band cosmology states that the universe began 13.7 billion years ago in a hot, dense singularity that has since expanded and cooled. The big bang theory has proven robust against a striking number of astrophysical observations: a dark night sky, the abundance and production of light elements [1, 2], receding galaxies [3] and the existence and properties of the cosmic microwave background (CMB) radiation.

The CMB is relic radiation from the big bang that permeates all space today as a 2.7 K background with an exquisite blackbody thermal spectrum [4]. Around $\sim$ 400,000 years after the big bang, the universe cooled enough to allow free electrons and protons to form neutral hydrogen. Light that had previously been tightly coupled to matter through frequent scattering was left to free stream largely unimpeded through the universe. This light is the CMB radiation that today provides a window into the physics of the early universe and is an invaluable probe of cosmology.

A host of impressive ground-based and balloon-borne experiments [5, 6, 7, 8, 9, 10, 11] measured small temperature fluctuations in the CMB that lead to the full sky measurement of NASA's Wilkinson Microwave Anisotropy Probe (WMAP) satellite [12] shown in Fig. 1.1. Cosmological models predict the statistical properties of the CMB via the angular power spectrum of such anisotropy maps (see Fig. 1.2). The CMB angular power spectrum is used to differentiate between cosmological models and together with supernova type IA and large scale structure observations has established the ΛCDM concordance model [13] for the contents and evolution of the universe. This model describes a flat universe filled with baryons, dark matter, neutrinos and a cosmological constant (Λ) with a nearly scale invariant spectrum of initial perturbations. The six free parameters of the concordance model fit the WMAP data well and are consistent will all other astrophysical observations, which span the 13 billion years of cosmic history.

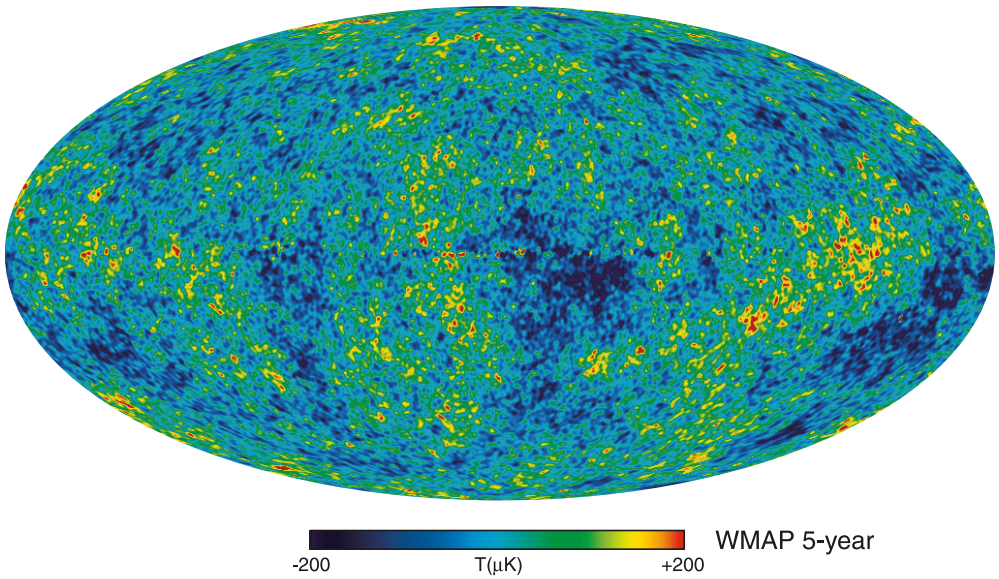

Figure 1.1: The full sky CMB temperature anisotropy measured by WMAP.

1.2 The inflation paradigm

Inflation naturally predicts several CMB observables that the standard big bang model falls short of explaining. Inflation theory posits a super-luminal, exponential expansion of space in the extremely early universe driven by a light scalar field [14, 15]. Such a phenomenon produces a spatially flat universe of almost uniform temperature with a near scale invariant spectrum of adiabatic, Gaussian fluctuations [16, 17]. We observe these fluctuations as the CMB temperature anisotropy and find that the amplitude of the fluctuations is the right size to produce the currently observed large scale structure in the universe.

Current data are consistent with inflation, but the details are poorly understood. The shape of the inflation potential is unknown as well as the energy scale, the age when inflation occurred. Theoretical arguments suggest that inflation may have occurred at energy scales relevant for the unification of the strong, weak and electromagnetic forces in a grand unified theory (GUT) [18]. Thus inflation is

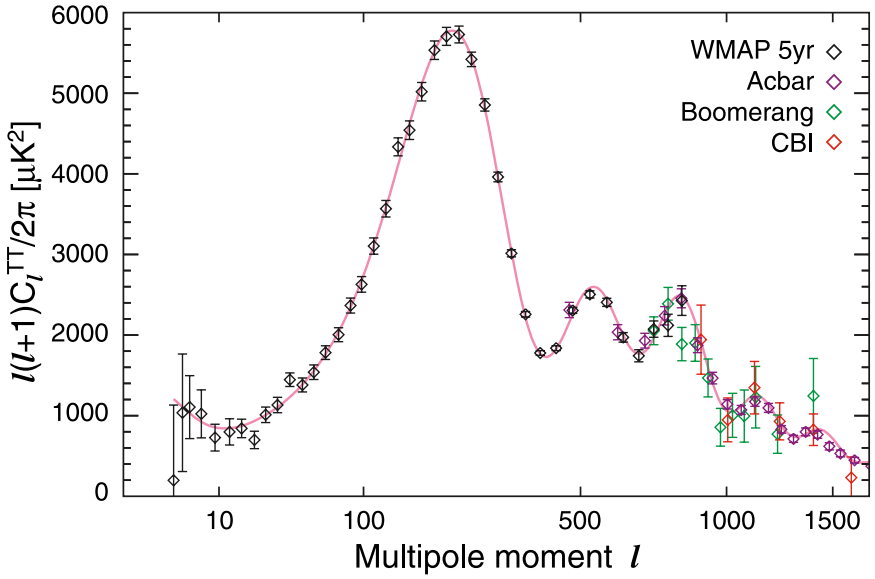

Figure 1.2: The angular power spectrum of CMB temperature anisotropy from WMAP.

fundamental to both physics and cosmology.

Fortunately, inflation has observational consequences. A generic prediction of inflation is the production of a stochastic background of gravity waves (ie tensor perturbations) that permeate all space akin to the CMB [19]. The amplitude of the gravity waves P_T is directly related to the inflation potential $V(\phi)$ [20],

$$P_T = \frac{2V(\phi)}{3\pi m_{pl}^4}, \tag{1.1}$$

where $m_{pl} = \sqrt{\hbar}c/G = 1.2 \times 10^{19}$ GeV/c^2 is the Planck mass. These gravity waves are predicted to imprint a distinct polarization signature in the CMB [21]. A detection of this signal or upper limits can constrain inflation models, reveal its energy scale and potentially probe GUT scale physics.

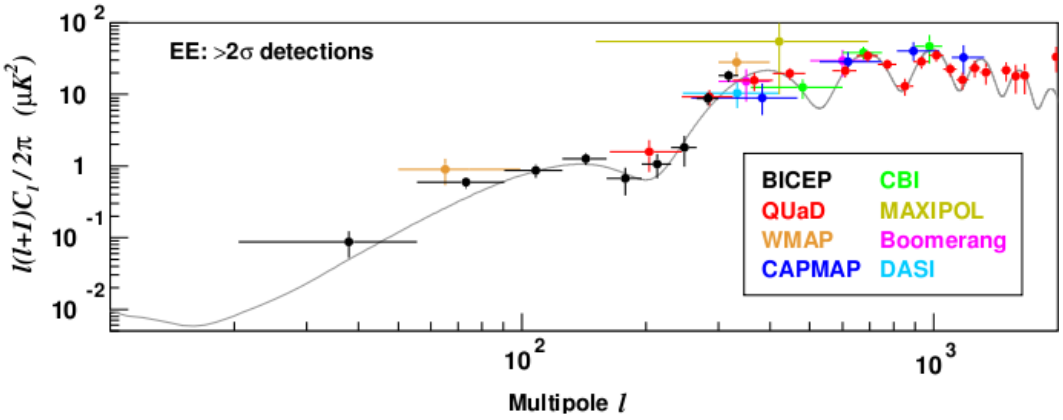

Figure 1.3: Current E-mode measurements from [29]

1.3 CMB polarization

The CMB is polarized through Thompson scattering of CMB photons at the surface of last scatter [22]. The polarization field can be decomposed into orthogonal components of curl free E-modes and divergence free B-modes [23]. This decomposition is useful because the source that generates these polarization patterns arise from different physical mechanisms. E-modes are produced by density perturbations present at the surface of last scatter, such as the temperature anisotropy. As such E-modes encode much of the same physics as the temperature anisotropy. Inflationary gravity waves produce equal parts E-mode and B-mode. Thus a detection of primordial B-modes is an unambiguous sign of inflation.

Just as a map of temperature produces an angular power spectrum, a polarization map generates E and B-mode power spectra. E-mode polarization at the $\sim \mu$K level have already been detected by a number of experiments [24, 25, 26, 27, 28, 29, 30], as shown in Fig. 1.3.

For perspective, Fig. 1.4 shows the temperature, E-mode and B-mode CMB power spectra on the same plot. The B-mode power spectrum generated by inflationary gravity waves peaks on degree angular scales at $\ell \sim 100$. B-modes provide

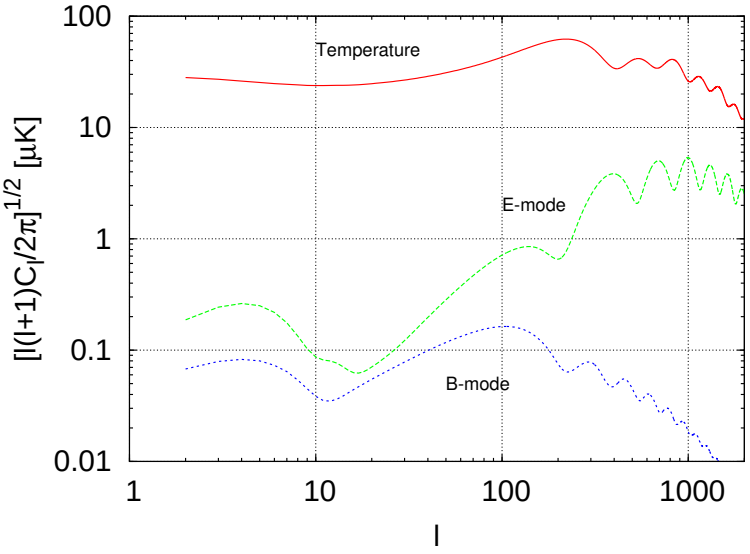

Figure 1.4: CMB temperature, E-mode and B-mode power spectra assuming concordance cosmology. The amplitude of the B-mode spectrum is set using the current upper-limits on the tensor to scalar ratio, $r < 0.22$ [32]. B-mode detection requires $\sim$ nK sensitivity.

a measure of the amplitude of tensor perturbations and therefore the energy scale of inflation $V^{1/4}$ through:

$$V^{1/4} = 2 \times 10^{16} (B_{\ell=90}/0.1\ \mu K)\ \text{GeV}. \tag{1.2}$$

The energy scale of inflation is currently unknown by at least 12 orders of magnitude [31].

The rewards of B-mode detection are high, but such measurements are extremely challenging due to the minute size of the signal in the presence of astrophysical foregrounds.

1.4 Detectors for balloon-borne approach

B-mode detection requires a *parts-per-billion* measurement which demand substantial technological development of millimeter-wave instruments capable of high sensitivity, fine control over systematic error and strong leverage against foreground contamination. Single bolometeric detectors have achieved sensitivity near the photon noise limit. As such, state of the art millimeter wave instruments employ large focal planes filled with thousands of fast, background limited detectors for increased sensitivity and mapping speed. The superconducting transition edge sensor (TES) bolometer is a promising detector choice because of its large responsivity, increased dynamic range and ease of fabrication into large arrays.

This thesis concerns the development and deployment of arrays of spider-web TES bolometers for the E and B experiment (EBEX). EBEX is the first experiment to successfully operate TES bolometers in a space-like environment. The colder telescope temperatures and lower background loading of the balloon environment allows the opportunity for sensitivity gains by lowering the thermal conductance G of the bolometer, which will be discussed in Chapter 3. As such the EBEX bolometers are uniquely designed for a balloon-borne application.

1.5 Thesis overview

The following list summarizes the thesis outline.

- Chapter 2 describes the EBEX science goals, experimental approach and instrument design.
- Chapter 3 reviews transition edge sensor bolometer theory.
- Chapter 4 reviews superconducting quantum interference devices (SQUIDs) used to readout the bolometers.
- Chapter 5 discusses frequency domain multiplexing with the digital frequency domain multiplexing (DfMUX) readout electronics.

- In Chapter 6, we demonstrate proto-type EBEX bolometers designed for a balloon-borne experiment.
- Chapter 7 discusses characterizing measurements of the three bolometer wafers used in the North American flight (NAF) including thermal transport properties, responsivity, linearity and optical time constants.
- Chapter 8 details the NAF campaign including laboratory measurements of optical efficiency as well as in-flight bolometer loading.

Chapter 2

EBEX

The E and B EXperiment is a bolometeric, balloon-borne experiment designed to measure the polarization in the cosmic microwave background from degree to arc-minute scales. EBEX has successfully flown from NASA's Columbia Scientific Ballooning Facility in Ft. Sumner, NM on June 12, 2009. During this North American test flight (NAF), the payload stayed at $\sim$ 115,000 feet for $\sim$ 10 hours. We plan a 14 day, long duration balloon (LDB) flight over Antarctica in December 2010. In this chapter, we detail the science goals, experimental approach, LDB instrument design and describe the configuration for the NAF.

2.1 EBEX science goals

EBEX has four primary science goals: 1) detect or set strong upper limits on inflationary B-modes, 2) detect lensing B-modes, 3) determine the properties of polarized dust foregrounds and 4) decrease the uncertainty on a number of cosmological parameters.

Fig. 2.1 plots the concordance model E and B-mode polarization power spectra of the CMB with red points and error bars that show the projected sensitivity of EBEX given a 14-day LDB flight. The B-mode spectrum comes from two sources: inflationary gravity waves and lensing. The gravity wave signal peaks at $\ell \sim 100$

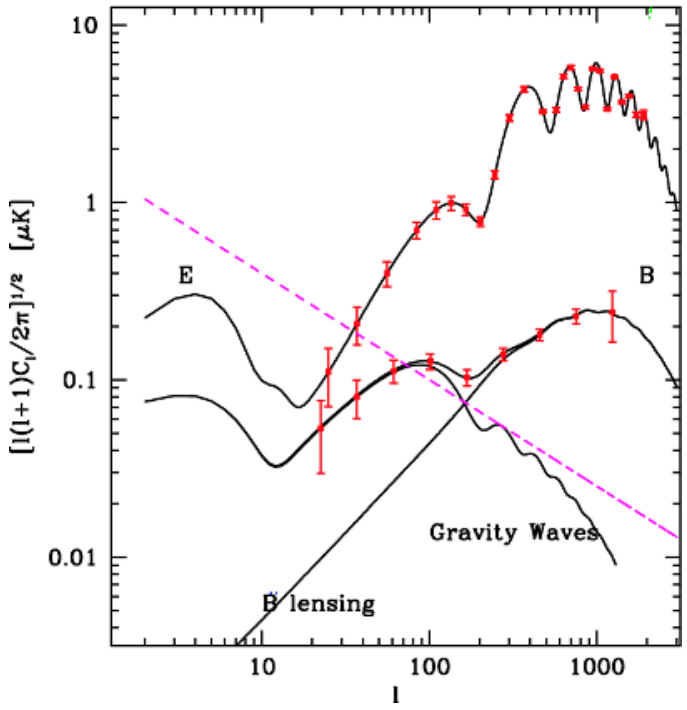

Figure 2.1: CMB polarization power spectra and expected EBEX sensitivity (red points and error bars). The B-mode prediction has two components: gravity waves (for which we assume $r = 0.1$ in this plot) and lensing. The dashed, pink line shows the expected level of dust foregrounds at 150 GHz in the EBEX observation area.

whereas the lensing B-modes peak at smaller angular scales around $\ell = 1000$.

The amplitude of the gravity wave B-mode signal is unknown and its determination provides a direct measure of the energy scale of inflation. The strength of the gravity waves is commonly parametrized by the tensor-to-scalar ratio $r \equiv C^T_{\ell=2}/C^S_{\ell=2}$. In Fig. 2.1, we have assumed $r = 0.1$ for illustration. If the tensor to scalar ratio is at this level, EBEX will detect inflationary B-modes with high signal to noise. Otherwise, EBEX will set a 2σ upper-limit on $r < 0.02$, which is a factor of 10 more stringent than the current upper limit set by WMAP [13, 32].

EBEX also aims to measure B-mode lensing. This robustly predicted signal

is currently undetected and results from the lensing of E-mode polarization into B-mode due to the matter along the photon line of sight. These measurements can be used to constrain the neutrino mass or set limits on the equation of state of dark energy [33]. Given the expected sensitivity, EBEX will determine the amplitude of the B-mode lensing power spectrum with 6% uncertainty.

An additional goal of EBEX is to determine the properties of polarized dust. The pink, dashed line in Fig. 2.1 shows the predicted level of B-modes produced by galactic dust foregrounds at 150 GHz in the EBEX sky patch. The prediction shows that even at high galactic latitudes, the dust level contents with the B-mode signal. Any B-mode experiment must characterize dust foregrounds in order to accurately recover inflationary B-modes. EBEX uses three frequency bands centered on 150, 250 and 410 GHz to characterize the spectrum of polarized dust foregrounds. With these frequency bands and the expected sensitivity, EBEX will determine the amplitude of the B-mode dust spectrum to within $\sim 6\%$ uncertainty.

Lastly, EBEX will make a cosmic variance limited E-mode measurement from $150 < \ell < 1500$ that will decrease the uncertainty on a number of cosmological parameters over the current values. For example, the uncertainty on the running of the scalar spectral index $d \ln n_s / d \ln k$ will decrease by a factor of four. Here n_s is the scalar spectral index and k is the co-moving wavenumber [34].

2.2 Experimental approach

The experimental approach to achieve these science goals follows three main design principles: high sensitivity, foreground discrimination and systematic error mitigation. High sensitivity is achieved with 1920[1] transition edge sensor (TES) bolometers and a 14 day LDB flight over Antarctica. EBEX will observe a ~ 400 deg^2 patch of sky in order to target the inflationary B-mode peak at degree angular scales while the optics produce $8'$ resolution in order to achieve sensitivity to the

[1] The number of bolometers is limited by detector readout and depends on the multiplexing factor (Sec. 2.3.6), which we assume is 16.

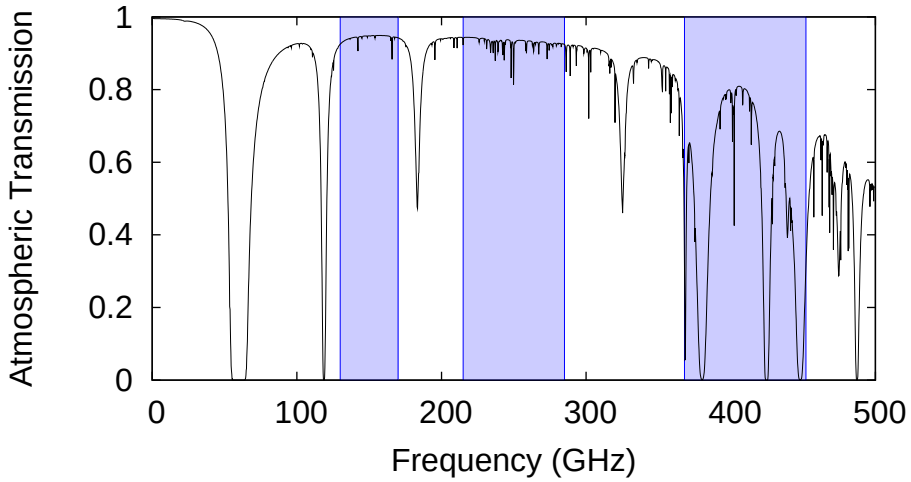

Figure 2.2: Model of zenith observation atmospheric transmission at the South Pole, one of the best ground-based, mm-wave observation sites. The model (from [36]) assumes 0.3 mm of perceptible water vapor. Atmospheric attenuation in EBEX observation bands (shaded regions) motivates a balloon-borne approach.

lensing signal. Three frequency bands centered on 150, 250 and 410 GHz that together span 120 to 450 GHz provide strong leverage on polarized dust foregrounds. This is the broadest frequency coverage of any sub-orbital CMB experiment to date. Foreground leverage motivates a balloon-borne approach because frequencies above 300 GHz are not accessible with ground-based observations (see Fig. 2.2). Systematic error mitigation is achieved with half wave plate (HWP) polarimetry which has strong heritage in astrophysics and was first successfully demonstrated in a CMB experiment by MAXIPOL [35].

2.3 Instrument design

The EBEX instrument (Fig. 2.3) is a bolometric, balloon-borne telescope operating at three frequency bands centered at 150, 250 and 410 GHz with polarization sensitivity achieved with a continuously rotating half wave plate (HWP) and fixed

wire grid analyzer. EBEX uses an f/1.7 Gregorian-Dragone type telescope with a 1.5 m primary and 1 m diameter secondary mirror. Light from the reflectors is re-imaged in a cryogenic receiver and coupled to the detectors by an array of smooth-walled, conical feed horns which produce 8′ beams at all frequency bands and a 6° instantaneous field of view. Signal is detected in 1920 spider-web transition edge sensor (TES) bolometers that are read out by superconducting quantum interference devices (SQUIDs) in a $\sim$ MHz frequency domain multiplexing architecture.

2.3.1 Receiver

The cryostat receiver houses the re-imaging optics, polarization modulation components, detector arrays and SQUID preamplifiers. The Dewar is cooled with liquid nitrogen, liquid helium and the boil off of both gases to achieve four cryogenic stages at 240, 77, 30 and 4.2 K. Fig. 2.4 shows a cross-section model of the receiver and photograph of the internal receiver hardware. Light from the reflectors enters the cryostat through a 30 cm diameter window. Polarized light is modulated by a continuously rotating half wave plate (HWP) held at 4 K and located at the aperture stop. A polarizing grid oriented at 45° with respect to the direction of light propagation reflects or transmits the radiation to one of two focal planes held at 270 mK by a three-stage ^{3}He adsorption refrigerator [37]. All re-imaging lenses are composed of ultra high molecular weight polyethylene (UHMWPE). Three lenses are held at 1 K using an additional internal refrigerator to reduce radiative loading on the bolometers. Signal from the bolometers is read out with SQUIDs located in an EMI tight compartment below the cold plate.

2.3.2 HWP polarimetry

Principle

Polarization modulation is achieved with a continuously rotating HWP and fixed wire grid analyzer. Fig. 2.5 demonstrates the concept. Linearly polarized light

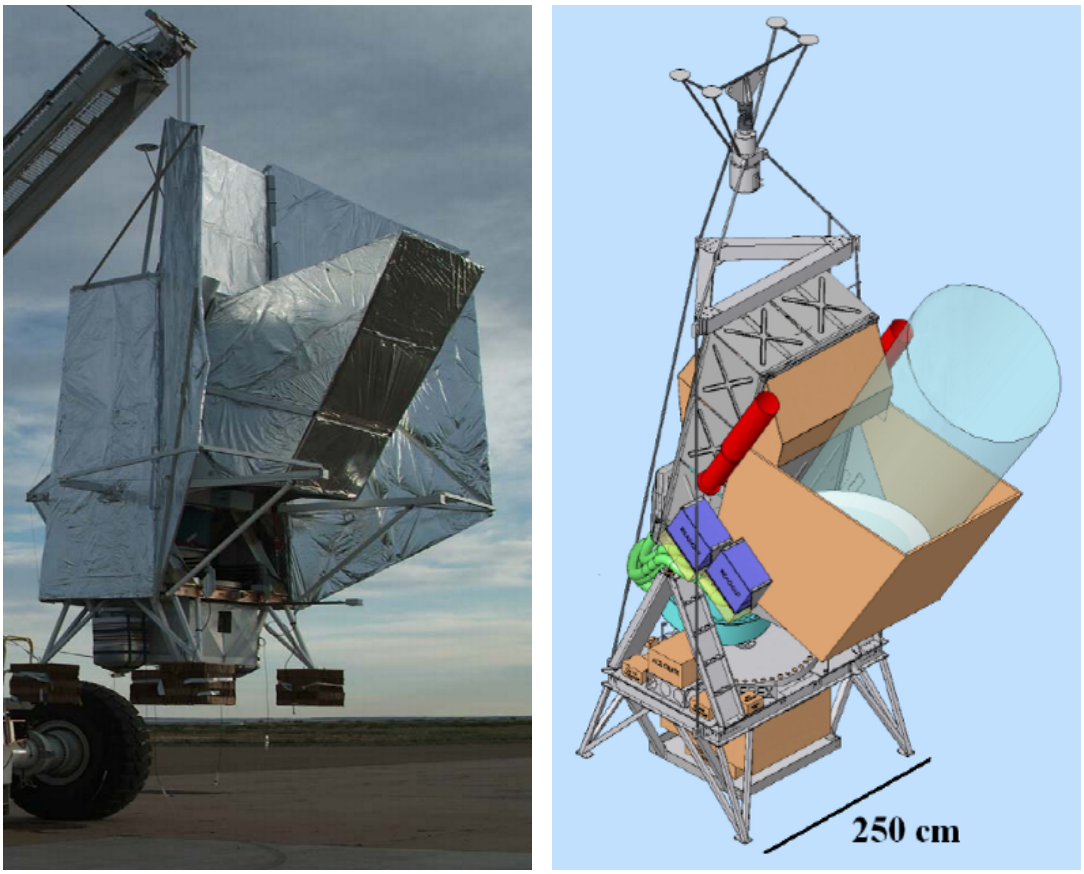

Figure 2.3: A photograph and solid works model of the EBEX instrument. The photograph was taken prior to the NAF and shows the sun shades and ground shields used to block stray radiation from the receiver.

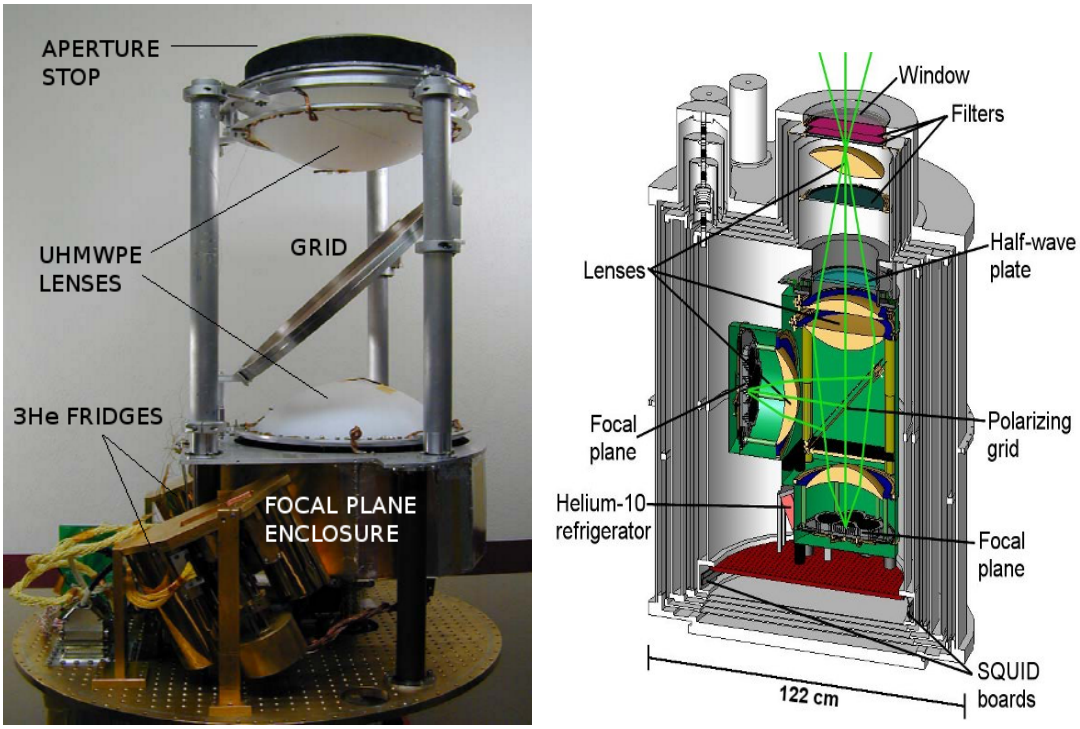

Figure 2.4: A cross-section model of the 1.2 m diameter EBEX cryostat receiver and a photograph of the current receiver hardware. The current implementation for the NAF has one focal plane.

incident on a continuously rotating HWP at fixed frequency f exists the HWP linearly polarized and rotating at frequency $2f$. Once analyzed by a wire grid polarizer and detected, the intensity of the polarized signal sinusoidally modulates at frequency $4f$. The amplitude of the sine wave depends on the level of polarization of the incident radiation. Fully polarized light will maximize the amplitude while unpolarized light yields no modulation. The phase of the sine wave depends on the polarization angle. The amplitude and phase of the modulation yields the polarization fraction and angle of the incident radiation.

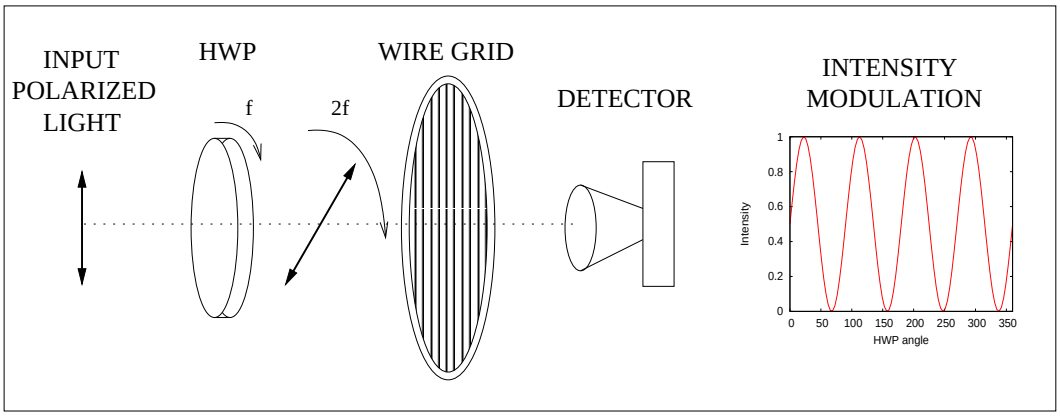

Figure 2.5: Schematic demonstrating half wave plate (HWP) polarimetry. A continuously rotating HWP and fixed wire grid polarizer modulates incoming polarized light at four times the rotation rate of the HWP. From the amplitude and phase of the modulated signal, the polarization fraction and angle of the incoming polarized light can be determined.

Merits of HWP polarimetry

This modulation scheme mitigates systematic errors in several ways. With this technique, each bolometer in the array makes an independent measurement of the Stokes I,Q and U parameters of the incoming radiation. The detectors are not differenced which avoids a potential source of instrumental polarization. Since the telescope scans the sky, polarization anisotropy data resides in the side bands of the $4f$ signal in Fourier space. Any spurious or systematic signals appearing in the data outside of this band can be filtered away. Also, moving the signal to higher frequencies avoids low-frequency detector noise, improving the sensitivity to polarized signals. In addition, instrumental polarization (IP) is limited to optical elements sky side of the HWP because any IP in down-stream elements does not modulate at $4f$.

Achromatic half wave plate

A HWP is inherently a monochromatic device. EBEX requires broad-band optical components and therefore uses and achromatic half wave plate (AHWP) [38]. The EBEX AHWP is composed of a stack of five A-cut, 1.65 mm thick sapphire plates with crystal axes rotated by angles 0-25-88-25-0 relative to the first plate. The plates are bonded together with a thin layer of polypropylene. The AHWP is predicted to operate with $> 98\%$ modulation efficiency from $120 < \nu < 450$ GHz [39].

2.3.3 HWP rotation mechanism

To lessen polarization systematics, it is advantageous to place the HWP at the aperture stop. In EBEX the aperture stop is at 4 K. Continuous rotation at cryogenic temperatures is a technical challenge that we address using a superconducting magnetic bearing (SMB) to levitate the HWP [40]. The HWP mounts inside a segmented ~ 1 Telsa ring magnet which then levitates above a tile of YBCo high temperature superconductors. The HWP is rotated by a belt system. A kevlar belt attaches the HWP to a pulley driven by a motor external to the cryostat. We plan 6 Hz rotation for LDB, which places polarized signals in the side bands of 24 Hz.

2.3.4 Focal plane

The polarizing grid splits incoming radiation to one of two identical focal planes held at ~ 270 mK. A focal plane is composed of an array of aluminum, smooth-walled conical feed-horns and single mode transmitting cylindrical waveguides coupled to planar silicon detector arrays. The horns produce $8'$ beams at all frequency bands. Fig. 2.6 shows the detector layout for one focal plane. Each focal plane observes at all three frequency bands centered on 150, 250 and 410 GHz and contains 738 detectors with a Strehl ratio > 0.85 at 250 GHz. The bands are defined by waveguide cut-offs and metal mesh, low pass filters [41] located

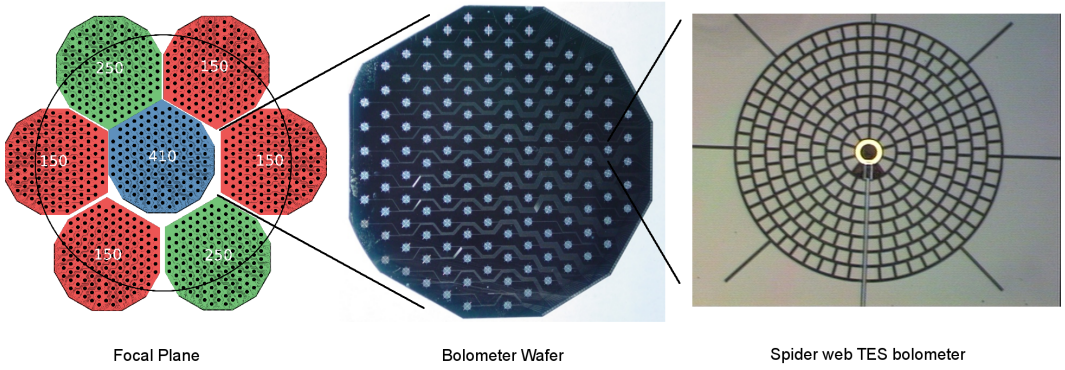

Figure 2.6: A single EBEX detector focal plane layout. Seven silicon detector wafers each with 140 bolometers compose the focal plane. [4,2,1] wafers observe at [150,250,410] GHz. The middle shows a photograph of the bolometer wafer, and on the right is a zoom in on a single spider-web transition edge sensor bolometer.

above the horn entrance aperture. Table 2.1 summarizes the EBEX bands and throughput. Seven silicon bolometer wafers 8 cm in diameter make up a focal plane. One wafer observes at a single frequency band.

ν_c (GHz)	ν_{low} (GHz)	ν_{high} (GHz)	$A\Omega$ (m^2str)
150	133	173	3.24×10^{-6}
250	218	288	1.44×10^{-6}
410	366	450	5.36×10^{-7}

Table 2.1: Band edges and throughput of EBEX frequency bands including loss due to cold Lyot stop.

2.3.5 Detectors

In the full EBEX LDB instrument, sky signal is detected in 1920 spider-web transition edge sensor (TES) bolometers, distributed in 14 Si detector wafers on

two focal planes. The bolometers are uniquely designed for the balloon platform. The lower background loading and telescope temperatures at balloon altitudes allow sensitivity gains by lowering the thermal conductance G of the bolometer. The thermal conductance controls the dynamic range and largely determines the sensitivity of the bolometer. The design goal at 150 GHz is $G \sim 21$ pW/K, which gives a 140 $\mu K\sqrt{Hz}$ noise equivalent temperature (NET).

The left panel of Fig. 2.7 shows a photograph of an EBEX bolometer array fabricated in the University of California, Berkeley Microlab clean-room facility using standard thin film deposition and optical lithography. The array contains 140 spider-web TES bolometers spaced 6.6 mm apart center-to-center. Superconducting aluminum leads connect each TES to wire-bonding pads at the bottom five sides of the wafer. One of the bolometers is shown in the right panel of Fig. 2.7. The bolometer consists of four main structures: a spider-web absorber, a TES, a gold ring and thermally isolating legs. The 2.1 mm diameter spider-web absorber is composed of 1 μm thick, 6 μm wide low-stress silicon nitride with a 117 μm grid spacing. The spider web geometry is chosen to reduce heat capacity, which decreases the optical time-constant, as well as the cross-section to cosmic rays. The web is metalized with a 2 μm wide, 200 $\mathring{A}$ thick layer of Au which has a DC sheet resistance $\sim 200\ \Omega/\square$. The spider-web is thermally isolated from the heat-sink by silicon nitride legs that have a ratio of cross-sectional area to length $A/l = 66$ nm. The transition edge sensor is composed of an Al/Ti proximity effect sandwich tuned to have a $\sim 1\ \Omega$ normal resistance and transition temperature $T_c \sim 500$ mK. The sensor is thermally attached to a gold ring. The heat capacity of the gold ring limits the sensor bandwidth ensuring stability [42].

Each array is composed of two wafers: the detector wafer and the backing wafer. The detector wafer contains all micro-machined structures and the back side is coated with a 1 μm layer of Al to create a back-short used to increase the bolometer absorption efficiency. The backing wafer is a bare silicon wafer which is bonded to the first piece so that the total thickness of the composite wafer is compatible with standard micro-lab machines. The distance to the back-short is

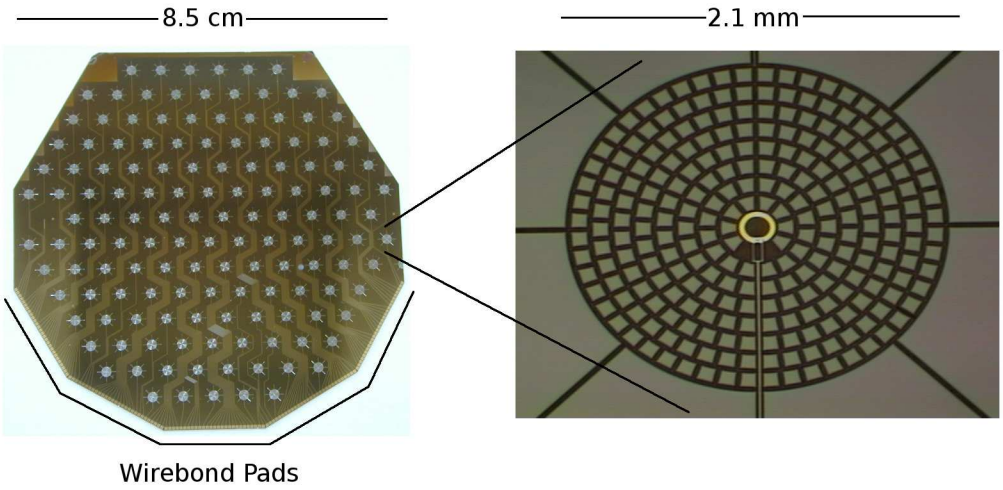

Figure 2.7: **Left:** The 140 element transition edge sensor (TES) bolometer array. **Right:** A close up picture of a spider-web TES bolometer. The gold ring and TES can be seen in the middle of the picture with the superconducting leads exiting the bottom of the picture.

determined by the observation wavelength, $\lambda_c/4$ where λ_c is the center observation wavelength. However, at 410 GHz we use a $3/4\lambda$ back-short because the thickness of the silicon at $\lambda/4$ is prohibitively thin.

2.3.6 Readout

The bolometers are read out with 100 series array superconducting quantum interference devices (SQUIDs) fabricated at NIST [43]. Fig. 2.8 shows the SQUIDs on their custom PCB card, which we install at 4 K in the cryostat. To decrease the heat load at the sub-Kelvin stage, the bolometers are multiplexed in the frequency domain such that currents produced by n bolometers travel on a single pair of wires to a SQUID amplifier. For LDB, EBEX plans a multiplexing factor of n=16. We utilize digital frequency domain multiplexing (DfMUX) electronics [44] to tune, operate and monitor the bolometer and SQUID readout system. SQUID

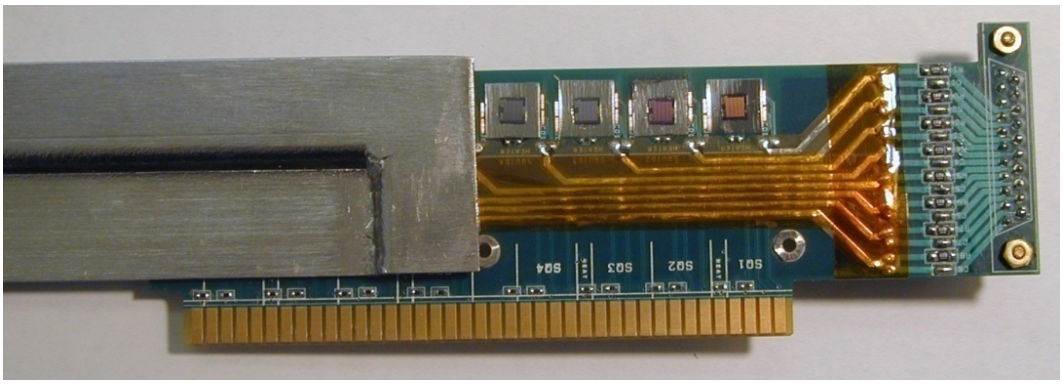

Figure 2.8: Photograph of a SQUID mounting card and cryoperm magnetic shielding. One card contains eight SQUIDs. Four are visible at the top of the photograph within the niobium squares. EBEX plans 15 cards for LDB.

readout is detailed in Chapter 4 and frequency domain multiplexing is described in Chapter 5.

2.4 NAF configuration

For the North American test flight (NAF), EBEX flew a stripped down version of the LDB instrument design as described in Sec. 2.3. The list below outlines the major differences.

- One focal plane
- Three bolometer wafers – one per frequency band
- Forty-eight SQUIDs on six SQUID mounting cards
- Bolometer multiplexing factor of eight
- Twelve DfMUX boards distributed in two readout crates
- HWP rotation frequency $\sim$2 Hz

Chapter 3

Bolometer Theory

This chapter discusses bolometer theory with strong emphasis on the superconducting transition edge sensor (TES) bolometer, the type of bolometer used in EBEX. We derive the responsivity of the TES bolometer and discuss the linearity, dynamic range and sensitivity to bath temperature fluctuations. We describe the time constants associated with bolometers and outline the relevant noise sources including a sensitivity calculation for the designed EBEX 150 GHz bolometer.

3.1 Thermal detectors

In their simplest form, thermal detectors consist of an absorbing element of heat capacity C coupled to a heat-sink at temperature T_o via a weak thermal link (see Fig. 3.1). Power absorbed in the detector raises the absorber temperature T above the heat-sink. By measuring the absorber temperature, the incident power can be determined. The steady state power flow through the device is described by

$$P = \bar{G}\Delta T \tag{3.1}$$

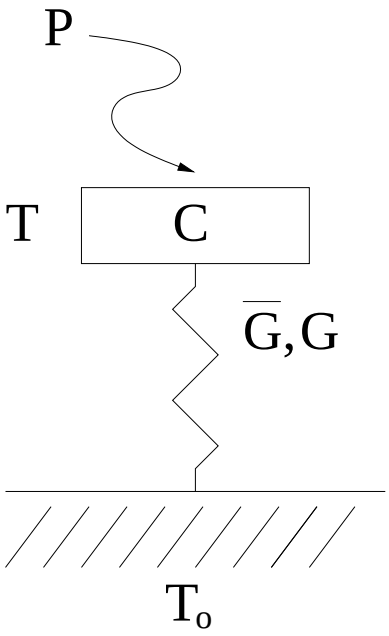

Figure 3.1: Lumped element model of a thermal radiation detector.

in which $\bar{G}$ is the average thermal conductance of the weak link from the absorber to the heat-sink. The dynamic thermal conductance G is given by

$$G = \frac{dP}{dT}. \tag{3.2}$$

If power absorbed in the detector changes instantaneously to a value P_1, the detector temperature changes as a function of time approaching the value $T_1 = T_o + P_1/\bar{G}$ with a time constant C/G.

3.1.1 Weak links

Considering the generalized flow of heat across a substance yields a relation between the average and dynamic thermal conductance. The heat transferred at a position x along a link is

$$P(x) = A(x)\kappa(T)\frac{dT}{dx}, \tag{3.3}$$

where $A(x)$ is the cross-sectional area at position x and $\kappa(T)$ is the thermal conductivity of the link. The total power flow from the absorber to the heat-sink of length l away from the heat-sink is

$$P = \frac{\int_{T_o}^{T} \kappa(T')\, dT'}{\int_0^l \frac{dx}{A(x)}}. \tag{3.4}$$

Eq. 3.4 is the most general form for the steady state power flow across a thermal detector. The right hand side is equal to $\bar{G}\Delta T$. If the link has uniform cross-sectional area A, then the total power across the link is

$$P = A/l \int_{T_o}^{T} \kappa(T')\, dT'. \tag{3.5}$$

The thermal conductivity of many materials can be described by a power law $\kappa = \kappa_o T^n$, in which case

$$P = A/l \frac{\kappa_o}{n+1}(T^{n+1} - T_o^{n+1}). \tag{3.6}$$

Comparing the right hand sides of Eqs. 3.1 and 3.6 yields the following relation between G and $\bar{G}$ [45]

$$G/\bar{G} = (n+1)\frac{1 - T_o/T}{1 - T_o^{n+1}/T^{n+1}}. \tag{3.7}$$

3.2 Superconducting TES bolometers

The bolometer, invented by Langley [46], is a type of thermal detector that uses a resistive element to sense the temperature of the absorber. The thermistor is chosen to have a strong temperature dependence around the operating temperature T. The two most common types of thermistor used at millimeter wavelengths are doped semi-conductors such as neutron-transmutation-doped (NTD) Germanium and the superconducting transition edge sensor (TES).

3.2.1 Electrical bias and feedback

In operation, the bolometer is biased with electrical power P_e to maintain the steady state temperature T above the heat-sink temperature. Since the bias power is a function of resistance and $R = R(T)$, the bolometer has an electro-thermal feedback mechanism. If $\frac{dP_e}{dT} < 0$, the feedback is negative, and if $\frac{dP_e}{dT} > 0$ the feedback is positive. Negative feedback is desired for stability, and therefore the slope of the thermistor R(T) determines the type of bias. Under constant current bias $\frac{dR}{dT} < 0$ for stability since

$$\frac{dP_e}{dT} = \frac{d(I^2 R(T))}{dT} = I^2 \frac{dR}{dT}. \tag{3.8}$$

Conversely, under constant voltage bias $\frac{dR}{dT} > 0$ to achieve negative feedback.

$$\frac{dP_e}{dT} = \frac{d(v^2/R(T))}{dT} = -\frac{v^2}{R^2}\frac{dR}{dT}. \tag{3.9}$$

For NTD bolometers, $\frac{dR}{dT} < 0$ and thus are operated under constant current bias. Superconducting TES bolometers have $\frac{dR}{dT} > 0$ and so are operated under constant voltage bias.

Superconductors make an excellent choice for a thermistor because of their extremely sharp R(T) curves (see Fig. 3.2). In operation, the TES bolometer is biased with constant voltage on its superconducting transition. An increase in power absorbed in the bolometer increases the bolometer's resistance and decreases the current produced by the TES. This change in current is measured to determine the incident power fluctuation. The first demonstration of the the voltage biased TES with strong negative electro-thermal feedback was by Irwin [47].

3.2.2 Responsivity

The behavior of the TES bolometer is governed by two coupled differential equations. One equation describes the thermal circuit, and the other describes the electrical circuit. The two equations are coupled by the TES resistance which is a

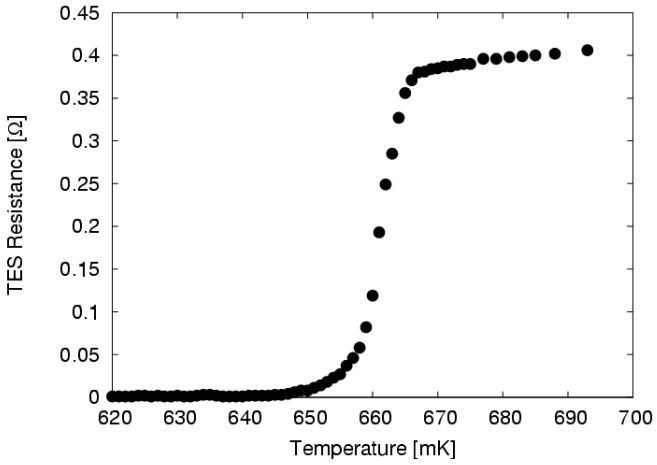

Figure 3.2: Measured resistance versus temperature of a superconducting transition.

non-linear function of both temperature and current, R(T,I). Irwin and Hilton [48] recover the dynamics of the TES in the small signal limit by expanding the variables R and T around their equilibrium values. Razeti [49] extends the analysis to large signals, and Rostem, Withington and Goldie [50] have since developed a numerical technique which describes the TES dynamics without any assumptions about the signal size.

We derive the current responsivity ($S_I = \delta I/\delta P$) of a TES bolometer in the small signal limit following Lee [45]. To begin, we determine $\delta P/\delta T$ by considering a single Fourier component of fluctuating power absorbed in the bolometer $\delta P e^{i\omega t}$. This power produces a fluctuating temperature in the bolometer $\delta T e^{i\omega t}$. The total power flow through the bolometer is

$$P + P_e + \delta P e^{i\omega t} + \delta P_e e^{i\omega t} = \bar{G}(T - T_o) + (G + i\omega C)\delta T e^{i\omega t}. \tag{3.10}$$

Considering the time dependent part of this equation yields $\delta P/\delta T$.

$$\delta P e^{i\omega t} + \delta P_e e^{i\omega t} \;\; = \;\; (G + i\omega C)\delta T e^{i\omega t} \tag{3.11}$$

$$\delta P e^{i\omega t} - \frac{V^2}{R^2}\frac{dR}{dT}\delta T e^{i\omega t} = (G + i\omega C)\delta T e^{i\omega t} \quad (3.12)$$

$$\delta P/\delta T = (G + i\omega C + \frac{P_e \alpha}{T}). \quad (3.13)$$

In the last step, we substituted the unitless, logarithmic slope of the transition

$$\alpha \equiv \frac{d\log R}{d\log T}. \quad (3.14)$$

The last term on the right hand side of Eq. 3.13 is due to negative electro-thermal feedback. The addition of this term decreases the temperature excursion δT for a given power fluctuation δP relative to a bolometer without feedback. The strength of electro-thermal feedback is characterized by the loopgain,

$$\mathcal{L}(\omega) = -\frac{\delta P_e}{\delta P} \quad (3.15)$$

$$= \frac{P_e \alpha}{GT(1 + i\omega\tau)} = \frac{\mathcal{L}}{1 + i\omega\tau}. \quad (3.16)$$

The loopgain has a zero frequency amplitude $\mathcal{L} = P_e\alpha/GT$, and rolls of as a single pole with a time constant $\tau = C/G$. Therefore

$$\delta P/\delta T = G(1 + i\omega\tau)(1 + \mathcal{L}), \quad (3.17)$$

and we may now determine the TES bolometer current responsivity:

$$S_I = dI/dP = \frac{1}{\delta P/\delta T}\frac{dI}{dT} = \frac{1}{\delta P/\delta T}\frac{-v}{R^2}\frac{dR}{dT} \quad (3.18)$$

$$= -\frac{1}{v}\frac{\mathcal{L}}{\mathcal{L}+1}\frac{1}{1 + i\omega\tau_{et}}, \quad (3.19)$$

where the electro-thermal time constant

$$\tau_{et} = \frac{\tau}{1 + \mathcal{L}}. \quad (3.20)$$

Note when the loopgain is high, the responsivity goes as the inverse of the voltage bias, $S_I \approx -1/v$. Also, negative electro-thermal feedback limits the temperature

excursion of the TES which acts to "speed up" the TES. This speed up is evident by the presence of $\mathcal{L}$ in the denominator of Eq. 3.20.

The sensor acts as a null detector. Electrical power compensates for the radiative power absorbed in the sensor. This phenomenon is seen graphically in the current versus voltage bias (IV) characteristics of the TES bolometer (Fig. 3.3).

3.2.3 Dynamic range and linearity

The dynamic range of the bolometer is determined by the maximum power the weak link can conduct away such that the absorber temperature does not exceed the TES transition temperature. This power is often called the saturation power P_{sat} and is explicitly:

$$P_{sat} = A/l \int_{T_o}^{T_c+\delta} \kappa(T')\, dT'. \tag{3.21}$$

The upper limit of the integral $T_c + \delta$ is the critical temperature of the superconductor plus the 10 - 90% transition width. A power absorbed in the bolometer greater than P_{sat} will drive the temperature of the bolometer above the transition where it is insensitive to temperature changes. Thus, P_{sat} sets the dynamic range of the bolometer, typically a few picowatts for a balloon based experiment.

In practice, linearity may limit the dynamic range to a value less than P_{sat}. The goal for the rest of the section is to determine the responsivity as a function of applied optical load since a responsivity change implies non-linearity. We first calculate the responsivity as a function of temperature.

To proceed we assume the functional form for the transition

$$R(T) = R_n/2(\tanh \frac{T - T_c}{\delta} + 1). \tag{3.22}$$

R_n is the normal resistance of the bolometer, T is the bolometer temperature, T_c is the superconducting critical temperature and δ is the aforementioned 10-90% transition width. Fig. 3.4 plots R(T) and the normalized responsivity as a function of temperature using Eqs. 3.19 and 3.22 for standard NAF EBEX

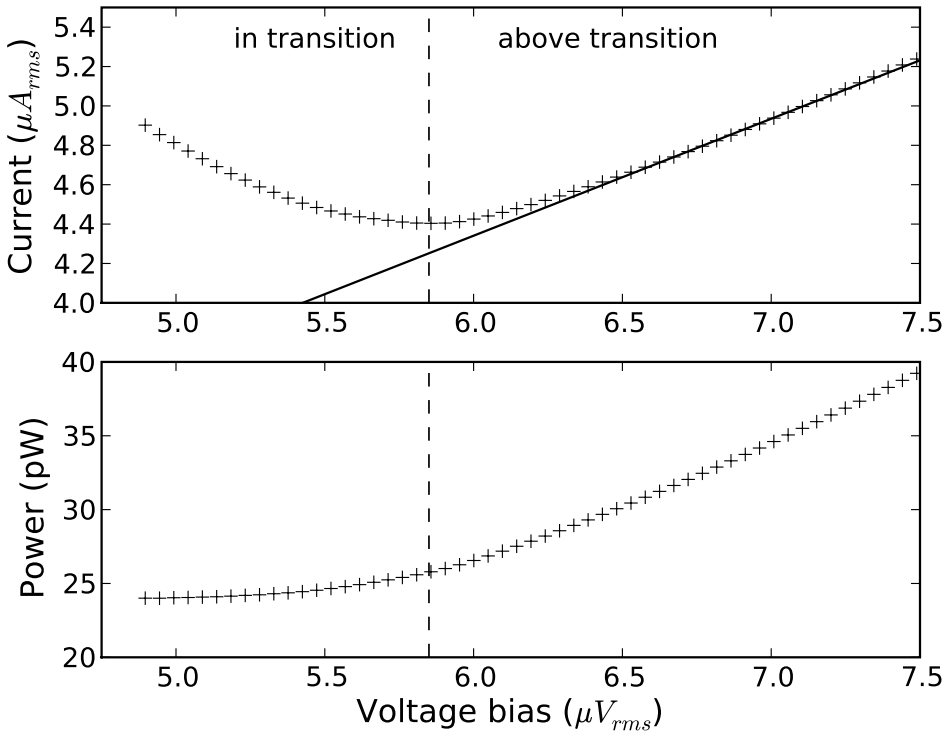

Figure 3.3: The top plot shows the bolometer current as a function of voltage bias. Above the superconducting transition the bolometer is Ohmic (solid line). Once the bolometer enters the superconducting transition, strong negative electrothermal feedback ensures that the total power in the transition is constant. Thus the current in the transition goes as $1/v$. The bottom plot shows the electrical power dissipated by the bolometer as a function of voltage bias. Constant total power in the transition is evident below $\sim 5.2\ \mu V_{rms}$.

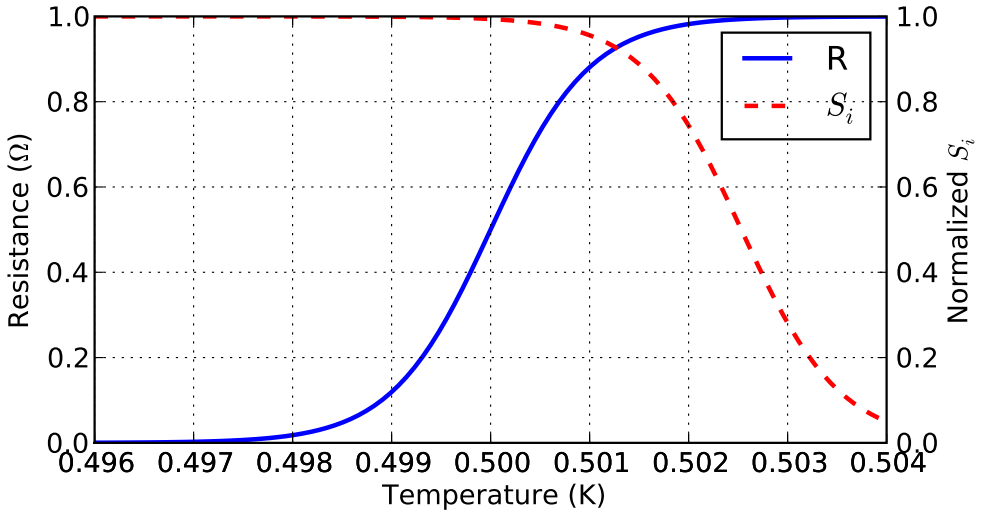

Figure 3.4: Blue, solid line shows a theoretical transition calculated using Eq. 3.22. The red, dashed line shows the responsivity versus temperature for the blue R(T) transition normalized to the value approximated deep in the transition $S_I = 1/v$. The left [right] vertical label corresponds to the R(T) [$S_I(T)$] curve. Both curves are calculated using typical EBEX NAF bolometer values.

bolometer parameter values ($R_n = 1\Omega$, $T_c = 500$ mK, $\delta = 10$ ms, $G = 60$ pW/K, $v = 2.2\ \mu V_{rms}$).

The operating temperature is controlled by the electrical bias, and thus in practice the bias position determines the linearity and dynamic range. The TES temperature is a function of both the optical and electrical power through the DC power flow equation:

$$P_o + P_e = P_o + v^2/R(T) = A/l \int_{T_o}^{T} \kappa(T')\, dT'. \tag{3.23}$$

Given a voltage bias and an optical load P_o, we calculate the TES temperature and look up the responsivity from Fig. 3.4. The voltage bias is determined by the optical load and the fraction of R_n that the bolometer is biased.

Fig. 3.5 shows the linearity and dynamic range for two bias positions ($0.1R_n$

and $0.7R_n$) and illustrates that both of these quantities improve deeper into the transition. The effective dynamic range is less for the bolometer biased to $0.7R_n$. This is because a fraction of P_{sat} is consumed by the electrical bias v^2/R, which is minimum but finite above the transition with a value v^2/R_n. The effective dynamic range is then $P_{sat} - v^2/R_n$. Biasing the bolometer deeper into the transition requires less voltage bias and therefore maximizes the effective dynamic range. In addition, biasing the bolometer deeper into the transition improves linearity. The fraction of optical load relative to P_{sat} that will cause a 1% change in the responsivity for a bolometer biased at $0.7R_n$ is 0.05 for increasing loads and 0.08 for decreasing loads. For a bolometer biased to $0.1R_n$, these numbers increase to 0.22 for increasing loads, whereas for decreasing loads the responsivity changes by less than 0.5% from $P_o/P_{sat} = 0.5$ to $P_o/P_{sat} = 0$.

3.2.4 Sensitivity to bath temperature fluctuations

The responsivity calculated in Eq. 3.19 is a weak function of bath temperature T_o. P_e is the only term in the loopgain $\mathcal{L}$ that depends on T_o. The change in electrical bias to a change in bath temperature is:

$$dP_e/dT_o = -G(T_o). \tag{3.24}$$

The change in responsivity due to a bath temperature change is then

$$dS_I/dT_o = \frac{dS_I}{d\mathcal{L}}\frac{d\mathcal{L}}{dT_o} = \frac{1}{vT}\frac{\kappa(T_o)}{\kappa(T)}\frac{1}{(1+\mathcal{L})^2}. \tag{3.25}$$

The change in responsivity due to bath temperature fluctuation is suppressed by two powers of the TES loopgain $\mathcal{L}$.

3.3 Time constants in bolometers

In Sec. 3.2.2, we discussed the sensor frequency response for the case of a TES, which is described by Eq. 3.20. For any bolometer, the sensor is thermally coupled to an absorber, and as such the bolometer exhibits more than a single time

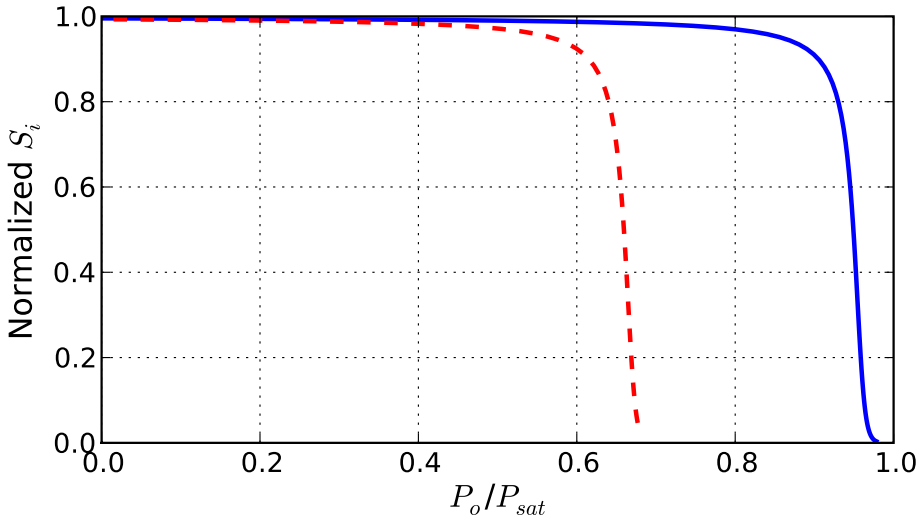

Figure 3.5: Calculated responsivity versus fractional optical load for bias positions $0.7R_n$ (dashed, red) and $0.1R_n$ (solid, blue). The calculation assumes nominal EBEX NAF bolometer parameters with an optical load of $0.5P_{sat}$, a power law dependence on the thermal conductivity with index $n = 3$ and a heat-sink temperature $T_o = 0.27$ K. The equilibrium bias position is $P_o/P_{sat} = 0.5$.

constant in its frequency response to absorbed power. Fig. 3.6 shows a thermal circuit model for a generic bolometer. The absorber has heat capacity C_a and is connected to the thermal bath at T_o through the thermal conductance G_{link} and is also coupled to a sensor of heat capacity C_s through the thermal conductance G_{as}. Since any sensor must have electrical leads for readout, the sensor is also directly coupled to the heat-sink through G_{leads}. In practice, $G_{leads} << G_{link} << G_{as}$ in which case the thermal response can be described by two time constants in series, the optical time constant $\tau_o = C_a/G_{link}$ and the sensor time constant $\tau_s = C_s/G_{link}$. If the sensor time constant is much smaller than the optical time constant, the bolometer frequency response is described by a single pole, and the thermal model collapses to that shown in Fig. 3.1. Such is the case for mm-wave absorber coupled bolometers like EBEX detectors because the size of the absorber

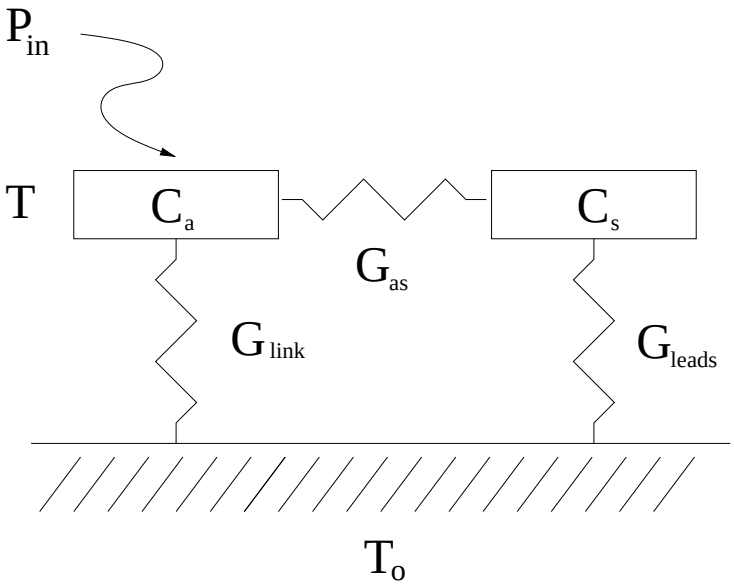

Figure 3.6: Lumped element thermal model of a bolometer illustrating the optical and sensor time constants τ_o and τ_s. See text for parameter definitions.

must be of order the observation wavelength. This restriction sets a practical lower limit on C_a and thus τ_o, typically a few milli-seconds at 150 GHz. The size of the sensor, on the other hand, can be very small. Also in the case of a TES bolometer, τ_s is decreased by electro-thermal feedback.

3.4 Noise sources in TES bolometers

The most common figure of merit for the sensitivity of a bolometer is the noise equivalent power (NEP), which has multiple definitions in the literature. We define NEP as the power *absorbed* in the bolometer required to produce a signal equal to the noise in a 1 Hz electrical bandwidth. The lower the NEP, the more sensitive the bolometer.

Bolometer noise theory has been described by Mather [51], which we follow in this discussion. Contributions to the bolometer NEP come from a number of

uncorrelated sources: photon noise, phonon noise, bolometer Johnson noise and readout noise. The expression for the total bolometer NEP is

$$N_{tot}^2 = N_{photon}^2 + N_{phonon}^2 + \frac{1}{S_I^2}(N_{Johnson}^2 + N_{readout}^2) \quad (3.26)$$

$$= 2h\nu P(1+\omega^2\tau_o^2) + \gamma 4k_bT^2G + \frac{1}{S_I^2}(4k_bT/R + N_{readout}^2). \quad (3.27)$$

In this equation, h is Planck's constant, ν is the center observation frequency, P is the optical power absorbed in the bolometer, ω is the angular frequency, τ_o is the optical time constant, k_b is Boltzmann's constant, T is the temperature of the bolometer, G is the dynamic thermal conductance R is the resistance of the bolometer and S_I is the current responsivity of the TES (Eq. 3.19).

Sensitivity to photons rolls off with the optical time constant. Therefore, the photon noise NEP is multiplied by the frequency response associated with τ_o. We also note the photon noise term in Eq. 3.27 is an approximation. The full expression for photon noise NEP is [52]

$$N_{photon}^2 = 2\int P_\nu h\nu \, d\nu + \int \frac{P_\nu^2 c^2}{A\Omega\nu^2} \, d\nu. \quad (3.28)$$

The first term obeys Poisson statistics where P_ν is power per unit frequency of the source, ie the Planck result for the spectral brightness of a black body times the optical throughput

$$P_\nu = A\Omega \frac{2h\nu^3}{c^2} \frac{1}{e^{h\nu/kT} - 1}, \quad (3.29)$$

where $A\Omega$ is the optical throughput. The second term in Eq. 3.28 is due to photon bunching and is neglected from Eq. 3.27. This term is non-negligible only when there are a large number of photons per standing wave mode given by $n = [exp(h\nu/k_bT) - 1]^{-1}$. For frequencies and temperatures relevant for EBEX, $n < 0.6$.

Photon noise sets the fundamental sensitivity limit on an individual bolometer. The goal of bolometer design is to make all other noise terms negligible compared to photon noise while also achieving the required dynamic range. A bolometer

in which the NEP is dominated by photon noise is termed background limited or 'BLIP' limited.

In the phonon noise term $N^2_{phonon} = \gamma 4 k_b T^2 G$, γ is a unitless number less than one that accounts for the temperature gradient along the thermal link [51]. It is an effective temperature weighted by the thermal conductivity of the weak link. Explicitly:

$$\gamma = \frac{\int_{T_o}^{T} (\frac{T' \kappa(T')}{T \kappa(T)})^2 dT'}{\int_{T_o}^{T} \frac{\kappa(T')}{\kappa(T)} dT'}, \tag{3.30}$$

where $\kappa(T)$ is the thermal conductivity at temperature T. If we assume a power law of index n for the thermal conductivity,

$$\gamma = \frac{n+1}{n+2} \frac{1-(T_o/T)^{n+2}}{1-(T_o/T)^{n+1}}. \tag{3.31}$$

Note that G in Eq. 3.27 is the dynamic thermal conductance *not* the average conductance $\bar{G}$. To write the phonon noise in terms of $\bar{G}$ (since this is more easily measured), we use Eq. 3.7. Therefore assuming a power law of index n,

$$\frac{\gamma G}{\bar{G}} = \frac{(n+1)^2}{n+2} \frac{1-(T_o/T)^{n+2}}{[1-(T_o/T)^{n+1}]^2} (1 - T_o/T). \tag{3.32}$$

This ratio is 1.6 for the typical values $n = 3$, $T_o/T = 0.5$ demonstrating that the often used shortcut $N_{phonon} = \sqrt{4 k_b T^2 \bar{G}}$ under-estimates the phonon noise by 25% in units of $\mathrm{W}/\sqrt{Hz}$.

The Johnson noise of the bolometer and the readout noise include the current responsivity S_I to refer these current noise terms to power. A large responsivity suppresses the current noise terms relative to the power noise terms. Using the approximation $S_I \approx 1/v$ and solving the DC power flow equation Eq. 3.1 for voltage bias, we may write

$$S_I = \frac{1}{R\sqrt{\bar{G}\Delta T - P}}. \tag{3.33}$$

From this discussion, we see that optimizing bolometer sensitivity requires tuning the thermal conductance of the weak link. $\bar{G}$ must be large enough to observe the background power loading, but overshooting $\bar{G}$ results in a two fold sensitivity hit. One factor comes from phonon noise which scales as $\sqrt{G}$ and another comes from the reduced responsivity apparent in Eq. 3.33 which amplifies current noise terms.

3.4.1 Expected NEP for EBEX ideal bolometer

Fig. 3.7 shows the NEP spectrum of the designed EBEX 150 GHz bolometer while observing the CMB. The white noise NEP is 2.3×10^{-17} W/$\sqrt{Hz}$ calculated from Eq. 3.27 [1] . Table 3.1 tallies the individual noise terms. The fourth column of Table 3.1 includes a factor of two for both the Johnson and readout current noise terms from the lock-in measurement technique used in the fMUX system (see Chapter 5 and Appendix B.1).

source	equation	raw NEP W^2/Hz $\times10^{-34}$	NEP with DfMUX W^2/Hz $\times10^{-34}$
Photon	$2h\nu P$	1.0	1.0
Phonon	$\gamma 4k_bT^2G$	2.3	2.3
Johnson	$4k_bTv^2/R$	0.5	1.0
Readout	NA	.45	.9
Quadrature noise sum			5.2

Table 3.1: Expected white noise level for EBEX 150 GHz bolometers.

The designed EBEX bolometer is not photon noise limited. The dominant NEP term is due to phonon noise. However, this calculation neglects all radiative loading from the thermal emission of the telescope mirrors and re-imaging optics inside the cryostat. In the calculation, only 0.5 pW of the total 2.3 pW of dynamic

[1] We assume $S_I = 1/v$, $A\Omega = 4\times10^{-6}$ m^{2}str, $\bar{G}$=10 pW/K, n=3, T_c=500 mK, T_o=270 mK, τ_o=3 ms and τ_{et}=1 ms.

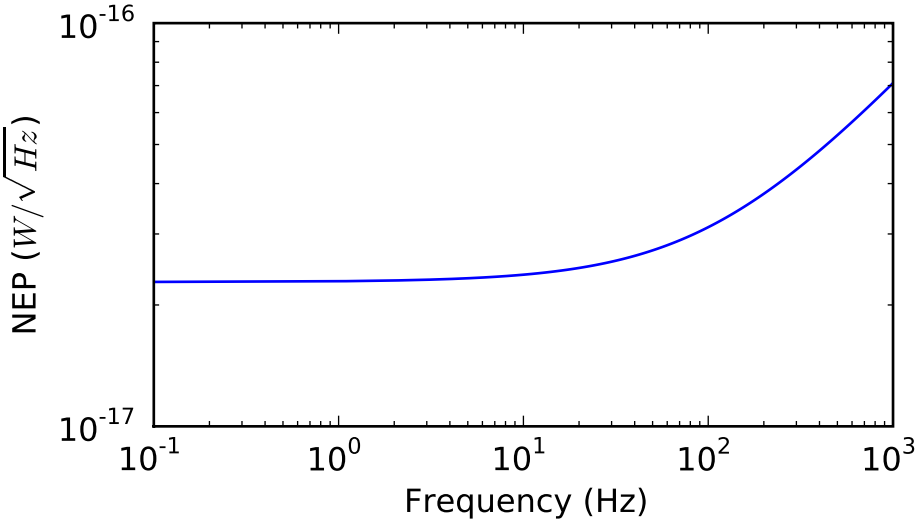

Figure 3.7: Calculated 150 GHz NEP

range is optical load, which comes entirely from the CMB assuming 100% optical efficiency. The emissive loading will consume more of the 2.3 pW of dynamic range, increase the photon noise NEP and decrease the readout and bolometer Johnson noise NEP terms.

Chapter 4

SQUIDs

To read out currents produced by transition edge sensor bolometers, we use superconducting quantum interference devices (SQUIDs). This choice is motivated by the low sensor noise and input impedance of the SQUID. In Sec. 4.1, we describe the theory of DC SQUID operation. In Sec. 4.2 we introduce the series array SQUID and briefly discuss their benefits. In Sec. 4.3, we describe the flux-locked feedback loop circuit used to extend the dynamic range of the SQUID and provide measurements of the SQUID feedback loopgain $\mathcal{L}$.

4.1 Theory of operation

The DC SQUID is a highly sensitive magnetic flux to voltage transducer. In this section, we quantify this relation and show that the voltage across a DC SQUID is periodic to an applied external flux with periodicity of $\Phi_o = h/2e$, the flux quantum. To this end, we discuss the physics of the Josephson junction and the phenomena of magnetic flux quantization.

4.1.1 Josephson junctions

A Josephson junction is a superconductor interrupted by a weak link. This link can be a constriction of the superconductor, an insulator or a normal metal. Josephson predicted that a phase difference of the Ginsberg-Landau wavefunction across the junction gives rise to a supercurrent and that applying a voltage across the junction makes the phase evolve with time. These are the DC and AC Josephson equations [53, 54]

$$I = I_c \sin\phi \tag{4.1}$$

$$d\phi/dt = \frac{2eV}{\hbar}, \tag{4.2}$$

for which ϕ is the phase *difference* of the wavefunction across the junction and I_c is the critical current of the junction, the maximum supercurrent the junction can support. These two equations show that a voltage biased junction creates an alternating current of amplitude I_c at the Josephson frequency $\nu_J = 2eV/h$. Notice the quantum energy $h\nu$ equals the energy required to move a Cooper pair (the superconducting charge carrier of electrical charge $2e$) across the junction.

Tinkham [55] notes that ϕ is not a gauge-invariant quantity and as such cannot determine a unique value of I (which is a gauge-invariant quantity) for all physical situations. This is remedied by replacing ϕ with the gauge-invariant phase difference γ

$$\gamma \equiv \phi - 2e/\hbar \int \mathbf{A} \cdot d\mathbf{l}, \tag{4.3}$$

where $\mathbf{A}$ is the magnetic vector potential. γ and ϕ are identical in the absence of a magnetic field; however, this distinction will be important for the description of the DC SQUID in Sec. 4.1.3.

Eqs. 4.1 and 4.2 describe the ideal Josephson junction at T=0 with no parasitic capacitance and no dissipation in the finite voltage regime. Real junctions require a more complete description, which is provided by the resistively and capacitively shunted junction (RCSJ) model. In this model, the junction is replaced by an ideal

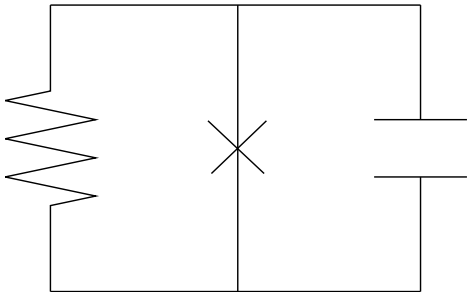

Figure 4.1: Electrical schematic for the resistively and capacitively shunted junction (RCSJ) model for a Josephson junction. The Josephson junction is represented by an 'x.' This model is used to describe the Josephson junction in the finite voltage regime.

Josephson junction described by Eq. 4.1 with a resistance R and capacitance C in parallel with the junction as shown in Fig. 4.1. The resistance allows for dissipation in the finite voltage regime, and C reflects the capacitance between the two superconductors on either side of the junction. If an external current I is supplied, the current through the RCSJ model is

$$I = CdV/dt + V/R + I_c \sin\phi. \tag{4.4}$$

The time evolution of the phase can be found by eliminating V in favor of ϕ according to Eq. 4.2. Doing so yields the basic result of the RCSJ model

$$I/I_c = \frac{\hbar C}{2eI_c}\ddot{\phi} + \frac{\hbar}{2eI_cR}\dot{\phi} + \sin\phi. \tag{4.5}$$

Qualitative insight of the junction dynamics described by solutions to Eq. 4.5 is often obtained by the "tilted-washboard" model, which points out that this equation of motion is the same as that of a particle of mass $(\hbar/2e)^2C$ moving along the ϕ axis in an effective tilted-washboard potential and subjected to a viscous drag force. However, in order to describe the DC SQUID, we only need to consider the over-damped case in which we neglect the $\ddot{\phi}$ term. This approximation is justified when the damping parameter $\beta_c = 2eI_cR^2C/\hbar$ [56, 57] (the inverse of

the constant multiplying the $\dot{\phi}$ term) is small. In practice this is accomplished by making C small . In the over-damped case, the time evolution of the phase is described by the following first order differential equation:

$$\frac{d\phi}{dt} = \frac{2eI_cR}{\hbar}\left(I/I_c - \sin\phi\right). \tag{4.6}$$

The time averaged voltage from Eq. 4.6 is

$$V = R\left(I^2 - I_c^2\right)^2, \tag{4.7}$$

which smoothly transitions from V=0 when superconducting to Ohm's law when $I \gg I_c$. Eq. 4.7 comprises one half of the description of the DC SQUID. The other half is flux quantization in a superconducting loop.

4.1.2 Flux quantization

In this section, we show that the magnetic flux threading a superconducting loop is quantized in units of the flux quanta ($\Phi_o = h/2e$). This phenomenon is a direct result of the Meissner effect (magnetic fields inside a superconductor are exponentially screened) and that the wavefunction must be single valued. The magnetic flux through any loop is

$$\Phi = \int \mathbf{B}\cdot d\mathbf{a} = \oint \mathbf{A}\cdot d\mathbf{l}. \tag{4.8}$$

Deep inside a superconductor, the Meissner effect ensures that the current density is zero. From which it follows [58]

$$\nabla\varphi = 2e/\hbar\mathbf{A}, \tag{4.9}$$

where φ is the phase of the Ginzberg-Landau wavefunction. Since the wavefunction must be single valued,

$$\oint \nabla\varphi\cdot d\mathbf{l} = 2\pi n. \tag{4.10}$$

Combining Eqs. 4.8 4.9 and 4.10, we find that flux is quantized in n integer units of Φ_o:

$$\Phi \;=\; \oint \mathbf{A}\cdot d\mathbf{l} = \hbar/2e\oint\nabla\varphi\cdot d\mathbf{l} = \frac{\hbar}{2e}2\pi n = n\Phi_o. \tag{4.11}$$

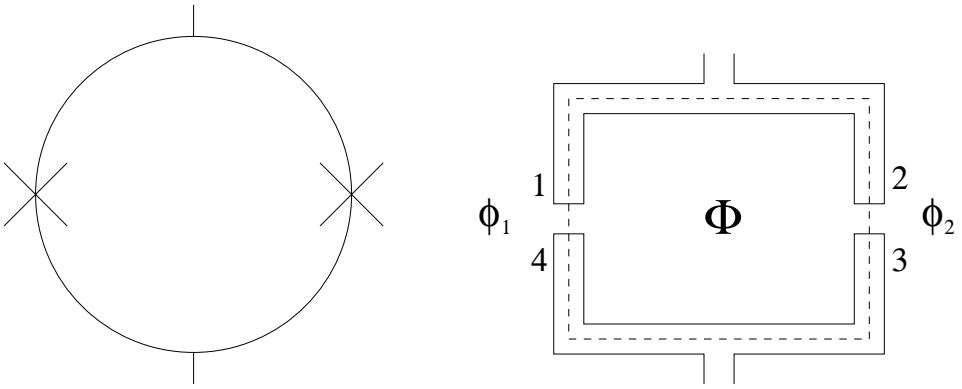

Figure 4.2: **Left:** Electrical schematic of the DC SQUID. Each junction is considered an over-damped RCSJ. **Right** Cartoon diagram of a DC SQUID. The dotted line is the path integral used to calculate the enclosed flux Φ. ϕ_1 and ϕ_2 are the Ginzberg-Landau phase differences across each Josephson junction.

4.1.3 DC SQUID

We are now in a position to quantify how the DC SQUID transduces magnetic flux to voltage. The DC SQUID uses two Josephson junctions in parallel integrated into a superconducting loop as shown in Fig. 4.2.

Consider the magnetic flux penetrating the loop in Fig. 4.2 by taking the line integral of the vector potential around the loop through the junctions,

$$\Phi = \oint \mathbf{A} \cdot d\mathbf{l} = \int_1^2 \mathbf{A} \cdot d\mathbf{l} + \int_2^3 \mathbf{A} \cdot d\mathbf{l} + \int_3^4 \mathbf{A} \cdot d\mathbf{l} + \int_4^1 \mathbf{A} \cdot d\mathbf{l} \qquad (4.12)$$

$$= \Phi_o/2\pi \int_1^2 \nabla\varphi \cdot d\mathbf{l} + \Phi_o/2\pi \int_3^4 \nabla\varphi \cdot d\mathbf{l} + \int_2^3 \mathbf{A} \cdot d\mathbf{l} + \int_4^1 \mathbf{A} \cdot d\mathbf{l}. \qquad (4.13)$$

The closed loop line integral has contributions from the superconducting electrodes (paths 1 to 2 and 3 to 4) and from the junctions (paths 2 to 3 and 4 to 1). Drawing on the development of Sec. 4.1.2, we replaced $\mathbf{A}$ with $\Phi_o/2\pi\nabla\varphi$ for the bulk superconductors if the line integral is taken deep within the interior of the superconductor. Also, the closed line integral of $\nabla\varphi$ must equal zero modulo 2π.

In this case however, the junctions contribute to the integral

$$\oint \nabla\phi \cdot d\mathbf{l} = \int_1^2 \nabla\varphi \cdot d\mathbf{l} + \int_3^4 \nabla\varphi \cdot d\mathbf{l} + \int_2^3 \nabla\varphi \cdot d\mathbf{l} + \int_4^1 \nabla\varphi \cdot d\mathbf{l} \quad (4.14)$$

$$= \int_1^2 \nabla\varphi \cdot d\mathbf{l} + \int_3^4 \nabla\varphi \cdot d\mathbf{l} + \phi_1 - \phi_2 = 2\pi n. \quad (4.15)$$

We see that the contributions from the electrodes equals 0 module 2π minus the sum of the phase differences across the junctions as defined in Fig. 4.2. Substituting this result in Eq. 4.13 we find

$$\frac{2\pi\Phi}{\Phi_o} = 2\pi n + \phi_2 - \Phi_o/2\pi \int_4^1 \mathbf{A} \cdot d\mathbf{l} - (\phi_1 - \Phi_o/2\pi \int_3^2 \mathbf{A} \cdot d\mathbf{l}) \quad (4.16)$$

$$= 2\pi n + \gamma_2 - \gamma_1, \quad (4.17)$$

where we have used the gauge-invariant phase γ defined in Eq. 4.3. This result shows that the difference between the gauge invariant phase differences of the two Josephson junctions is modulated by the external flux,

$$\gamma_2 - \gamma_1 = \frac{2\pi\Phi}{\Phi_o} - 2\pi n. \quad (4.18)$$

The total current flowing through the DC SQUID is

$$I_{sq} = I_{c1} \sin\gamma_1 + I_{c2} \sin(\gamma_1 - 2\pi\Phi/\Phi_o), \quad (4.19)$$

and the maximum supercurrent supported by the DC SQUID is

$$I_m = \left((I_{c1} - I_{c2})^2 + 4I_{c1}I_{c2}\cos^2 2\pi\Phi/\Phi_o\right)^{1/2}. \quad (4.20)$$

The structure of Eq. 4.20 is nearly identical to the intensity pattern formed from the double slit experiment in optics. Φ is analogous to the x-position of the image and the slit separation is analogous to Φ_o. This equation shows that the effective critical current of the DC SQUID is modulated by the applied flux. The voltage dependence of applied flux assuming the two junctions are identical is found by substituting Eq. 4.20 into Eqs. 4.7

$$V = \frac{IR}{2}\sqrt{1 - (2I_c/I\cos\pi\Phi/\Phi_o)^2} \quad (4.21)$$

$$= \frac{IR}{2}\sqrt{1 - I_c/I - I_c/I\cos 2\pi\Phi/\Phi_o}. \quad (4.22)$$

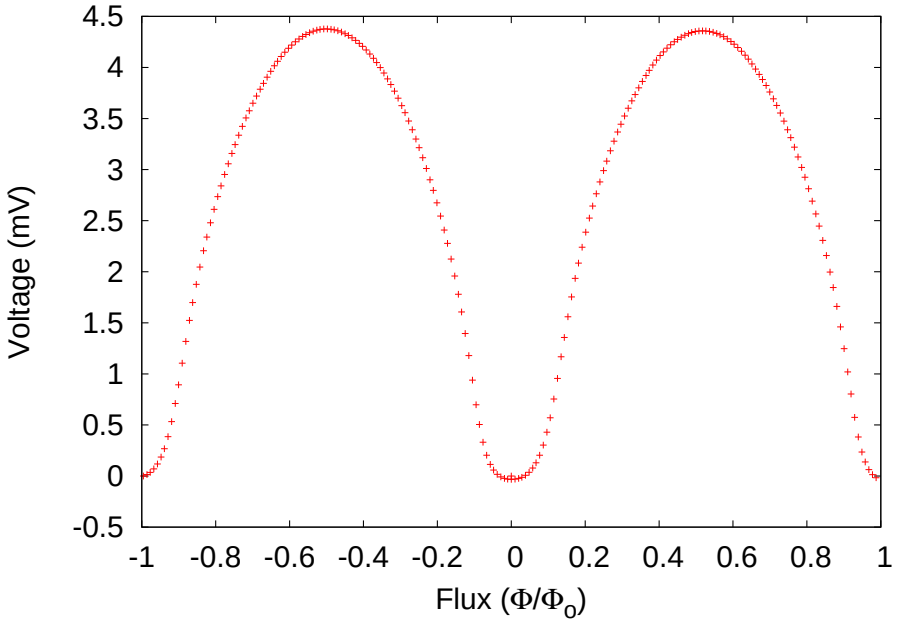

Figure 4.3: Measured voltage response of a SQUID, with offset removed, showing modulation to an applied flux with a period of Φ_o as derived in Eq. 4.21.

Eq. 4.21 shows the usefulness of the DC SQUID. The DC SQUID can measure magnetic flux with resolution to fractions of the flux quanta. Fig. 4.3 shows the measured voltage versus flux response of an EBEX DC SQUID.

4.2 Series array SQUIDs

A series array SQUID shown in Fig. 4.4 consists of N DC SQUIDs wired in series. We show that a series array with total input inductance L has $\sqrt{N}$ larger transimpedance ($Z = \frac{dV}{dI}$) and dynamic range than a conventional single SQUID with input inductance L. The signal to noise ratio of the two is the same.

A single SQUID with input inductance L, SQUID inductance L_{sq}, mutual inductance $M = \sqrt{LL_{sq}}$ and flux-to-voltage conversion $\frac{dV}{d\phi}$ produces an output

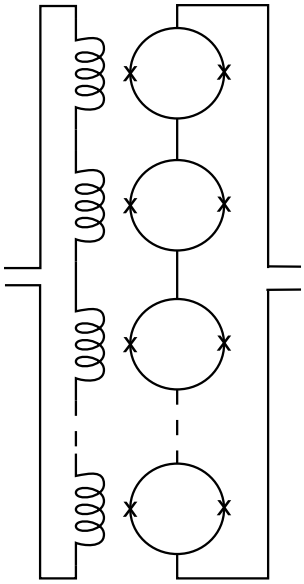

Figure 4.4: Schematic of series array SQUID amplifier. The signal to noise ratio increases by the square root of the number of SQUIDs over a single SQUID.

voltage to a signal current I of

$$V_s = IM\frac{dV}{d\phi}. \tag{4.23}$$

Now consider a series array with total input inductance the same as the single SQUID, L. The mutual inductance of each SQUID in the array is $M_i = \sqrt{LL_{sq}/N} = M/\sqrt{N}$. The voltage response of the series array to the same signal current I is

$$V_{sa} = NIM_i\frac{dV}{d\phi} = \sqrt{N}V_s. \tag{4.24}$$

We see the series array produces a voltage response a factor $\sqrt{N}$ larger than a single SQUID. Stated differently, the transimpedance of the series array is $\sqrt{N}$ larger.

If there is a maximum allowable flux Φ_{max} in each SQUID in the array, the

maximum input current for an array is

$$I_{max} = \frac{\Phi_{max}}{M_i} = \sqrt{N}\frac{\Phi_{max}}{M}. \tag{4.25}$$

Thus the dynamic range of the series array is $\sqrt{N}$ larger than for a single squid with mutual inductance M.

While the voltage response of the series array is $\sqrt{N}$ higher than a single SQUID, the signal to noise ratio is the same. If the single SQUID produces a voltage noise V_N, the series array produces an output voltage $\sqrt{N}V_N$ since the noise of each SQUID is the array is uncorrelated. This factor increase in the noise exactly cancels the voltage increase.

EBEX uses 100 series array SQUIDs [43] with 8-turn input coils fabricated by the National Institute of Standards and Technology (NIST) . The parameters of these devices are listed in Appendix C. For the rest of the thesis, a SQUID refers to a 100 series array SQUID unless otherwise noted.

4.3 Flux-locked loop

We operate the SQUID in shunt feedback with a flux-locked loop (FLL). Feedback increases the SQUID dynamic range and linearity. We use the block diagram in Fig. 4.5 to calculate the FLL transimpedance $Z_{sq} \equiv V/I$. The input current I is converted to a voltage and amplified by gain G. A fraction of the output voltage is fed back to the summing junction $\sum$ through $\frac{dI_{fb}}{dV}$. The output voltage is

$$V = (I + I_{fb})\frac{dV}{dI}G \tag{4.26}$$

$$= I\frac{\frac{dV}{dI}G}{1 - \frac{dV}{dI}\frac{dI_{fb}}{dV}G}. \tag{4.27}$$

For EBEX, an inductor and SQUID form the conversion of the signal to voltage $\frac{dV}{dI} = \frac{d\phi}{dI}\frac{dV}{d\phi} = M\frac{dV}{d\phi}$ in which M is the mutual inductance of the SQUID and $\frac{dV}{d\phi}$ is the slope of the SQUID $V - \phi$ curve. The feedback element is a resistor, $\frac{dI_{fb}}{dV} = 1/R_{fb}$. Substituting these expressions into Eq. 4.26 yields the FLL

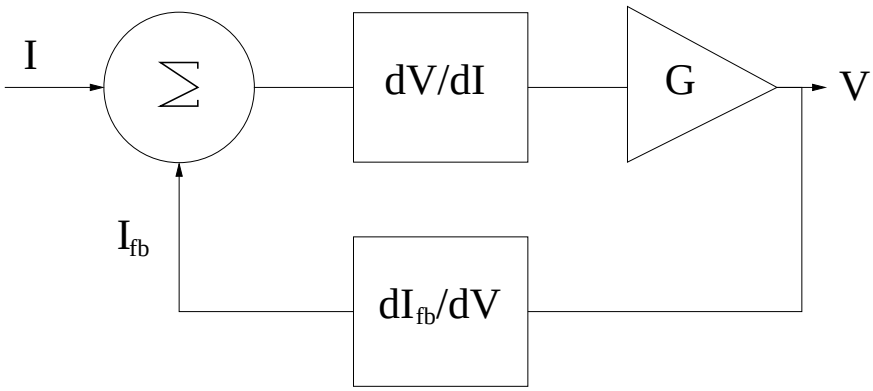

Figure 4.5: Diagram illustrating the SQUID shunt feedback, flux-locked loop.

transimpedance.

$$Z = \frac{M\frac{dV}{d\phi}G}{1 - M/R_{fb}\frac{dV}{d\phi}G} = \frac{M\frac{dV}{d\phi}G}{1-\mathcal{L}} \tag{4.28}$$

Notice that when the loopgain $\mathcal{L} = M/R_{fb}\frac{dV}{d\phi}G$ is high, $|Z| \approx |R_{fb}|$. We can change Z and $\mathcal{L}$ by a choice of three feedback resistors 10 K, 5 K and 3.3 K. Table 4.1 lists the loopgain for each feedback resistor setting.

R_{fb}	$\mathcal{L}$
10 K	13
5 K	26
3.3 K	40

Table 4.1: Loopgain as a function of feedback resistors. These values are calculated assuming $1/M = 26\mu A/\phi_o$, $\frac{dV}{d\phi}$ = -4π mV/ϕ_o and $G = 270$

4.3.1 Frequency dependence

A realistic treatment of the FLL transimpedance involves frequency dependence due to amplifier $G(\nu)$ and the use of a 'lead-lag' filter. This filter attenuates the

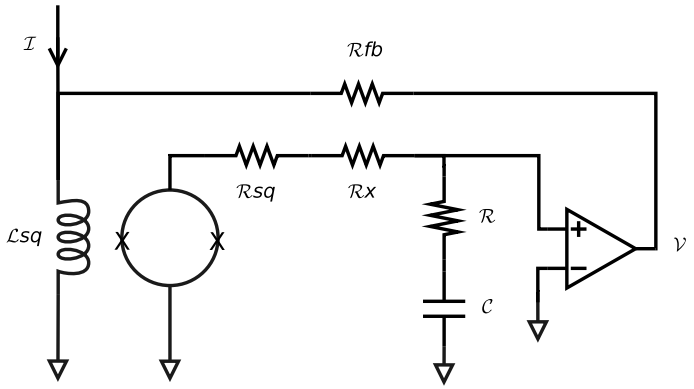

Figure 4.6: Schematic used to calculate the realistic SQUID flux-locked loop transimpedance including the 'lead-lag' filter. The terms are discussed in the text.

loopgain at frequencies above the signal bandwidth to avoid amplifying resonant frequencies in the system [59]. Fig. 4.6 shows the electrical schematic used to calculate the frequency dependent loopgain and transimpedance. Current is coupled to the SQUID with an inductor. R_{sq} is the output impedance of the SQUID, R_x is the warm to cold wiring resistance and R and C make up the lead-lag filter. From this schematic the transfer function is

$$Z = M \frac{\frac{dV}{d\phi}\frac{1+i\omega\tau_1}{1+i\omega\tau_2}\frac{G}{1+i\omega\tau_3}}{1 - M/R_{fb}\frac{dV}{d\phi}\frac{1+i\omega\tau_1}{1+i\omega\tau_2}\frac{G}{1+i\omega\tau_3}}, \tag{4.29}$$

where $\tau_1 = RC$, $\tau_2 = (R_{sq} + R_x + R)C$ and τ_3 is the time constant associated with the amplifier, whose frequency response is modeled as a single pole response with DC gain G. Fig. 4.7 shows the expected performance of the EBEX flux-locked loop. Across the fMUX bandwidth (300-1000 kHz), while the loopgain varies by almost a factor of 2, the transfer function varies by less than 4%. Fig. 4.8 shows the loopgain of eight SQUIDs measured in the EBEX cryostat and a frequency response predicted from the circuit model that matches the data well.

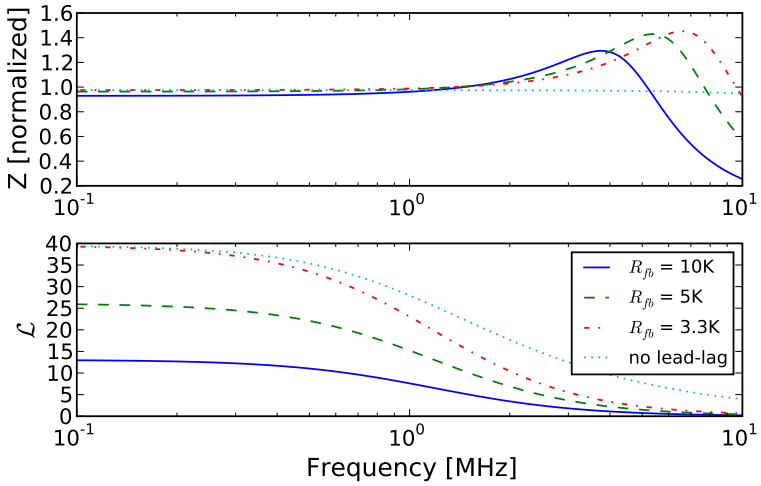

Figure 4.7: **Top:** Predicted transfer function of the EBEX SQUID flux-locked loop for each feedback resistor setting. **Bottom:** Predicted loopgain for each feedback setting. The calculation assumes a lead lag filter with components $R = 10\Omega$ and $C = 1nF$ with $R_{sq} = 80\Omega$ and $R_x = 20\Omega$, typical for EBEX.

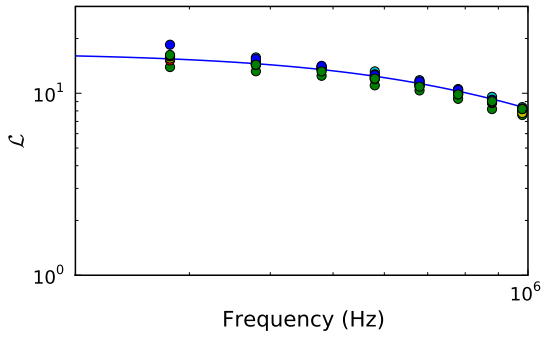

Figure 4.8: Loopgain measurements of eight SQUIDs and a model assuming $R = 10\ \Omega$, $R_x = 20\ \Omega$, $R_{sq} = 80\ \Omega$ and $C = 1.75$ nF.

Chapter 5

Frequency Domain Multiplexing

In Chapter 4, we detailed the theory of SQUID operation including the flux-locked loop feedback circuit. In EBEX, we use this SQUID circuit in a $\sim$ MHz frequency domain multiplexing (fMUX) architecture in which a single SQUID array reads out N TES bolometers. Multiplexing enables us to read out the $\sim$ 1000 bolometer of EBEX, where otherwise the number of wires running from the 4 K SQUIDs to the 270 mK bolometers produces an intolerable level of heat load on the sub-Kelvin cooler.

In this chapter, we explain the principle of fMUX in Sec. 5.1, describe digital frequency domain multiplexing (DfMUX) in Sec. 5.2, calculate the readout white noise level in Sec. 5.3, discuss how the fMUX departs from an ideal current readout in Sec. 5.5 and fit network analyses to a circuit model in order to extract network parameters used to correct for the non-idealities in Sec. 5.6.

5.1 fMUX Principle

Frequency domain multiplexing is detailed in [60, 61, 62, 63, 64]. We briefly describe the concept here. An electrical schematic of the readout system is shown in Fig. 5.1. The $\sim$ 1 Ω transition edge sensors of the bolometer array are placed in series with band defining LC filters. The LCR circuits are wired in parallel to

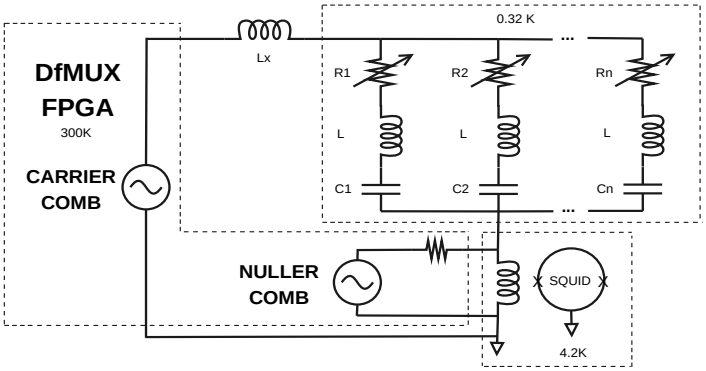

Figure 5.1: Electrical schematic of the fMUX readout system.

create a multiplexed module. A comb of sine wave carriers between 200 kHz - 1 MHz voltage biases each sensor in the module at its LC resonant frequency. Sky intensity changes the sensor resistance and amplitude modulates the carrier transferring signals to the side-bands of each carrier. Thus each sensor response is well defined in frequency space. Currents from all sensors within the module are carried on a single pair of wires to a SQUID ammeter. Warm electronics are used to lock in on the carrier frequency of each sensor with a bandwidth that contains the sky signal.

The large carrier amplitudes of the module present a flux burden on the SQUID. Since there is no sky signal at the carrier frequencies, they can be removed. A nuller comb consisting of sine wave currents 180 degrees out of phase with each carrier frequency is summed at the SQUID input. This nuller comb removes the unmodulated carrier amplitudes reducing the dynamic range requirement of the SQUID and improving linearity.

Figure 5.2: The digital frequency domain multiplexer (DfMUX) readout board used to tune, bias and monitor the detector and readout system. One board can readout 128 bolometers and dissipates 16W.

5.2 Digital fMUX

EBEX uses digital frequency domain multiplexer (DfMUX) electronics [44] in its implementation of frequency domain multiplexing. The DfMUX boards are a drop-in replacement for the analog fMUX boards designed to consume substantially less power and improve low frequency noise performance. The DfMUX board shown in Fig. 5.2 produces the sine wave carrier and nuller combs digitally with a Xilinx Virtex4 LX160 FPGA. The SQUID output is directly digitized with an ADC operating at 25 MHz. Sky signal from each bolometer is then digitally demodulated with a set of parallel algorithms that use a pseudo sine-wave mixer and a series of cascading filters.

Placing sine wave generation and signal demodulation in the digital domain achieves substantial power savings over the previous implementation of the frequency multiplexing system, which performed these functions in the analog domain. The power consumption of one DfMUX board is 16 W and is capable of reading out four modules with multiplexing factors of 32. The DfMUX system is therefore capable of dissipating as little as 125 mW per detector. However, the

multiplexer bandwidth is currently limited by the cold components of the system. Using a multiplexing factor of 16 to readout 1920 detectors, as is planned for EBEX, the power consumption of the readout system is 565 W, which includes a 15% loss of efficiency in power delivery. This level of power consumption satisfies the EBEX power budget constraints.

The DfMUX boards contain a set of algorithms to tune and monitor the SQUIDs and detectors [65]. This functionality is essential for commanding the readout system remotely during a balloon flight.

5.3 Noise sources in the DfMUX readout

Fig. 5.3 shows an electrical schematic used to calculated the expected readout noise. We define readout noise as the combined Johnson and current shot noise from all the warm and cold readout electronics shown in this diagram. Johnson noise terms are summarized in Tab. 5.1. Current shot noise terms are tallied in Tab. 5.2. The largest contributor to the readout noise is the 0.03 Ω bias resistor (R_b) which provides the bolometer voltage bias and is located on the 4 K SQUID mounting board.

Noise sources in the readout system fall under two categories: broad-band noise sources and narrow-band noise sources. Broad-band sources contribute across the entire MUX bandwidth (200-1000 kHz), whereas narrow-band noise sources are attenuated at frequencies away from the LC resonance. This distinction is important because broad and narrow-band noise sources transfer differently through a square-wave mixer which was used early versions of the DfMUX demodulator. For the EBEX NAF, we used a pseudo-sinusoidal mixer, in which case the two types of noise sources transfer identically. In this case, the white noise level is artificially increased by $\sqrt{2}$ because noise is 'amplified' over signal through the mixer (see Appendix B.1). Using a sinusoidal mixer, the expected readout noise level is:

$$N_{readout} = \sqrt{2}\sqrt{N_{J_b}^2 + N_{I_b}^2 + N_{J_n}^2 + N_{I_n}^2} \tag{5.1}$$

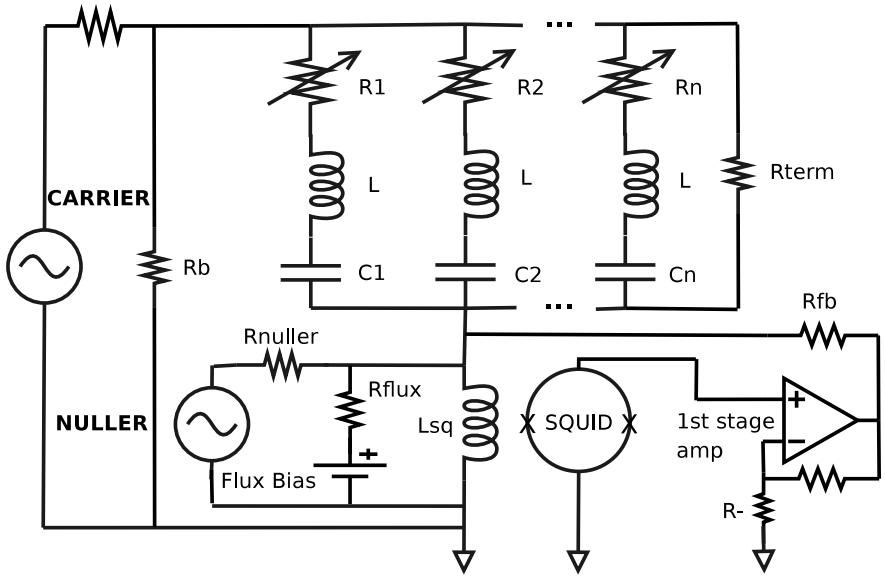

Figure 5.3: Schematic used to calculate the expected readout noise level from the fMUX readout.

$$= \sqrt{2}\sqrt{4.5^2 + 2.0^2 + 5.3^2 + 0.8^2} \quad (5.2)$$

$$= 10.3\ pA_{rms}\sqrt{Hz}, \quad (5.3)$$

referred to the squid input coil. Here the subscripts J and I refer to Johnson and current noise respectively and the subscripts b and n correspond to broad-band and narrow-band noise sources.

5.4 Bandwidths and electrical cross-talk

The MUX bandwidth spans 200-1000 kHz. The low edge of the band is constrained by the TES time constant τ_{et}. The AC bias frequency ν must satisfy $\nu \gg (2\pi\tau_{et})^{-1}$, otherwise the TES will response to the bias. The upper edge of the MUX bandwidth is constrained by the gain-bandwidth product of the SQUID

Table 5.1: Johnson noise readout terms

Noise Source	type	T (K)	R (Ω)	equation	current noise ($pA_{rms}/\sqrt{Hz}$)
R_{term}	b	0.25	50	$N_j(R_{term})/R_{term}$	0.5
R_b	n	4.2	0.03	$N_j(R_b)/R_{bolo}$	5.3
SQUID	b	4.2	100	NA	2.5
R_{nuller}	b	300	3,250	$N_j(R_{nuller})/R_{nuller}$	2.1
R_{flux}	b	300	50,000	$N_j(R_{fb})/R_{fb}$	0.6
R_{fb}	b	300	5,000	$N_j(R_{fb})/R_{fb}$	1.8
R_-	b	300	20	$N_j(R_-)/Z_{sq}$	1.2
1^{st} stage amp	b	300	NA	1 $nV_{rms}/\sqrt{Hz}/Z_{sq}$	2
total noise					7.3

$Z_{sq} = 500\Omega$, the SQUID transimpedance and $R_{bolo} = 0.5\Omega$, the bolometer resistance.

feedback flux-locked loop. Currently, the major inhibitor to increasing the bandwidth is the wire length between the 4 K SQUIDs and the 300 K 1^{st} stage amplifier.

The electrical bandwidth per TES within 200-1000 kHz is $BW_e = L/R$, where L is the inductance in series with a bolometer of resistance R. For stability, the electrical bandwidth must satisfy the following inequality [42]

$$BW > \frac{5.8}{2\pi\tau_{ef}}. \tag{5.4}$$

The frequency spacing between bolometers is constrained by Eq. 5.4 and the allowable cross-talk between adjacent RLC channels. The finite bandwidth of the tuned filters allows currents to flow through off-resonance channels [61]. The changing resistance of the off resonance bolometer to an optical signal modules the current producing a source of cross talk. The level of cross talk, which we define as the on resonance modulated current to off-resonance, is

$$X = \left(\frac{R}{\sqrt{R^2 + (\omega L_i - 1/\omega C_i)^2}} \right)^3, \tag{5.5}$$

Table 5.2: Current shot noise terms in readout

Current Source	noise type	Current (μA_{rms})	Equation	Current Noise ($pA_{rms}/\sqrt{Hz}$)
Bolometer bias	n	2	$N_s(I)$	0.8
Nulling	b	2	$N_s(I)$	0.8
SQUID flux bias	b	6	$N_s(I)$	1.4
SQUID current bias	b	100	$N_s(I) \times R_{sq}/Z_{sq}$	1.1
total noise				2.1

$R_{sq} = 100\Omega$, the SQUID resistance.

where L_i and C_i are the inductance and capacitance of the off resonance channel. For the NAF, we used 60 kHz spacing between resonance channels from 300 to 720 kHz, inductors of value $L \sim 16\ \mu H$ and bolometer resistance of R=0.7 Ω. The calculated total cross-talk from all off resonance channels is $< 5 \times 10^{-4}$. The cross-talk matrix X_{ij} of this network, where the element x_{ij} is the cross-talk at the frequency of the i^{th} on resonance frequency due to the j^{th} off-resonance channel is:

$$X_{ij} = \begin{pmatrix} 1.0 & 1.5e^{-4} & 1.4e^{-5} & 3.3e^{-6} & 1.1e^{-6} & 4.6e^{-7} & 2.2e^{-7} & 1.2e^{-7} \\ 2.5e^{-4} & 1.0 & 1.5e^{-4} & 1.5e^{-5} & 3.7e^{-6} & 1.3e^{-6} & 5.5e^{-7} & 2.7e^{-7} \\ 3.9e^{-5} & 2.4e^{-4} & 1.0 & 1.6e^{-4} & 1.6e^{-5} & 4.0e^{-6} & 1.4e^{-6} & 6.3e^{-7} \\ 1.3e^{-5} & 3.6e^{-5} & 2.4e^{-4} & 1.0 & 1.6e^{-4} & 1.7e^{-5} & 4.3e^{-6} & 1.6e^{-6} \\ 6.5e^{-6} & 1.2e^{-5} & 3.5e^{-5} & 2.3e^{-4} & 1.0 & 1.7e^{-4} & 1.8e^{-5} & 4.6e^{-6} \\ 3.7e^{-6} & 6.0e^{-6} & 1.2e^{-5} & 3.3e^{-5} & 2.3e^{-4} & 1.0 & 1.7e^{-4} & 1.8e^{-5} \\ 2.4e^{-6} & 3.4e^{-6} & 5.6e^{-6} & 1.1e^{-5} & 3.2e^{-5} & 2.2e^{-4} & 1.0 & 1.7e^{-4} \\ 1.6e^{-6} & 2.1e^{-6} & 3.1e^{-6} & 5.3e^{-6} & 1.1e^{-5} & 3.2e^{-5} & 2.2e^{-4} & 1.0 \end{pmatrix}$$

5.5 fMUX readout non-idealities

In this section, we consider how the fMUX system departs from providing an ideal voltage bias and current readout. We show that stray impedance in the system and a non-ideal voltage bias can produce $\sim 25\%$ error in determining the voltage bias and electrical power dissipated in the sensor if not accounted properly. This error goes directly into the determination of bolometer responsivity and optical loading, motivating the calculations below. We also show how these non-idealities change the shape of the bolometer IV curve.

5.5.1 Definition of correction factors

The ideal voltage bias creates a constant voltage across the TES regardless of its impedance. In practice the constant voltage is achieved by driving a constant current through a load consisting of the TES in parallel with a bias resistor R_b that has an impedance much less than that of the TES, R. In the limit $R_b << R$, the ideal voltage bias is

$$V = I_{in} R_b, \tag{5.6}$$

where I_{in} is the constant current. In the fMUX system, the non-zero value of R_b moves the voltage bias across the TES away from the value in Eq. 5.6. In addition, since the fMUX system uses AC bias at $\sim$ MHz frequencies, stray impedance causes the voltage bias to depart from ideal.

The measured current through the SQUID also differs from the current flowing through a particular TES due to leakage in off-resonant RLC channels. We calculate the voltage, current and power correction factor C_v, C_I and C_P respectively for several non-ideal terms in the fMUX system. We define these correction factors:

$$C_v = \frac{V_{tes}}{I_{in} R_b} \tag{5.7}$$

$$C_I = \frac{I_{tes}}{I_{measured}} \tag{5.8}$$

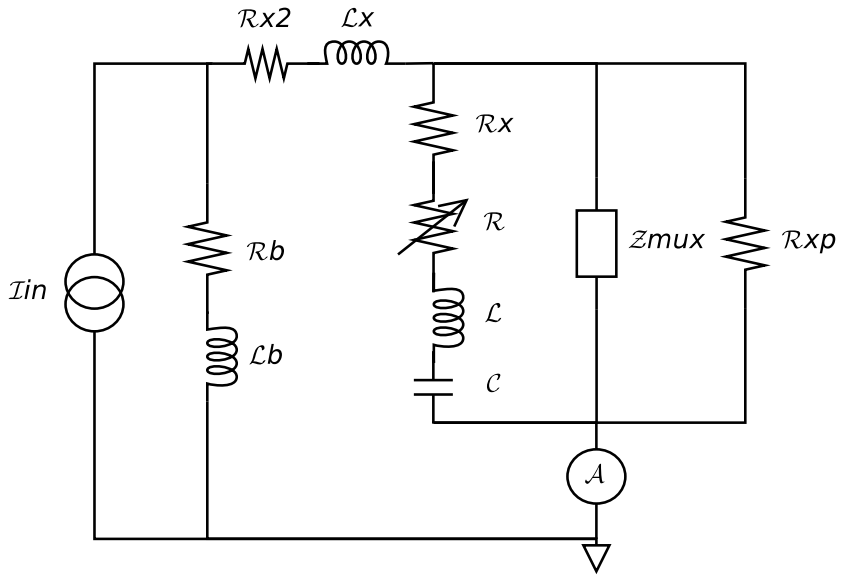

Figure 5.4: Electrical schematic of bias including non-idealities. Components are defined in the text.

$$C_P = C_v C_I. \tag{5.9}$$

The departure from unity of a correction factor may be viewed as the error incurred if the effect is not considered.

5.5.2 Circuit model

Fig. 5.4 shows the electrical schematic used to calculate the correction factors. An AC current of *rms* amplitude I_{in} largely runs through the bias resistor R_b creating a constant voltage bias across the TES of variable resistance R. The TES is in series with an LC resonant filter and multiplexed with all *other* RLC channels which have a Thevenin equivalent impedance Z_{mux}.The current produced by the multiplexed module is readout at A, shown as an ammeter in the schematic.

We include the following strays in the system: L_b the stray inductance of the bias resistor; R_{x2} and L_x are stray resistance and inductance in the wiring between

parameter	value
I_{in}	33 μA_{rms}
R_b	0.03 Ω
L_b	1.2 nH
R_{x2}	0
L_x	70 nH
R_x	0
R	0.7 Ω (in transition)
L	16 μH
R_{xp}	51 Ω
ν_o	280-1000 kHz
$\lvert Z_{mux}\rvert$	$\sim$ 3-5 Ω

Table 5.3: Nominal network parameters for EBEX.

the detectors and current readout; R_x is a stray resistance in series with the TES; and R_{xp} is the termination resistance of wiring between the detectors and readout. Table 5.3 lists the nominal magnitude of the model parameters for EBEX.

5.5.3 Calculation

We calculate C_v, C_I and C_P for the following individual terms: non-zero R_b, R_x, R_{x2}, L_b, off LC resonance, Z_{mux}, R_{xp} and L_x. In each case all other non-ideal terms are set to the ideal value, either 0 or ∞. In the subsections below, we give the analytical expression for the correction factors, list the source in the experiment which gives rise to the term and calculate the magnitude of the effect at $R = 0.7\ \Omega$, the nominal TES bias position during the NAF. For calculations that include Z_{mux}, we assume a network of eight resonant peaks spaced 50 kHz apart between 300 and 650 kHz. Table 5.4 summarizes the correction factors at $R = 0.7\ \Omega$. A range of values in the table shows the extremes within the frequency range 300-650 kHz.

non-ideality	C_v	C_I	C_p
finite R_b	0.959	1	0.959
R_x= 0.03 Ω	0.959	1	0.959
finite $R_b$and L_b= 1.2nH	0.962-0.989	1	0.962-0.989
ν-ν_o = 500 Hz	0.990	1	0.990
Z_{mux}+ finite R_b	0.959	0.989	0.948
R_{xp}= 50 Ω	0.958	0.986	0.945
L_x= 100 nH + Z_{mux}	1.003-.793	.989-.980	.992-.777

Table 5.4: Effect of the non-ideal terms on the voltage bias and measured current. In order to correct for the effect, the ideal voltage or measured current needs to be multiplied by C_v or C_I respectively. The power correction term $C_p = C_V C_I$.

Non-zero bias resistor R_b

The finite size of R_b will decrease the voltage across the TES relative to the ideal by

$$C_v = \frac{R}{R + R_b}. \tag{5.10}$$

For EBEX R_b= 0.03 Ω and $C_v \sim 4\%$, independent of frequency.

Bias resistor stray inductance L_b

The stray inductance of the bias resistor acts to *increase* the voltage bias across the TES. The voltage correction factor is

$$C_v = \frac{R_b + Z(L_b)}{R + R_b + Z(L_b)} \frac{R}{R_b}, \tag{5.11}$$

where $Z(\ L_b\ ) = j\omega L_b$. Measurements of L_b are 1.2 nH [66]. The voltage correction factor is frequency dependent and ranges from 0.989 to 0.962 over 300-650 kHz.

Stray resistance R_x in series with R

A non-zero R_x voltage divides with R decreasing the voltage bias across the TES by an amount

$$C_v = \frac{R}{R + R_x}. \tag{5.12}$$

If a finite bias resistor and a stray series resistance is considered, the voltage bias correction is

$$C_v = \frac{R}{R + R_x + R_b}. \tag{5.13}$$

Potential sources of R_x include wire-bond contacts, copper wire-bonding pads and solder joints of the surface mount capacitors. However; these sources should be negligible. We assume R_x= 0.03 Ω in Table 5.4 for illustrative purposes only. The voltage bias correction due to R_{x2} is identical to that due to R_x.

Bias frequency off LC resonance

Biasing the TES away from its LC resonance creates a voltage divider between the TES and the non-zero impedance of the LC filter. The voltage correction factor is

$$C_v = \frac{R}{\sqrt{R^2 + (\omega L - 1/\omega c)^2}}. \tag{5.14}$$

Our algorithms that select the bias frequencies to minimize inter-modulation products bias the detectors no further than 500 Hz off resonance, which results in a 1% decrease in voltage bias.

Finite impedance of off resonance bolometer channels Z_{mux}

The impedance of off resonant RLC channels lowers the Thevenin equivalent impedance of the multiplexed module. Thus when considering a non-zero bias resistor, the voltage correction factor due to Z_{mux} is not unity. The voltage

correction factor is frequency dependent. The presence of off resonant channels allows leakage current into $I_{measured}$. On resonance ω_o of the TES in question, the correction factors are

$$C_v = \frac{Z_{mux}(\omega_o)R}{RZ_{mux}(\omega_o) + R_b(R + Z_{mux}(\omega_o)} \quad (5.15)$$

$$C_I = \frac{Z_{mux}(\omega_o)}{R + Z_{mux}(\omega_o)}. \quad (5.16)$$

Multiplexing changes the conversion to power from ideal at the $\sim 5\%$ level for EBEX. This level depends on the spacing between resonances and the multiplexing factor.

Readout cable termination resistor R_{xp}

A 51 Ω resistor terminates the microstrip cable that connects the detectors to the current readout. This termination resistor damps resonances created by this cable but also creates a non-zero current and voltage correction factor

$$C_v = \frac{R_{xp}R}{R + R_b + R_{xp}} \quad (5.17)$$

$$C_I = \frac{R_{xp}}{R_{xp} + R}, \quad (5.18)$$

giving $C_v = 0.958$ and $C_I = 0.986$ for the EBEX system.

Stray impedance L_x in series with multiplexed module

The voltage correction factor on resonance ω_o is

$$C_v = \frac{RZ_{mux}(\omega_o)}{j\omega_o L_x(R + Z_{mux}(\omega_o)) + RZ_{mux}}, \quad (5.19)$$

while the current correction factor is identical to finite impedance of off resonance bolometer channels case. C_v is a strong function of frequency and is shown in Fig. 5.5. The voltage bias at 650 kHz is 20% less than the input voltage bias making strays associated with L_x the most problematic stray at high frequencies.

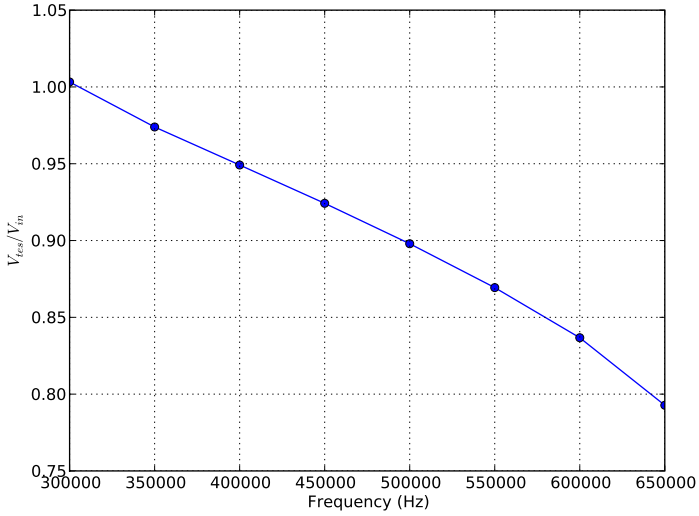

Figure 5.5: Effects of stray inductance L_x=100 nH on the voltage bias across the TES relative to the input voltage as a function of frequency. The stray inductance voltage divides with multiplexed module decreasing the bias across the TES. The reduction in voltage bias exceeds 20% at 650 kHz.

Stray inductance L_x comes from two main sources: 1) input inductance of the SQUID coil and 2) the microstrip cable connecting detectors to readout [67]. The inductance of the SQUID input coil is decreased by shunt feedback. The effective inductance is $L_{eff} = L_{in}/(1 + \mathcal{L})$, where L_{in} is the input inductance and $\mathcal{L}$ is the loopgain of the SQUID feedback loop. The cable inductance is more problematic. Because of the adverse effects of L_x, much effort has been made to produce a cable that minimizes L_x, while at the same time satisfies the cryogenic constraints.

Typical case for EBEX

The previous sections demonstrate the magnitude of each term individually. However, these effects are not independent. Using the values listed in Table 5.3, the fiducial correction factors for EBEX are shown in Fig. 5.6. The corrections are

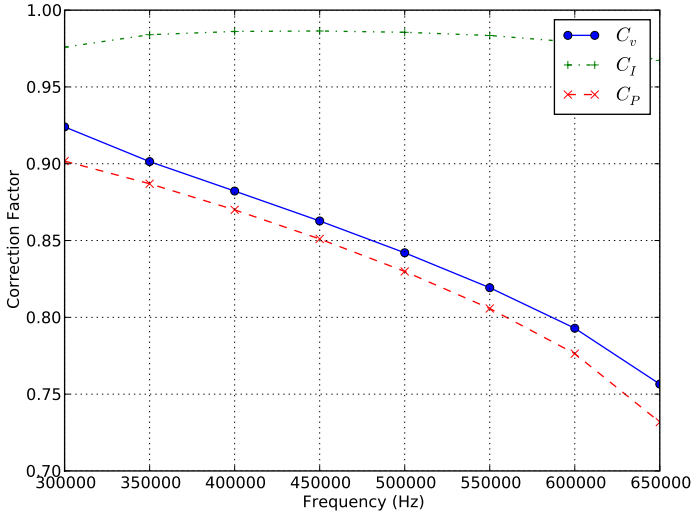

Figure 5.6: Fiducial EBEX correction factors that account for non-ideal impedance terms in the fMUX readout system.

frequency dependent and C_P ranges from 0.9 to below 0.75.

5.5.4 Effects on IV and PV curves

The non-ideal impedance terms can be seen in the current versus voltage (IV) and power versus voltage (PV) curves. The most notable effect is that voltage dividing terms produce a negative slope of the power in the transition (dP/dV), which is unphysical. Fig. 5.7 shows the calculated IV and PV curves for typical EBEX bolometer that is readout with the fMUX system and has L_x= 100 nH.

5.6 Network analysis fitting

Because of the systematic errors dealing with the non-idealities of the fMUX system described in Sec. 5.5, it is important to determine the network parameters

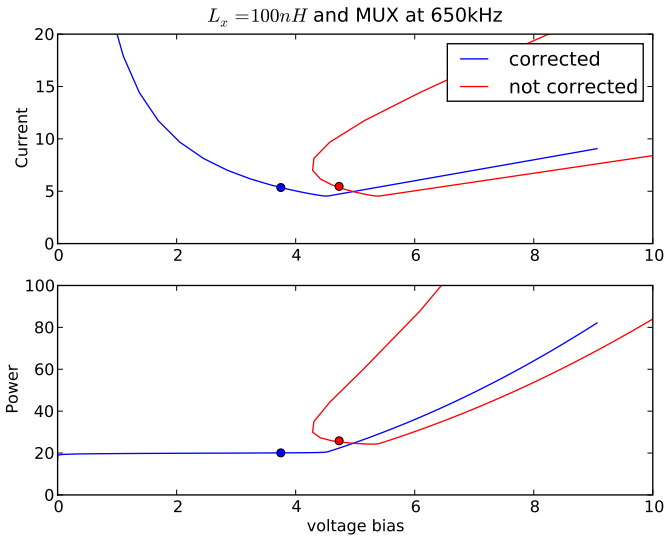

Figure 5.7: Simulated IV and PV curves for uncorrected and corrected stray inductance of L_x= 100 nH. All voltage dividing terms create a negative slope of the power in the transition.

so that the errors can be corrected. We determine the network parameters by performing a least squares fit of the network analysis to a circuit model with $2N$+2 free parameters, where N is the number of bolometers in the module. During a network analysis, the temperature of the bolometers is held above T_c, and a single sinusoidal voltage bias sweeps in frequency while the SQUID records the current response. Fig. 5.8 shows the circuit model used for the fit. The free parameters in the model include an overall voltage amplitude, stray inductance L_x, and a resistance R_i and inductance L_i for the i^{th} bolometer RLC channel. The measured 300 K value for each capacitance is kept constant as well as the 51 Ω termination resistance R_{xp}.

Fig. 5.9 shows an example network analysis fit and the residuals of the fit. The residuals of the fit are Gaussian and the reduced chi-squared is $\chi^2_{red} = 0.95$ with 18 free parameters and 387 degrees of freedom. $\chi^2_{red} < 1$ indicates that

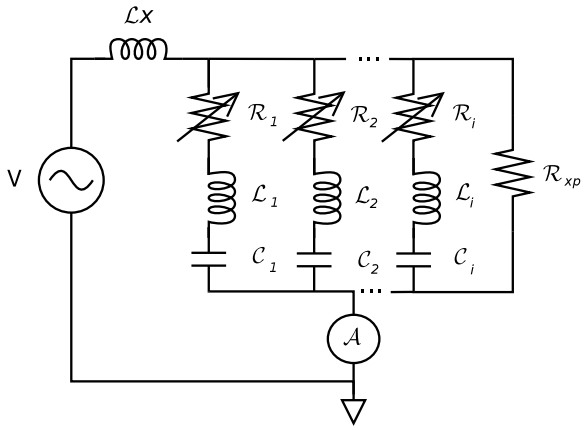

Figure 5.8: Electrical schematic used to fit the network analysis with 2N+1 free parameters with N bolometers in the module.

the variance of the data is slightly under-estimated. From the fit, we conclude the stray inductance in series with the module is 90 nH. The decreasing peak height with increasing frequency is the result of this stray inductance voltage dividing with the bias. The majority of the stray inductance comes from the wiring between the SQUIDs and bolometers; however at most 16 nH is due to the effective inductance of the SQUID input coil, $L_{eff} = L_{sq}/(1 + \mathcal{L})$, because the loopgain is finite.

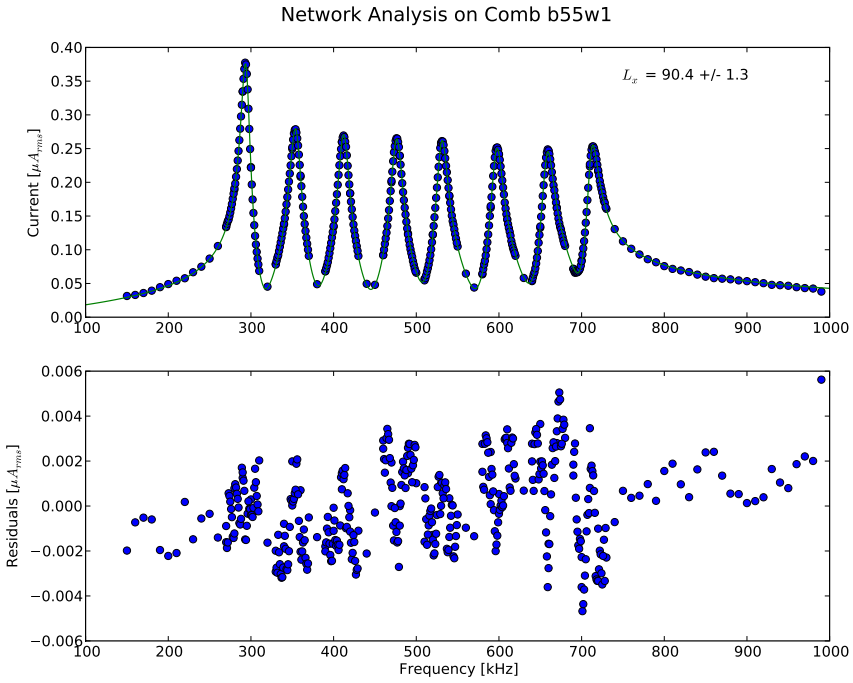

Figure 5.9: **Top:** An example network analysis fit on a multiplexed module in the NAF. **Bottom:** The residuals to the fit. $\chi^2_{red} = 0.95$ for 387 free parameters. The parameters determined from the fit can be used to correct the bolometer IV curves for further analysis.

Chapter 6

Proto-type EBEX bolometers

In this chapter, we detail measurements of proto-type EBEX bolometers taken with the digital frequency domain multiplexing (DfMUX) system. As a step in the implementation of $\bar{G}$=10 pW/K bolometers suitable for thermal loading at balloon altitudes, an array with bolometers with designed $\bar{G}$=32 pW/K has been fabricated. The measurements described in this chapter are the first demonstration of the DfMUX system reading out EBEX bolometers. Much of the following discussion appears in Hubmayr et al [68].

6.1 Bolometer array

The bolometer array is identical to the arrays described in Sec. 2.3.5 with two exceptions. The aluminum back-short is 500 μm; no wafer bonding was used for this array. The silicon nitride legs are 0.5 mm long, half the length of the standard EBEX isolating legs. This increases the expected thermal conductance. We predict the dynamic thermal conductance of the bolometers using $G = 4\sigma A T^3 \xi$ [69], where σ=15.7mW/cm^{2}K^4 and T is the temperature of the TES. We use the complete diffuse surface scattering limit known as the Casimir limit $\xi \approx \sqrt{A}/l$ which is valid for $\sqrt{A}/l \ll 1$. We predict G = 61 pW/K at T_c and $\bar{G}$=32 pW/K.

6.2 Experimental setup

The prototype bolometer array is heat-sunk to the baseplate of a ^{3}He adsorption refrigerator [37] operated at 320 mK. The array is enclosed in a dark cavity at the same temperature so that radiative loading is negligible. A Fairchild LED56 inside the dark cavity provides optical signals to the bolometers. Fig. 6.1 shows the experimental setup with the wafer mounted in a light tight box. Each bolometer is wired in series with a ceramic capacitor [70] and a 16 μH inductor fabricated by TRW. Using a multiplexing factor of three, the bolometers are read out with a 100 series array SQUID amplifier [43] operated in shunt feedback coupled to a room temperature amplifier located on a custom SQUID Controller electronics board [71]. The SQUID is heat-sunk to 4.2 K. The output of the SQUID is sent on a twisted pair to the demodulator of the DfMUX board.

6.3 Results

6.3.1 Network analysis

In order to determine the bias frequencies, normal resistance of the bolometers and the stray inductance in series with the module, we perform the network analysis shown in Fig. 6.2.

For this measurement, the cold stage is held above the TES transition at 800 mK, and a carrier voltage sweeps across the module in frequency. The three peaks at 438, 534 and 645 kHz are the LC resonant frequencies in series with sensors '11-01', '10-02' and '9-03' respectively. We fit the data to an analytic circuit model with $2n + 1$ free parameters where n is the number of bolometer channels. The inductors in series with each bolometer are fixed at 16 μH, and the voltage bias is fixed at 3.9 μV_{rms}. For each channel the normal resistance of the bolometer and the capacitance in series with the bolometer are to be determined from the fit. The stray inductance in series with the module L_x is also determined by the fit. The impedance of the stray inductance (ωL_x) creates a frequency

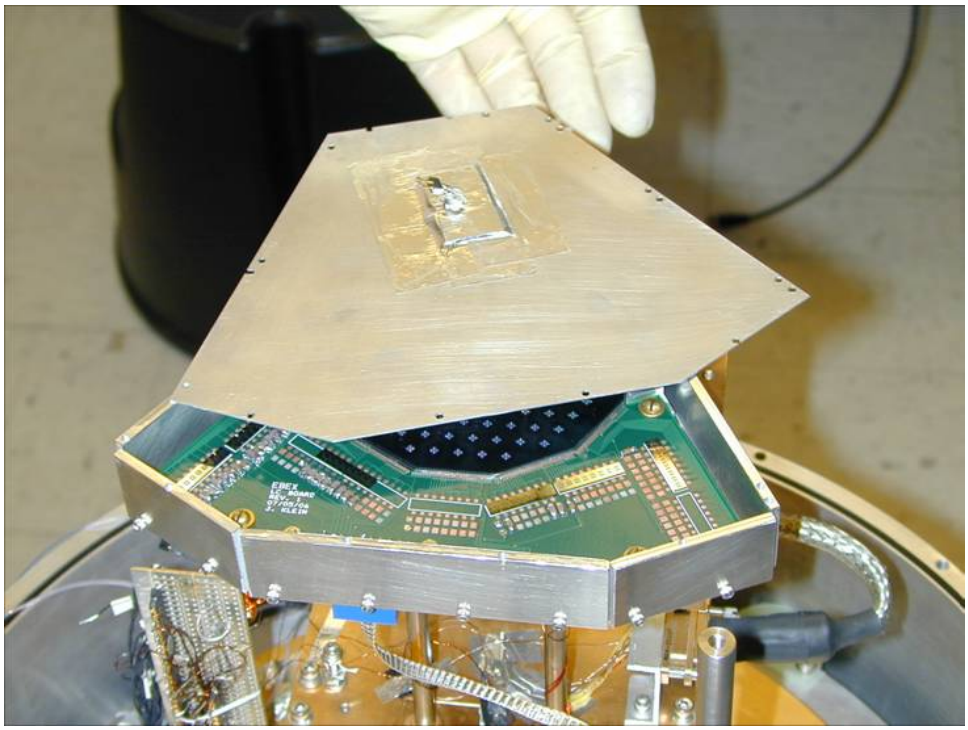

Figure 6.1: Experimental setup for the proto-type bolometer measurements. The bolometer array is seen above the green LC board. The LC board holds the band defining LC filters in series with each bolometer. The entire aluminum structure surrounds the bolometer array and is heat-sunk to 320 mK.

dependent voltage divider which is the source of the decreasing peak height with increasing frequency. Since the voltage bias of the bolometer (v) largely determines the responsivity of the device [72], it is important to determine L_x. From the fit, we determine that $R = 1.03$, 1.04 and 1.00 Ω for bolometers '11-01', '10-02' and '9-03' respectively, and $L_x = 149$ nH. For all TES, L_x affects the voltage bias by $< 10\%$. However, for subsequent measurements, we include $L_x = 149$ nH in our analysis.

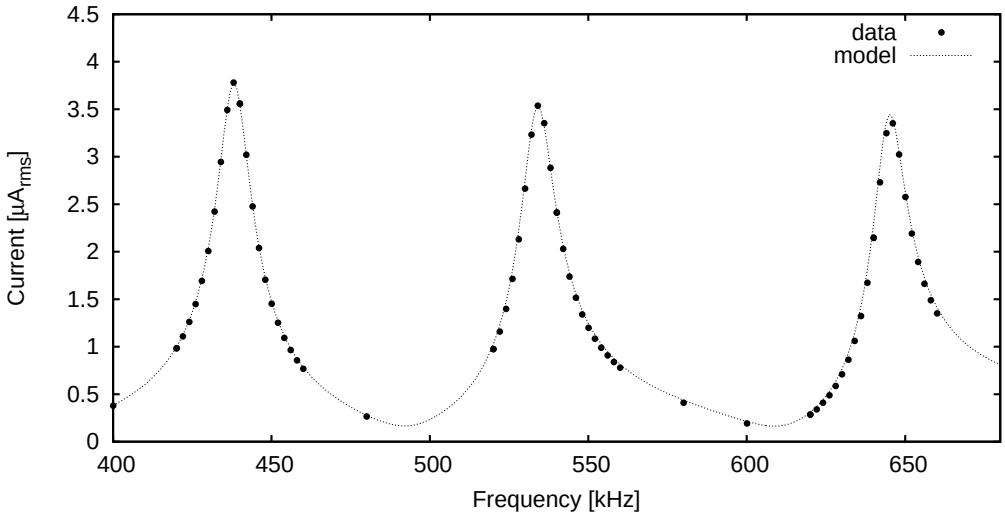

Figure 6.2: The network analysis of the multiplexed module. A fit to the analytic model shown by the dashed curve is used to determine the bias frequencies, resistance of the bolometers and the stray inductance in series with the module.

6.3.2 Thermal conductance

To determine the average thermal conductance of the bolometers ($\bar{G}$), we perform current versus voltage (IV) measurements of the three bolometers in the module. Each sensor is biased at its resonant frequency, the voltage is stepped down and the current through the SQUID is recorded. At voltage biases $> 3\mu V_{rms}$ shown in Fig. 6.3, the TES is normal and the IV curve is linear. The turnaround at $\sim 2.5\mu V_{rms}$ is evidence that the TES enters the superconducting transition. In the transition, the total power is constant due to strong electro-thermal feedback, and the current is proportional to the inverse of the voltage bias. The steady state power through the device is

$$P + P_e = \bar{G}(T - T_o), \tag{6.1}$$

where P is the radiative power, $P_e = v^2/R$ is the electrical power, $\bar{G}$ is the average thermal conductance, T is the temperature of the TES and T_o is the temperature

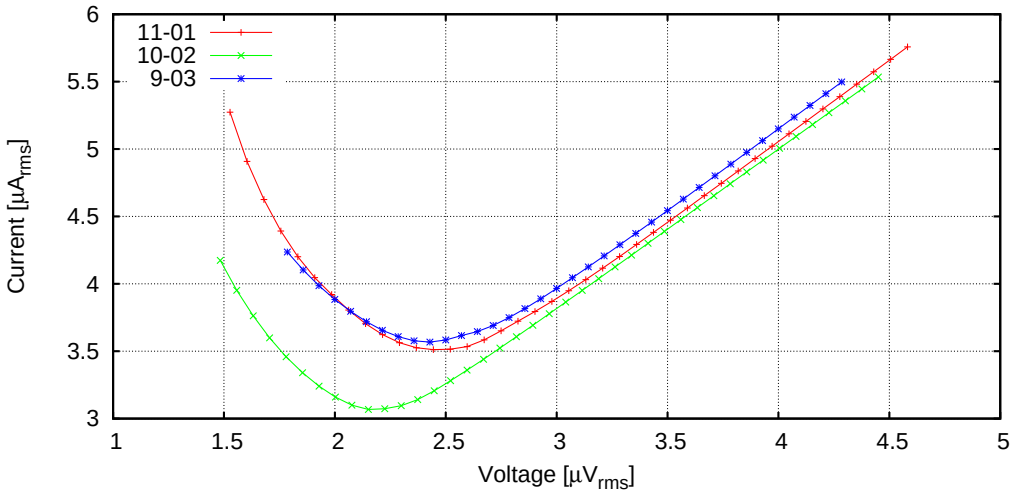

Figure 6.3: Current versus voltage curves for the bolometers in the module. The electrical power at the turnaround divided by $T_c - T_o$ gives $\bar{G} = 32$, 27 and 33 pW/K for the three devices.

of the heat-sink. Since the bolometers are operated within a dark enclosure, the data in Fig. 6.3 together with $T_c - T_o$ yield measurements of $\bar{G}$. We determine $T_c \sim 550$ mK by biasing the bolometers with $\sim 10\ nV_{rms}$ and monitoring the current response while slowly lowering the heat-sink temperature. We measure $\sim$ 32, 27 and 33 pW/K for bolometers '11-01', '10-02' and '9-03' respectively, which are in good agreement with the theoretically calculated $\bar{G} = 32$ pW/K.

6.3.3 Optical frequency response

We determine the bolometer response to optical signals by biasing the LED with a small sinusoidal current and measuring the bolometer amplitude response as a function of LED bias frequency. Figure 6.4 shows the frequency response of bolometer '9-03' biased at 0.8 Ω (black circles) and 0.5 Ω (blue asterisks). A single-pole fit gives optical time constants of 22 ms and 13 ms respectively. With feedhorns coupled to the bolometers we expect the response time to decrease by a

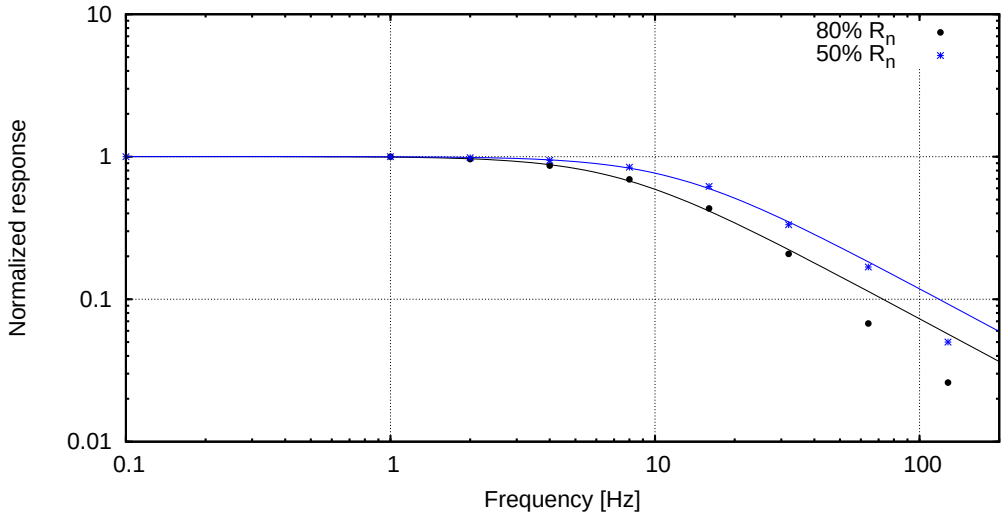

Figure 6.4: The optical frequency response of bolometer '9-03' biased to 0.8 Ω (black dots) and 0.5 Ω (blue asterisks). The single pole fits yield 22 ms and 13 ms time constants.

factor of ∼ 2-3, which yields a response time close to our design goals when biased at 0.5 Ω.

The decreased time constant lower into the transition is evidence that the thermalization of the TES, not the spider-web, dominates the response time of the bolometer. For bolometer arrays currently in fabrication we have reduced the heat capacity of the gold ring by a factor of four, which should decrease the response time of the TES by the same factor. The optical response time of the bolometer should then be limited by the thermalization time of the web.

6.3.4 Bolometer noise

The demodulated noise spectrum of bolometer '9-03' is shown in Fig. 6.5. The solid, red curve shows the noise level of the bolometer when it is biased with 2.275 μV_{rms} and has a resistance of 0.8 Ω. The spectrum is white down to 200 mHz with an amplitude of 5.0×10^{-17} $W/\sqrt{Hz}$. The blue, dot-dashed spectrum shows

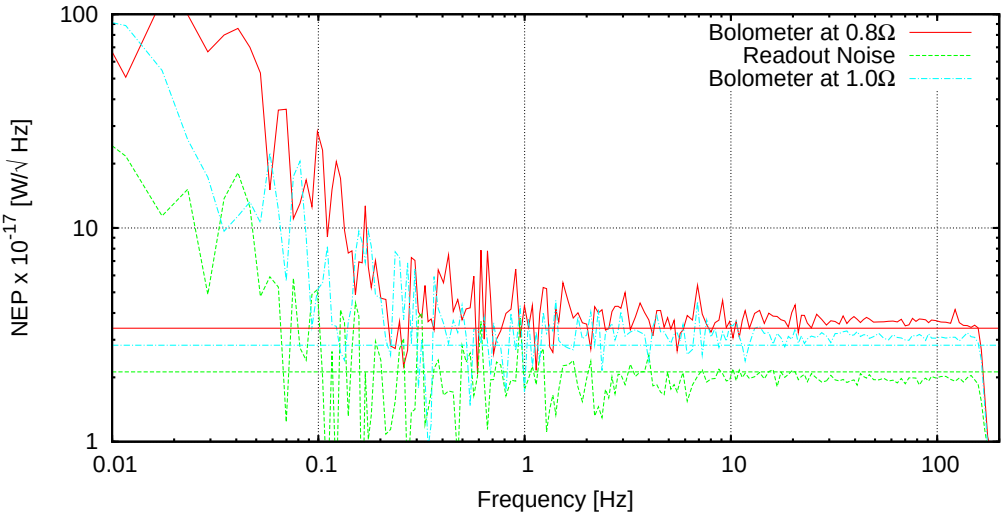

Figure 6.5: Demodulated noise of bolometer '9-03' in NEP units biased into the transition (red, solid) and above the transition (blue, dot-dash). The green, dashed curve shows the readout noise level.

the noise of the bolometer when biased above the transition at 1.0 Ω and is therefore insensitive to phonon noise. For this bias position the expected noise sources are bolometer Johnson, SQUID and readout electronics noise. The readout noise level is shown in the green, dashed curve. Readout noise consists of SQUID noise and readout electronics noise. When biased to 0.8 Ω the expected noise level is 4.2 $\times 10^{-17} W/\sqrt{Hz}$, which is calculated from the quadrature sum of readout, bolometer Johnson and phonon noise using the measured thermal conductance value. The 20% discrepancy between the calculated and measured noise levels is currently under investigation.

The expected noise sources and levels for bolometer '9-03' are listed in Tab. 6.1 in NEP units. The DfMUX demodulator transfer function is different for signal and the different noise components of the system. To account for these differences a factor of $\pi/2$ has been included for the SQUID and readout electronics noise levels, and a factor of $\sqrt{2}$ has been included for the bolometer Johnson noise (see

Appendix B.1).

Table 6.1: Noise expectation for dark bolometer '9-03.'

Noise source	Equation	NEP $(10^{-17}W/\sqrt{Hz})$
Phonon [51]	$\sqrt{\gamma 4k_bT_c^2G}$	2.3
Bolometer Johnson	$\sqrt{4k_bT_c/R}\cdot v$	1.9
SQUID	$2.5\ pA_{rms}/\sqrt{Hz}\cdot V_b$	0.9
Readout electronics	$4.7\ pA_{rms}/\sqrt{Hz}\cdot V_b$	1.7

Here $\gamma = 0.498$, k_b is Boltzmann's constant, $T_c = 550$ mK, $G = 63$ pW/K, $R = 0.8\ \Omega$ and $v = 2.275\ \mu V_{rms}$.

Post-demodulation the readout noise is increased by a factor 1.5 due to the half-wave mixer's sensitivity to odd harmonics of the demodulator frequency. A measurement of the pre-demodulated noise level shows an increase in noise at frequencies between 1 and 10 MHz. Since the square wave mixer is sensitive to odd harmonics of the fundamental it samples this excess noise, which then adds to the demodulated noise level. The quadrature sum of the mixer's response and the measured noise levels at odd harmonics of the demodulator frequency is $3.0 \times 10^{-17}W/\sqrt{Hz}$ which matches the measured value. The excess demodulated noise can be addressed without hardware changes by filtering away harmonics with a low pass filter in firmware. The source of increased out of band noise above 1 MHz is currently unknown, but we have ruled out the bolometers as the source because the same out of band noise is observed in SQUIDs that are not connected to detectors.

Bolometer Johnson, SQUID and readout electronics NEP scale linearly with the voltage bias, v. In any astrophysical application, the radiative background loads the bolometer, and the voltage bias required to keep the TES in transition is smaller than the voltage bias needed for these dark measurements. If half the power required to keep these bolometers in the transition comes from radiative

loading, the NEP from terms proportional to voltage bias summed in quadrature is 1.0 $\times 10^{-17} W/\sqrt{Hz}$ which is below the photon noise level at 150 GHz of 2.5 $\times 10^{-17} W/\sqrt{Hz}$.

6.4 Conclusion

We have fabricated and measured a TES bolometer array as part of a program to produce low thermal conductance TES bolometer arrays for the EBEX balloon-borne experiment. Average thermal conductance measurements of three bolometers on the proto-type array are in good agreement with the 32 pW/K designed value. Noise measurements are 20% larger than expected. All measurements are taken with DfMUX readout electronics, which have been designed for low power consumption suitable for a balloon application.

Chapter 7

Detector characterization of NAF bolometers

One bolometer wafer at each frequency band has been fabricated and used for the North American flight (NAF). The names of the wafers are 'G17', 'G20' and 'G18' at the 150, 250 and 410 GHz bands respectively. In this chapter, we determine the electrical and thermal properties of the bolometers on each wafer. In Sec. 7.1, we characterize the thermal transport across the bolometer weak link. In Sec. 7.2 we detail measurements that determine the TES responsivity, frequency response and linearity. In Sec. 7.3 we determine the bolometer optical time constants. For all but the final section of this chapter, the measurements were performed with the bolometers in a dark $\sim$ 270 mK enclosure in the EBEX cryostat.

7.1 Bolometer weak link thermal transport

Bolometer performance is largely dictated by the thermal transport in the weak link. The thermal conductance G and the transition temperature T_c of the bolometer determine the dynamic range and phonon noise level. We determine $G(T)$ and T_c for a large number of bolometers on each wafer by measuring the power conducted across the weak link as a function of heat-sink temperature.

7.1.1 Method

If the thermal conductivity of the weak link scales as a power law in temperature $\kappa(T) = \kappa_o T^n$, the power conducted across the link P_c is described by Eq. 3.6 reproduced here for clarity:

$$P_c = A/l\frac{\kappa_o}{n+1}(T^{n+1} - T_o^{n+1}). \tag{7.1}$$

We have also referred to P_c as the saturation power of the bolometer P_{sat}. We determine the parameters $A/l\kappa_o$, $n+1$ and T_c by performing bolometer IV curves as a function of heat-sink temperature T_o and fitting the data to Eq. 7.1 with these parameters free. For each IV curve, the power P is determined by the electrical power $P_e = IV$ dissipated in the sensor when the bolometer is held at its transition temperature T_c. The flat part of the power versus voltage (PV) graph indicates that the bolometer is held in transition at T_c (see left panel Fig. 7.1). The right panel of Fig. 7.1 shows an example of the measured power versus heat-sink temperature and the least squares fit to the data. From the fit parameters, we may determine the dynamic thermal conductance from

$$G \equiv G(T_c) = A/l\kappa_o T_c^n. \tag{7.2}$$

7.1.2 Results

Fig. 7.2 shows the distributions of n, T_c and G for each wafer determined from the fits. The mean and standard deviation of each distribution is tallied in Table 7.1.

If thermal transport is dominated by phonon surface scattering in the Silicon nitride legs, the power law index $n = 3$ [73]. We measure $n = 2.2$, 1.9 and 2.1 for each wafer, slightly less than the surface scattering limit. These values may indicate that a fraction of heat propagates in electrons for which $\kappa \sim T$.

The transition temperature of the 250 and 410 GHz wafers is $T_c \sim 510$ mK, while the 150 GHz wafer has $T_c \sim 590$ mK. These values match independent

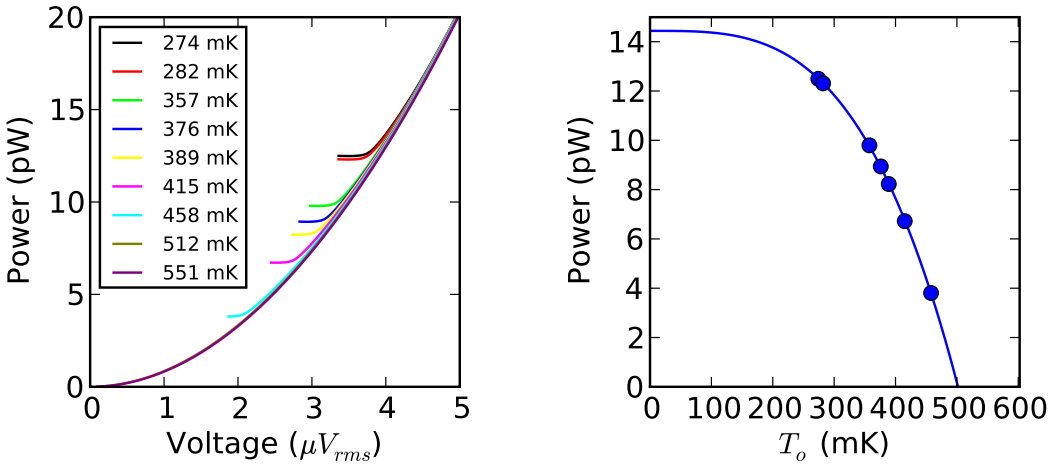

Figure 7.1: **Left:** PV curves at each heat-sink temperature T_o. The conducted power across the link from T_c to T_o is determined by the flat part of the curve. **Right:** Measurement of conducted power P_c versus T_o. The solid line is the model fit to the data.

measurements of bolometer T_cs on both the 150 and 410 GHz wafers, providing confidence in the fit and parameter extraction. Also, the 250 and 410 GHz wafers were fabricated after the first measurements of 150 GHz bolometer T_cs with the goal of lowering T_c to near 500 mK. This data set shows that we achieved this design goal.

The majority of bolometers on all wafers show $80 < G < 110$ pW/K, a factor of four to five higher than our design goal. Using these values together with T_c and operating from a 270 mK heat-sink, the expected phonon noise level is $\sim 3.5 \times 10^{-17}$ W/$\sqrt{Hz}$ for all wafers. Substantial improvements in sensitivity would result from fabricating lower thermal conductance bolometers. However, measurements of bolometer loading in the EBEX receiver, which we discuss in Sec. 8.2, show that the dynamic range provided by these higher G bolometers is currently needed.

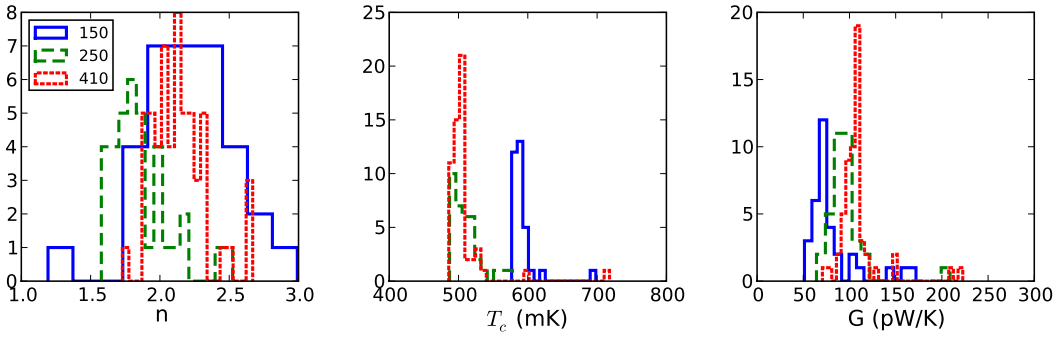

Figure 7.2: Distributions thermal transport parameters as determined from the fit for each wafer. The parameters are the thermal conductivity power law index n, transition temperature T_c and dynamic thermal conductance G.

Wafer	n	T_c (mK)	G (pW/K)	# of bolos	N_{phonon} $\times 10^{-17}$ W/$\sqrt{Hz}$
150	2.2 ± 0.3	592 ± 21	82 ± 28	33	3.6
250	1.9 ± 0.2	511 ± 21	95 ± 22	35	3.3
410	2.1 ± 0.2	508 ± 32	109 ± 24	57	3.6

Table 7.1: Mean and standard deviation of the distributions in Fig. 7.2.

7.2 Bolometer responsivity

In this section, we expand on a method described by Lueker et al. [74] to determine the frequency response of the TES. We obtain not only the frequency dependence but also the responsivity of the TES and linearity. This method applies most readily when using frequency domain multiplexing.

7.2.1 Measurement principle

The heart of a current responsivity measurement is to subject the bolometer to a known change in power. Measuring the current produced by the change in power yields the responsivity. The general idea of this method is use the beat frequency

of two AC voltages to produce the known power change. One AC voltage is the carrier voltage bias $V_c\exp(i\omega_c t)$ that biases the bolometer into the transition. The second AC voltage, called the 'test' voltage $V_t\exp(i\omega_t t)$, is used to create a fluctuating power at the beat frequency $\nu_t - \nu_c$. Below we show that with these two voltage biases, the electrical power dissipated in a sensor of resistance R fluctuates with amplitude $V_t V_c/R$.

The voltage applied to the bolometer is

$$V = V_c e^{i\omega_c t} + V_t e^{i\omega_t t}. \tag{7.3}$$

Therefore the power dissipated in the bolometer is

$$\begin{aligned} P &= \frac{1}{2}\frac{VV^*}{R} && (7.4)\\ &= \frac{1}{2R}(V_c e^{i\omega_c t} + V_t e^{i\omega_t t})(V_c e^{-i\omega_c t} + V_t e^{-i\omega_t t}) && (7.5)\\ &= \frac{V_c^2}{2R} + \frac{V_t^2}{2R} + \frac{V_c V_t}{2R}(e^{i(\omega_c-\omega_t)t} + e^{-i(\omega_c-\omega_t)t}) && (7.6)\\ &= \frac{V_c^2}{2R} + \frac{V_t^2}{2R} + \frac{V_c V_t}{R}\cos{(\omega_c - \omega_t)t}. && (7.7) \end{aligned}$$

In the last step we used the identity

$$\cos\theta = \frac{e^{i\theta} + e^{-i\theta}}{2}, \tag{7.8}$$

and thus, the electrical power dissipated in the sensor fluctuates at the beat frequency $\nu_b = \nu_c - \nu_t$ with an amplitude of $V_c V_t/R$. Note the voltages are in amplitude not rms units. The TES responds to the applied thermal signal by producing a current of magnitude determined by the responsivity. By increasing ν_b and recording the magnitude of the response, we map out the TES electro-thermal frequency response.

7.2.2 Amplitude response determination

We determine the magnitude of the current response with lock-in techniques which require explanation. The fluctuating power changes the TES resistance which then

amplitude modulates the carrier. This action transfers the thermal response to frequencies $\nu_c \pm \nu_b$ with equal power in each Fourier component. Only one of these two Fourier components contains a purely thermal response since one component must include the Ohmic response of the test signal itself, $V_t/R\exp(i\omega_t t)$. We therefore measure the component with only the thermal signal by demodulating at a frequency ν_m such that the amplitude coefficient corresponding to the thermal signal is well defined in the demodulated frequency spectrum. In practice, we apply the test signal at a beat frequency above the carrier frequency ($\nu_t = \nu_c + \nu_b$) and demodulate at frequency $\nu_m = \nu_c - \nu_b - \nu_x$ such that the thermal response appears at ν_x in the demodulated frequency spectrum.

Mathematically, the lock-in scheme works as follows. An amplitude modulated signal is $A(t)\sin(\omega_c t)$. The test signal will also vary sinusoidally, and therefore $A(t) = A_c + A_t \sin(\omega_t t)$, where A_c is the amplitude of the carrier wave, and the second term is the response from the test signal. The goal is to determine A_t. We mix the amplitude modulated signal with a sine wave $A_m \sin(\omega_m t)$. In the standard lock-in technique $\omega_m = \omega_c$; however, in order to isolate the thermal signal, the mixer frequency differs from the carrier. Prior to the demodulator filter, the harmonic content of the signal is the product of the amplitude modulated signal and the mixer:

$$
\begin{aligned}
& A_m \sin\omega_m t A(t) \sin\omega_c t && (7.9)\\
= \;& A_m \sin\omega_m t (A_c + A_t \sin\omega_t t)\sin\omega_c t && (7.10)\\
= \;& \frac{A_m A_c}{2}\{\cos(\omega_c - \omega_m)t + \cos(\omega_c + \omega_m)t\} + && (7.11)\\
& \frac{A_m A_t}{4}\{\sin[(\omega_c - \omega_m) + \omega_t]t - \sin[(\omega_c - \omega_m) - \omega_t]t && (7.12)\\
& + \sin[(\omega_c + \omega_m) + \omega_t]t - \sin[(\omega_c + \omega_m) - \omega_t]t\} && (7.13)\\
& && (7.14)
\end{aligned}
$$

The mixer places the amplitude modulated signal in the side-bands of $(\nu_c \pm \nu_m)$. The demodulator filter attenuates the additive terms leaving the amplitude modulated signal in side bands of $\nu_c - \nu_m$. The Fourier component at $\nu_c - \nu_m - \nu_t$ has

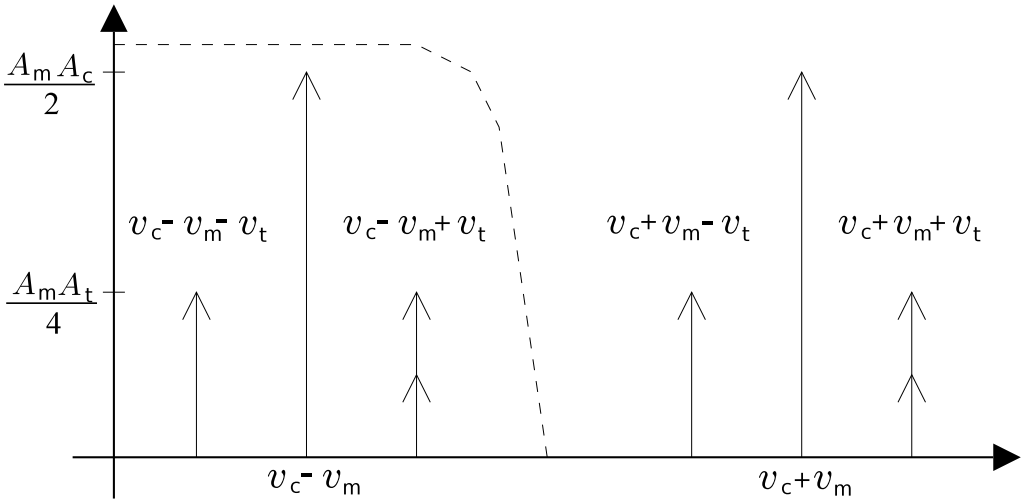

Figure 7.3: Cartoon demonstrating the determination of the amplitude response to an electrical fluctuating power for a TES responsivity measurement. The cartoon shows the harmonic content of the demodulated TES response. The demodulator filter band pass shown by the dashed line attenuates the high frequencies. The thermal response signal A_t is determined by measuring the Fourier component at frequency $\nu_c - \nu_m - \nu_t$. Signals at $\nu_c \pm \nu_m + \nu_t$ include the Ohmic response of the applied test signal as well as the thermal signal indicated schematically by two vectors.

an amplitude $A_m A_t/4$, and by measuring this component, we determine A_t. Fig. 7.3 illustrates this demodulation concept.

7.2.3 Data reduction

We applied beat frequencies at 3,9,27,and 81 Hz. For each frequency, we record ~ 5 seconds of data demodulated at a frequency such that the thermal response lies at 24 Hz in the demodulated spectrum. From this time-stream, we apply a Hanning window and then compute the power spectral density (PSD), which has units $cnts_{peak}/\sqrt{Hz}$, in which *cnt* is a single demodulated ADC count. An example PSD from an applied thermal signal at 9 Hz is shown in Fig. 7.4.

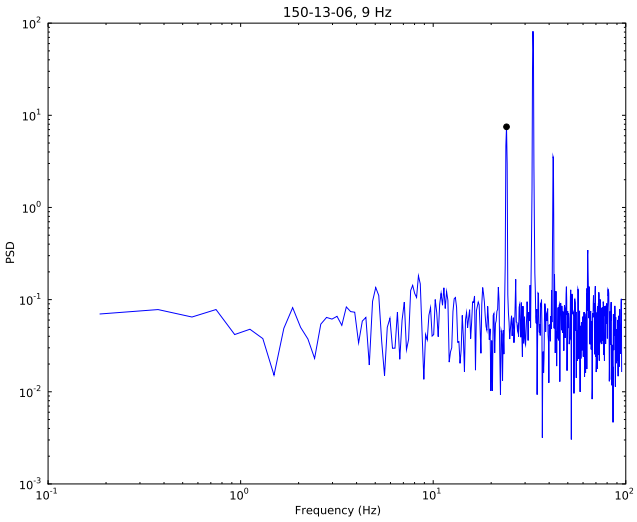

Figure 7.4: Demodulated TES power spectrum during a 9 Hz beat frequency thermal signal. The thermal response, carrier frequency and test frequency lie at 24, 31 and 40 Hz respectively. The 40 Hz signal contains the Ohmic response to the applied test signal and one fourth the power from the thermal response. We measure the peak at 24 Hz to determine the amplitude response to applied fluctuating power.

The amplitude of the response (A_t) to the fluctuating power can be calculated from

$$A_t = \frac{dA}{d(cnt)} \alpha_{Hanning} \frac{4PSD(\nu_x)\sqrt{\Delta\nu}}{A_m}. \tag{7.15}$$

The constant $\frac{dA}{d(cnt)}$ converts the demodulated counts to current at the squid coil (see Appendix B.2), $\alpha_{Hanning}$=2 corrects for the power removed by the Hanning window, $PSD(\nu_x)$ is the Fourier component at the thermal response frequency, $\Delta\nu$ is the frequency bin resolution and A_m is the amplitude of the mixer. Note that in practice $\frac{dA}{d(cnt)}$ is determined from a calibration that includes the factor

$A_m/2$. Therefore in practice A_t is determined by

$$A_t = 2\frac{dA}{d(cnt)}\alpha_{Hanning} PSD(\nu_x)\sqrt{\Delta\nu}. \tag{7.16}$$

The responsivity is then determined by

$$S_I = \frac{A_t}{P} = \frac{A_t}{V_c V_t/R}, \tag{7.17}$$

where R is determined from the bolometer IV curve ($R = V_c/I$) and V_c and V_t are determined from the DfMUX settings and knowledge of the network. Typical values are $V_c = 4.2\ \mu V_{peak}$, $V_t = 6.8\ nV_{peak}$ and $R = 0.7\ \Omega$.

7.2.4 Results

Linearity

By increasing the amplitude of the test signal, we increase the amplitude of the fluctuating power and probe the bolometer linearity. The left panel of Fig. 7.5 shows the bolometer response at 3 Hz to increasing test signals for three different bias positions. When biased to 70% into the transition, the bolometer is linear up to 3 pW and deviates from linearity by 4% at 3.5 pW.

Responsivity

The right panel of Fig. 7.5 shows the responsivity versus frequency for the same bias positions 0.9, 0.8 and $0.7R_n$. The top plot shows that the responsivity increases deeper into the transition. The bottom plot shows the same data normalized to the value at 3 Hz in order to show how the frequency response differs for the three bias positions. The lower attenuation of the signal at the $0.7R_n$ bias position relative to the other bias positions demonstrates that the bolometer speeds up when biased lower in transition as predicted in Eq. 3.20. At $0.7R_n$, $\nu_{-3dB} \sim 80$ Hz. Other devices show similar results.

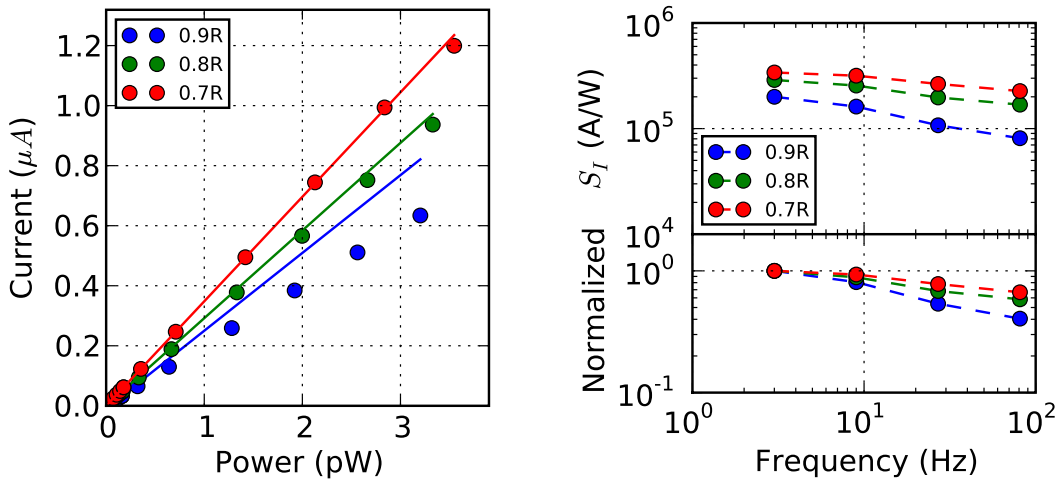

Figure 7.5: **Left:** TES current response versus applied power for 0.9, 0.8 and $0.7R_n$ bias positions. The non-linearity of the device is shown by the deviation of the data points from the solid lines. Linearity improves deeper into the transition. **Right:** TES responsivity versus frequency. The top panel shows that the responsivity increase when biasing lower in the transition. The bottom panel is normalized to the value at 3 Hz in order to show how the sensor frequency response changes with bias position.

Comparison of measured responsivity to $1/v$

From Sec. 3.2.2, Eq. 3.19 predicts that $|S_I| = |1/v|$ for a bolometer with high loop gain. We expect that the bolometer has high loopgain when biased low in transition and therefore compare the measured responsivity to $1/v$. We find that the measured responsivity is higher than predicted for all three wafers. Fig. 7.6 shows the distributions of the product $S_I v$, the measured responsivity at $0.7R_n$ and the RMS voltage bias. This product is the measured to expected responsivity ratio and is free of factors which convert the raw signal to physical units. The distributions are centered on 2, 1.2 and 1.7 for the 150, 250 and 410 GHz wafers indicating a larger responsivity than $1/v$.

This result is difficult to understand since $1/v$ is the theoretical upper-limit to

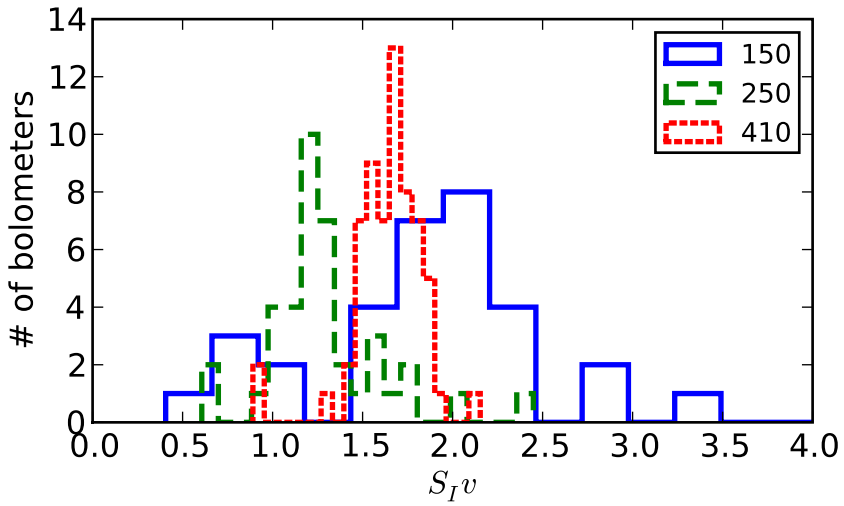

Figure 7.6: Distributions of the measured to expected responsivity ($S_I v$) for each bolometer wafer. All show a responsivity higher than expected.

the responsivity. However, current bolometer noise measurements (not discussed here) follow the same general trend. 150 and 410 GHz bolometers show noise levels $\sim \times 2$ higher than expected while 250 GHz bolometers show noise $\sim 20\%$ higher than predicted. Such measurements are explainable if the responsivity is higher than we think. The responsivity data set shows no dependence on AC bias frequency, and the resistance determined from IV curves match the resistance determined from the network analyses at the $\sim 10\%$ level. These two points show that the data is free from these potential sources of systematic error. Our current hypothesis is that the actual voltage bias across the bolometer is lower than we calculate due to resistive strays in series with the bolometer. One piece of evidence that supports this model is that for all bolometers the ratio $S_I(0.7R_n)/S_I(0.8R_n)$ is larger than $v(0.8R_n)/v(0.7R_n)$ calculated assuming no strays. Including stray resistance, the calculated value $v(0.8R_n)/v(0.7R_n)$ would increase.

7.3 Bolometer time constants

The bolometer optical time constant τ_o is the thermal relaxation time of the spider-web absorber to the heat-sink as discussed in Sec. 3.3. The optical time constant determines the telescope mapping speed, and for EBEX, the HWP rotation speed. We determine τ_o by mapping the bolometer response to a beam-filling chopped thermal source. We fit the data to a single pole frequency response to extract τ_o:

$$R(\omega) = \frac{A}{\sqrt{1 + (\omega\tau_o)^2}}. \tag{7.18}$$

Polsgrove [67] states that the mean optical time constants are 34.2, 35.0 and 45 ms at 150, 250 and 410 GHz for a large sample of detectors. However, the size of the thermal chop was very large for this data set ($\sim$ 10 pW absorbed at 410 GHz). Since the TES is not in the small signal limit, the frequency response described by Eq. 3.20 does not apply. In which case, we expect that the time constant of the TES and not the web dominates the thermal response time. In this light, the Polsgrove values are a useful upper-limit to τ_o.

Data while using a smaller chopped load exists for a subset of the array. From this data set, τ_o = 34.8 $\pm$ 14.7, 12.9 $\pm$ 2.5 and 8.2 $\pm$ 1.0 ms at 150, 250 and 410 GHz for 5, 4 and 8 bolometers respectively. At 250 and 410 GHz the time constants are a factor of three to four smaller than the previously measured values. The 150 GHz bolometers still show long time constants because again the size of the input signal was too large. Like the Polsgrove measurements, this data set was also collected during the NAF campaign, for which the 150 GHz bolometers had no neutral density filter (NDF) to attenuate the signal (see Chapter 8). This is the source of the discrepancy in τ_o between the 150 GHz array and the higher frequency arrays.

In the March 2009 cryostat run at University of Minnesota, a 4 K NDF was used to attenuate 99% of the optical load. The NDF prevents bolometer saturation for ground-based measurements. Measurements of τ_o in this configuration are in the small signal limit and four 150 GHz bolometers show τ_o=9.4, 13.2, 11.4 and

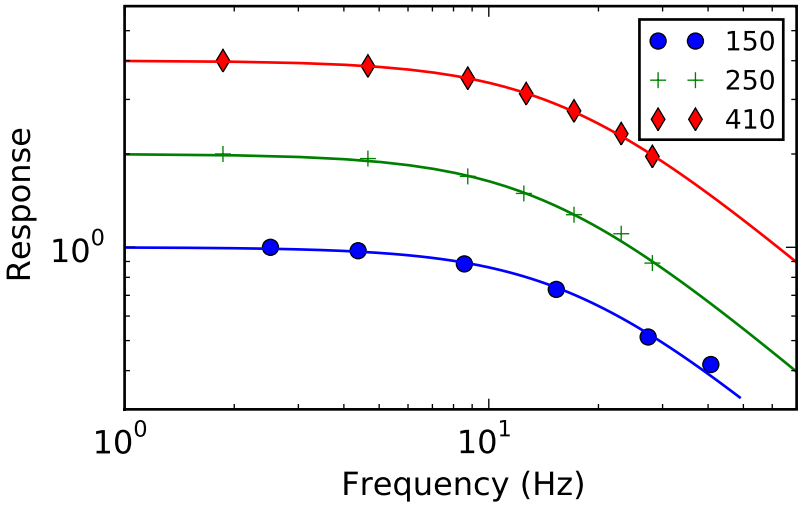

Figure 7.7: The solid lines show example τ_o fits for a single bolometer on each wafer used in the NAF. The offsets are arbitrary. From the fits $\tau_o = 9.4$, 11.2 and 9.9 ms at 150, 250 and 410 GHz.

14.7 ms. Unfortunately, the entire array was not measured; however, these four data points indicate that the 150 GHz bolometer time constants are a factor of three smaller than previously thought.

Taken together, these three data sets show that $\tau_o \sim 10$ ms for all wafers. Fig. 7.7 shows example fits for a bolometer on each wafer.

Chapter 8

North American Flight

The bolometer wafers detailed in Chapter 7 were integrated into the EBEX instrument and used in the NAF. The NAF focal plane of live bolometers is shown in Fig. 8.1. The focal plane had 167 light, 22 dark and 13 eccosorb-horn filled bolometers distributed among the three frequency bands (see Appendix A for details). Dark bolometers are used for systematic checks, and the eccosorb filled-horns attenuate $\sim 99\%$ the load for ground-based calibration measurements during the field campaign. In this chapter, we discuss the receiver optical efficiency and bolometer loading during the NAF.

8.1 Receiver optical calculations

Fig. 8.2 shows a cross-section schematic of the EBEX receiver optics which include IR-blocking filters, lenses, the HWP, polarizing grid, horn arrays and bolometers. Each component reflects and absorbs part of the incoming wave, which decreases the sensitivity to external radiation. The emissive components are a source of bolometer loading. In this section, we calculate the receiver optics efficiency ϵ_o and the bolometer loading due to thermal emission of the optical elements. We define the receiver optics as all the elements in the receiver up until the horn arrays and bolometers. We separate the receiver optics from the bolometers in

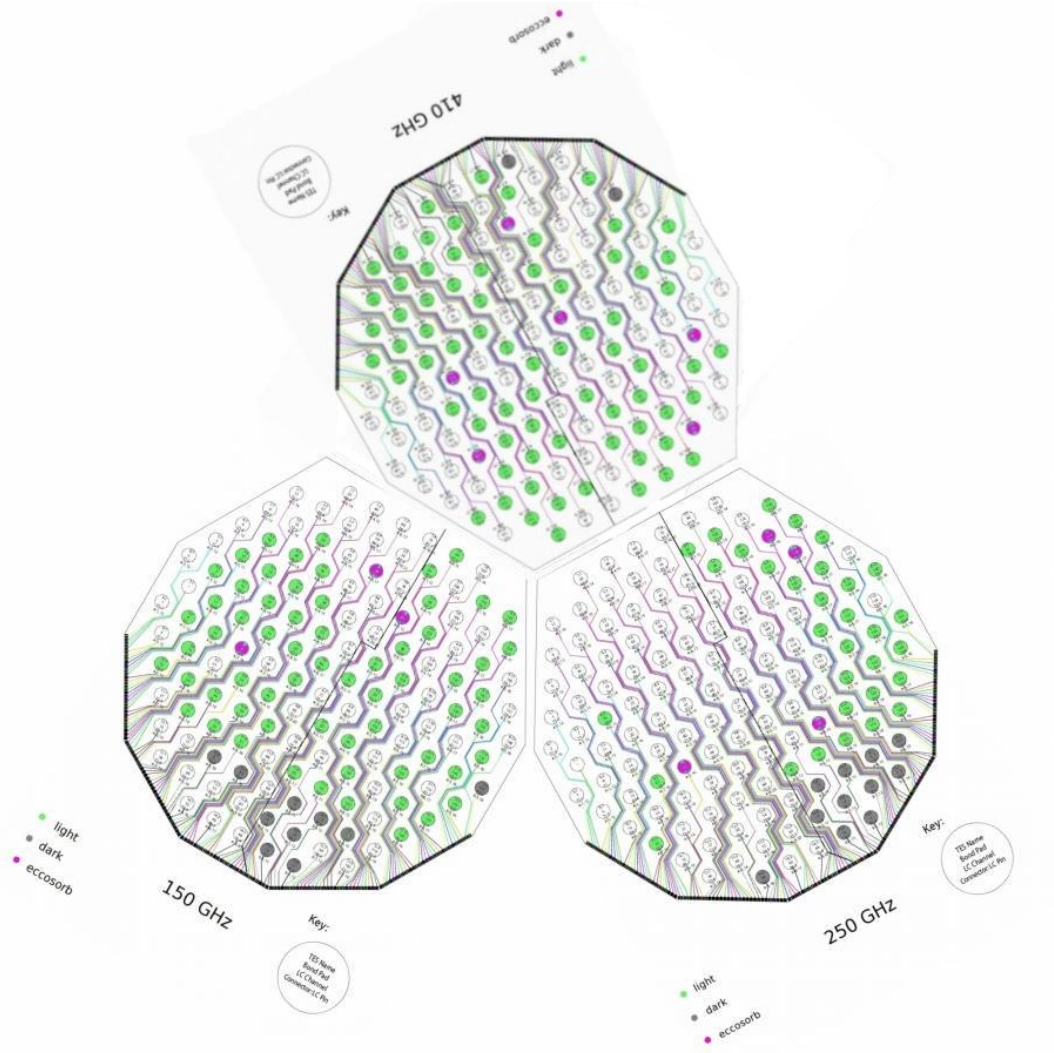

Figure 8.1: North American flight focal plane configuration.

both these calculations because the bolometer absorption efficiency ϵ_b is unknown. Table 2.1 lists the band edges and throughput assumed for the calculations.

8.1.1 Receiver optics efficiency

The optics efficiency ϵ_o is defined as the fraction of external power that enters the receiver window in a detector beam-width which remains at the horn array. To calculate ϵ_o, we consider each optical component independently, multiply each elements transmission frequency response $\tau(\nu)d\nu$ and then integrate the combined response across the band,

$$\epsilon_o = \frac{\int_{\nu_1}^{\nu_2} \prod_{i=1}^{N} \tau(\nu)_i \, d\nu}{\nu_2 - \nu_1}. \tag{8.1}$$

We use measurements of the transmission spectra [1] for low pass filters (LPE, LPE2, LPE2b and band pass filters LP3 and LP4). For all other optical elements, the absorption and reflection is calculated using knowledge of the index of refraction, loss tangent and thickness of the material at the appropriate temperature and frequency range (see Table 8.1). We calculate loss due to absorption and reflection separately. When calculating reflective loss, we include multiple reflections for all elements that have uniform thickness and are normal to the direction of wave propagation. For all lenses, we assume 4% loss per surface based on the index of refraction for ultra high molecular weight polyethylene (UHMWPE).

The calculated transmission spectrum of the receiver optics in each frequency band is shown in the left panel of Fig. 8.3. We calculate ϵ_o = 13.0, 4.0 and 3.9 % for the 150, 250 and 410 GHz respectively. Because we neglect interaction between surfaces and given the uncertainty in the optical parameters used in the calculation, we expect a factor of ~ 2 uncertainty in the calculated ϵ_o.

Table 8.2 lists the transmission through each optical component in the receiver. The non-anti-reflection coated HWP is the largest contributor to reflective loss other than the polarizing grid (see Fig. 8.3 right panel). The largest absorptive

[1] measurements from Cardiff University using Fourier transform spectroscopy

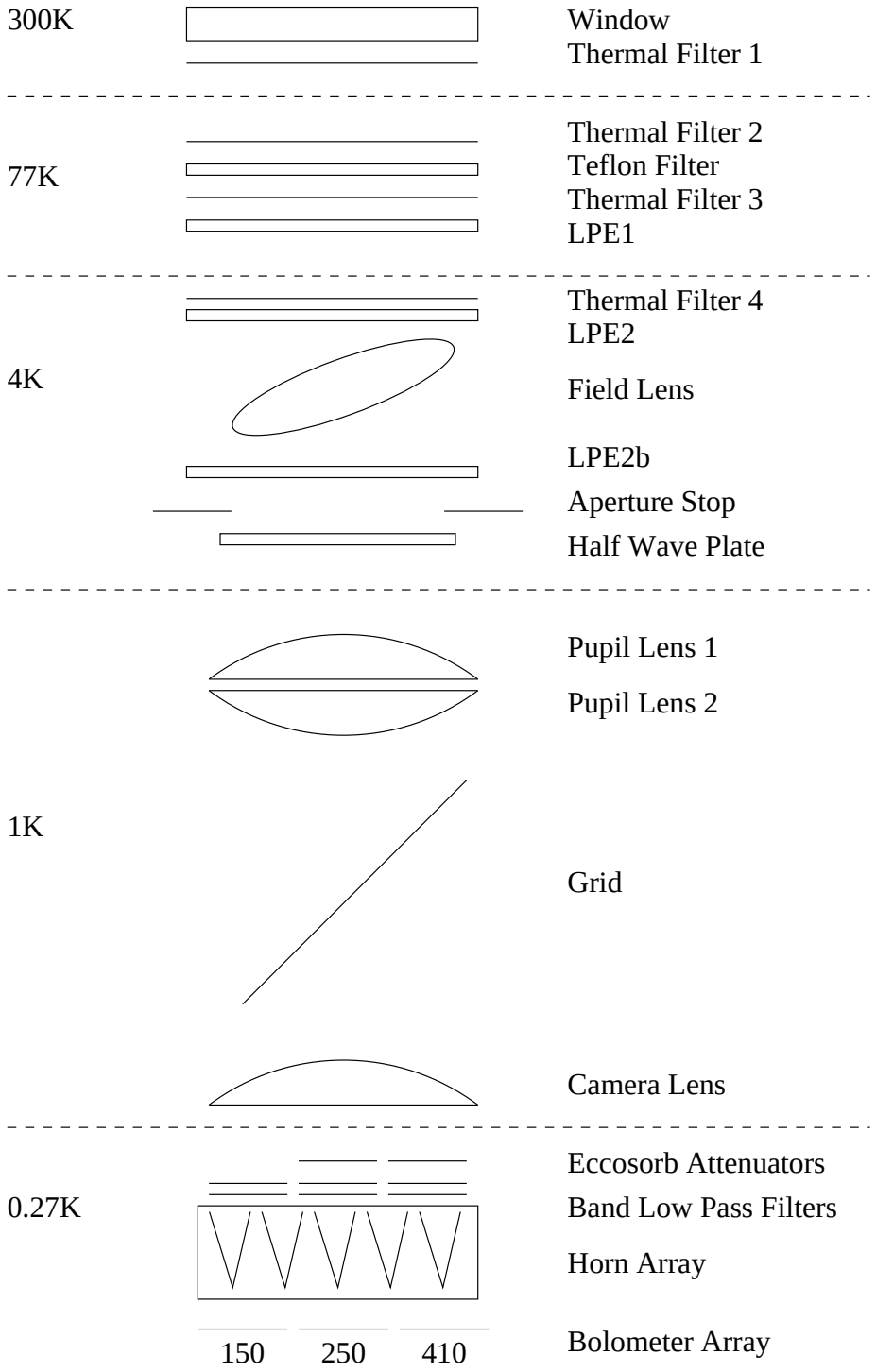

Figure 8.2: Cross-section schematic of the receiver optical elements in the NAF configuration.

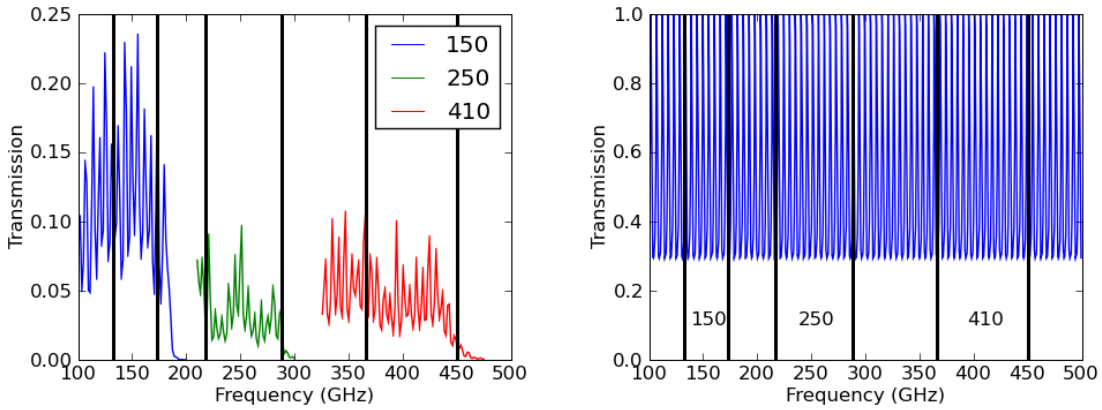

Figure 8.3: **Left:** Calculated EBEX receiver optics transmission in each frequency band. Fringing at 5 GHz is due to the non-AR coated HWP. **Right:** Calculated transmission of the non-AR coated HWP modeled as an 8.25 mm thick slab of sapphire with index $n = 3$. Fringing occurs due to reflections off the front and back surfaces.

losses are due to the window and the 77K teflon filter, which each absorb $\sim 10\%$ at 410 GHz.

Eccosorb MF-110 neutral density filters (NDFs) were placed in front of the 250 and 410 GHz horn arrays to avoid detector saturation. The thickness of each NDF was 1.08 mm. Two NDFs were placed in series at 250 GHz. The transmission is calculated assuming loss tangent measurements in [77] for which lab measurements at 300 K of the NDFs are in good agreement. The NDFs explain the factor of three decrease in calculated transmission at 250 and 410 GHz relative to 150 GHz.

8.1.2 Loading

Thermal emission from receiver optical elements load the bolometers and consume a fraction of the detector dynamic range. We estimate this emissive power loading

element	material	T(K)	n	d (cm)	tanδ $\times 10^{-4}$	ref.
window	UHMWPE	300	1.52	1.27	1.3-2.8	[75]
teflon filter	PTFE	200	1.44	1.27	5.5-7.0	[75]
LPEs	PP	20-160	1.5	0.5	5.5-7.0	[75, 76]
lenses	UHMWPE	2-20	1.52	4.0-6.0	3.1	[75]
HWP	sapphire	3.0	50	0.825	0	[75]
NDF	eccosorb MF-110	1.9	.27	1.09	380	[77]

Table 8.1: Optical properties of receiver elements. The spread in a parameter value indicates the range over 100-450 GHz, or the range from different optical elements if the entry includes more than one element.

P_{emit} in each frequency band using the following equation

$$P_{emit} = \sum_{i=1}^{N} A\Omega \int_{\nu_1}^{\nu_2} I(\nu, T)_i \epsilon(\nu)_i \tau(\nu)_i \, d\nu. \tag{8.2}$$

Here, i is the i^{th} optical element, $I(\nu, T)$ is the intensity emission spectrum, $\epsilon(\nu)$ is the emissivity, $\tau(\nu)$ is the transmission of the receiver *downstream* from the i^{th} element and $A\Omega = \lambda^2$ is the throughput defined by a single moded conical feed. We assume the Planck function for $I(\nu, T)$, and the temperature is taken from measurements in a previous cryostat run in which sensors were mounted on the center of each optical element. The emissivity is determined from the calculated absorption spectrum.

Table 8.3 tallies the thermal emission from each element. With the transmission spectra calculated using the method described in Sec. 8.1.1, we estimate that the emissive power entering the horn array is 2, 2.3 and 5.1 pW at 150, 250 and 410 GHz subject to the factor two uncertainty in ϵ_o. To determine the power absorbed in the bolometers, these numbers are multiplied by the bolometer absorption efficiency.

element	150 GHz	250 GHz	410 GHz
Window	0.91	0.91	0.88
Teflon Filter	0.92	0.89	0.86
LPE1	0.99	0.95	0.98
LPE2	0.95	0.96	0.98
Field Lens	0.92	0.91	0.89
LPE2b	0.98	0.99	0.90
HWP	0.54	0.53	0.52
Pupil Lens 1	0.92	0.91	0.90
Pupil Lens 2	0.92	0.91	0.90
Grid	0.5	0.5	0.5
Camera Lens	0.91	0.90	0.88
Eccosorb Attenuator	1.0	0.35	0.42
LP3	0.96	0.97	0.95
LP4	0.96	0.90	0.91
total	0.13	.04	0.039

Table 8.2: Calculated receiver optics transmission (receiver optics efficiency ϵ_o) for each element.

8.2 Bolometer loading measurements

As detailed in Sec. 3.4 knowledge of bolometer loading allows one to optimize the bolometer sensitivity. In this section, we determine the bolometer loading during the North American Flight.

8.2.1 Method

When the bolometer is open to light, there are two sources of input power: electrical power P_e and optical power P_o, which we wish to determine. Conservation of energy requires

$$P_o = P_c(T_o) - P_e(T_o), \tag{8.3}$$

where $P_c(T_o)$ is the power conducted across the link from the bolometer transition temperature T_c to the heat-sink temperature T_o. P_e is the electrical power required

element	T (K)	150 GHz	250 GHz	410 GHz
Window	300	2.3	11.4	30.1
Teflon Filter	200	4.7	19.1	36.4
LPE1	160	2.5	6.8	15.3
LPE2	100	1.5	4.1	9.2
Field Lens	20	0.1	0.4	1.0
LPE2b	20	0.3	0.6	1.2
HWP	50	0.4	1.6	3.8
Pupil Lens 1	2	~ 0	~ 0	~ 0
Pupil Lens 2	2	~ 0	~ 0	~ 0
Camera Lens	2	~ 0	~ 0	~ 0

Table 8.3: Calculation of the in-band power (in pWs) emitted from each optical element.

to hold the bolometer in transition at heat-sink temperature T_o and with the optical load P_o. $P_c(T_o)$ is well characterized from dark measurements described in Sec. 7.1. As such, a bolometer load curve determines P_o since P_e is measured from the flat part of the PV graph.

We determined the optical load at each frequency band for two configurations. In the first configuration, the receiver window is covered with an aluminum lens cap. The second configuration is during the EBEX NAF. In flight, the focal plane temperature cooled from 300 to 270 mK during bolometer tuning. As such each bolometer was tuned at a slightly different heat-sink temperature, and for this reason we include the heat-sink temperature dependence in Eq. 8.3.

8.2.2 Results

Fig. 8.4 shows the distribution of optical power absorbed in the bolometers for both the receiver and in-flight load configurations. Table 8.4 lists the mean and standard deviation of the distributions in both cryostat configurations.

The 150 GHz loading is a factor ~ 3 larger than the other bands due to the use of neutral density filters (NDFs) at the higher frequency bands. Considering

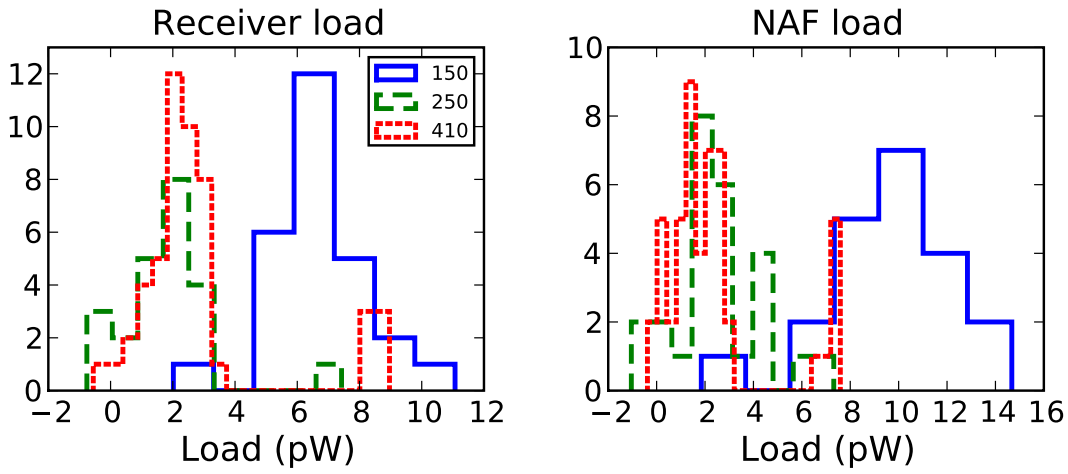

Figure 8.4: Distribution of the measured receiver loading (left) and in-flight loading (right) for each of the three frequency bands. The 250 and 410 GHz frequency bands have lower load because of the neutral density filters placed in front of the horn arrays.

the $\sim$ 30% and 40% transmission of the NDFs at 250 and 410 GHz, the loading at each frequency band is very similar.

The distributions show considerable scatter. We expect a $\sim$ 20% smear due to the frequency dependent voltage bias and current readout that have not been corrected as discussed in Sec. 5.5. In addition, for bolometers with large transition widths δ, a $\sim$ 1 pW error in determining P_e may result from the non-flat PV response in the transition. These two effects explain the majority of the variance in distribution. We expect variability in bolometer absorption efficiency to be sub-dominant. We delay the discussion of these results to after the description of optical efficiency measurements since these measurements influence the loading prediction.

Wafer	Flight load (pW)	Receiver load (pW)
150	9.7 ± 2.7	6.7 ± 1.6
250	2.6 ± 1.8	1.8 ± 1.6
410	2.3 ± 2.1	2.9 ± 2.2

Table 8.4: Mean and standard deviation of the bolometer loading distributions in Fig. 8.4.

8.3 Receiver optical efficiency measurements

We determine the end-to-end receiver optical efficiency ϵ_r using two independent methods. In the first method described, we set limits on the efficiency using the load curves measured with a 273 K thermal background. In the second method, we record the bolometer response to a known, chopped thermal load between ice water and room temperature. In both methods, we define the efficiency as the fraction of input power P_{in} at the receiver window in a detector beam that is absorbed in the bolometer P

$$\epsilon_r = P/P_{in}. \tag{8.4}$$

8.3.1 Calculation of input power

The power entering the receiver window in a detector beam size is

$$P_{in} = xA\Omega \int_{\nu_1}^{\nu_2} I(\nu, T)\, d\nu, \tag{8.5}$$

where x is the fraction of the Gaussian beam that is not clipped by the Lyot stop, $A\Omega = \lambda^2$ is the throughput defined by a single moded conical feed and $I(\nu, T)$ is the intensity spectrum.

8.3.2 Limits from load curves

Limits on ϵ_r can be obtained from the steady state power absorbed in the bolometer given an external thermal load. If the bolometer is observed to be saturated, at least the power required to drive the TES above its transition is absorbed in the bolometer. Dividing the saturation power of the bolometer P_{sat} by the calculated input power yields a lower limit on ϵ_r.

One caveat to this method is that the argument assumes no emissive loading. Considering emission, the optical efficiency is determined from

$$\epsilon_r = \frac{P - P_{emit}}{P_{in}}, \tag{8.6}$$

where P is the total power absorbed in the bolometer, P_{emit} is the power absorbed in the bolometer due internal emissive elements and P_{in} is the external input power. If the bolometer is saturated, P may be replaced by the saturation power of the bolometer P_{sat} in Eq. 8.6 and

$$\epsilon_r > \frac{P_{sat} - P_{emit}}{P_{in}}. \tag{8.7}$$

We use the measured receiver load from Sec. 8.2 as an estimate of P_{emit} which produces a lower limit on ϵ_r.

We observe all but three 150 GHz bolometers are saturated, all but a single 250 GHz bolometer is saturated and ~ 9.8 pW of power are absorbed in 410 GHz bolometers when the receiver observes at 273 K load. Those bolometers at 150 and 250 GHz bolometers that do not saturate have higher P_{sat}s than the wafer mean and thus have the dynamic range to observe higher loads. These observations show that the end-to-end receiver optical efficiency ϵ_r is > 6.2, > 2.9 and $\sim 1.6\%$ for the 150, 250 and 410 GHz band respectively. The details are given in Table 8.5.

8.3.3 Measurements from chopped thermal load

We determine ϵ_r explicitly by recording the bolometer response to an ice water to room temperature chopped thermal load.

ν GHz	P_{in} (273K) pW	P pW	P_{emit}	ϵ_r limit
150	297	>15	6.7	>2.8 %
250	523	>12	1.8	>2.0 %
410	610	10	2.9	1.2 %

Table 8.5: Limits on ϵ_r from power absorbed with a 273 K load. The value of P_{sat} is the average value for the wafer.

Experimental description

We use egg crate eccosorb CV3 as a beam filling, black body source. One piece of eccosorb is held in an ice water bath in an expanded polystyrene container suspended $\sim$ 6" above the cryostat window. The bottom of the container is $\sim$ 1.5" thick and is expected to absorb 10% at 410 GHz while negligible in the other bands. An identical piece of eccosorb at room temperature is periodically placed on the cryostat window to provide a changing load from 273 K to 298 K. The change in input power is calculated using Eq. 8.5 assuming the Planck distribution, $T_1 = 298$ K and $T_2 = 273$ K and a top hat frequency response. Tab. 8.6 tallies the input power for each frequency band. We include 10% loss due to the polystyrene cooler at the 410 GHz band.

ν_{center} GHz	ν_1 GHz	ν_2 GHz	x	ΔP_{in} pW
150	133	173	0.81	23.5
250	217	288	0.99	50.0
410	366	450	1	58

Table 8.6: Calculated input power from an ice water to room temperature chopped load for each EBEX frequency band.

For each thermal load, we average 100 bolometer samples ($\sim$ 0.5 s) and subtract the averages at each thermal load to determine the bolometer response to

chopped power. The change in absorbed power in the bolometer is determined by

$$\Delta P = \Delta cnt \times \frac{\frac{dA}{d(cnt)}}{S_I} \tag{8.8}$$

where Δcnt is the recorded change in demodulator counts, $\frac{dA}{d(cnt)}$ is a factor converting demodulator counts to current at the SQUID input coil (see Appendix B.2) and $S_I = dI/dP$ is the responsivity of the bolometer for which we assume $S_I = 1/v$. The measured end-to-end receiver optical efficiency is determined by

$$\epsilon_r = \frac{\Delta P}{\Delta P_{in}}. \tag{8.9}$$

At each thermal load, we flash focal plane LEDs to check for responsivity variations between the thermal loads.

Bolometer cuts

Bolometers with no distinct turnaround in the IV curve are rejected from the analysis. This is the only cut to the data we apply for the results below. We analyzed bolometers from a more stringent bolometer cut, and the results are largely unchanged. In addition to the IV cuts, the stringent cut rejected bolometers with responsivity variation greater than 10% at the two thermal loads and bolometers with an LED flash response of $S/N < 10$. Two notable difference between the initial cut and stringent cut are that ϵ_r is 15% greater at 410 GHz for the more stringent cut, and no 150 GHz light bolometers pass the stringent data cut.

Results

Fig. 8.5 shows the distribution of measured ϵ_r for each bolometer type in each frequency band. Table 8.7 lists the weighted mean and standard deviation of the distribution. The mean value is weighted by the variance of the 100 samples taken at each thermal load for each bolometer. The average optical efficiency for light bolometers is 15.0, 1.8 and 0.58% respectively for 3,1 and 58 bolometers at 150, 250 and 410 GHz.

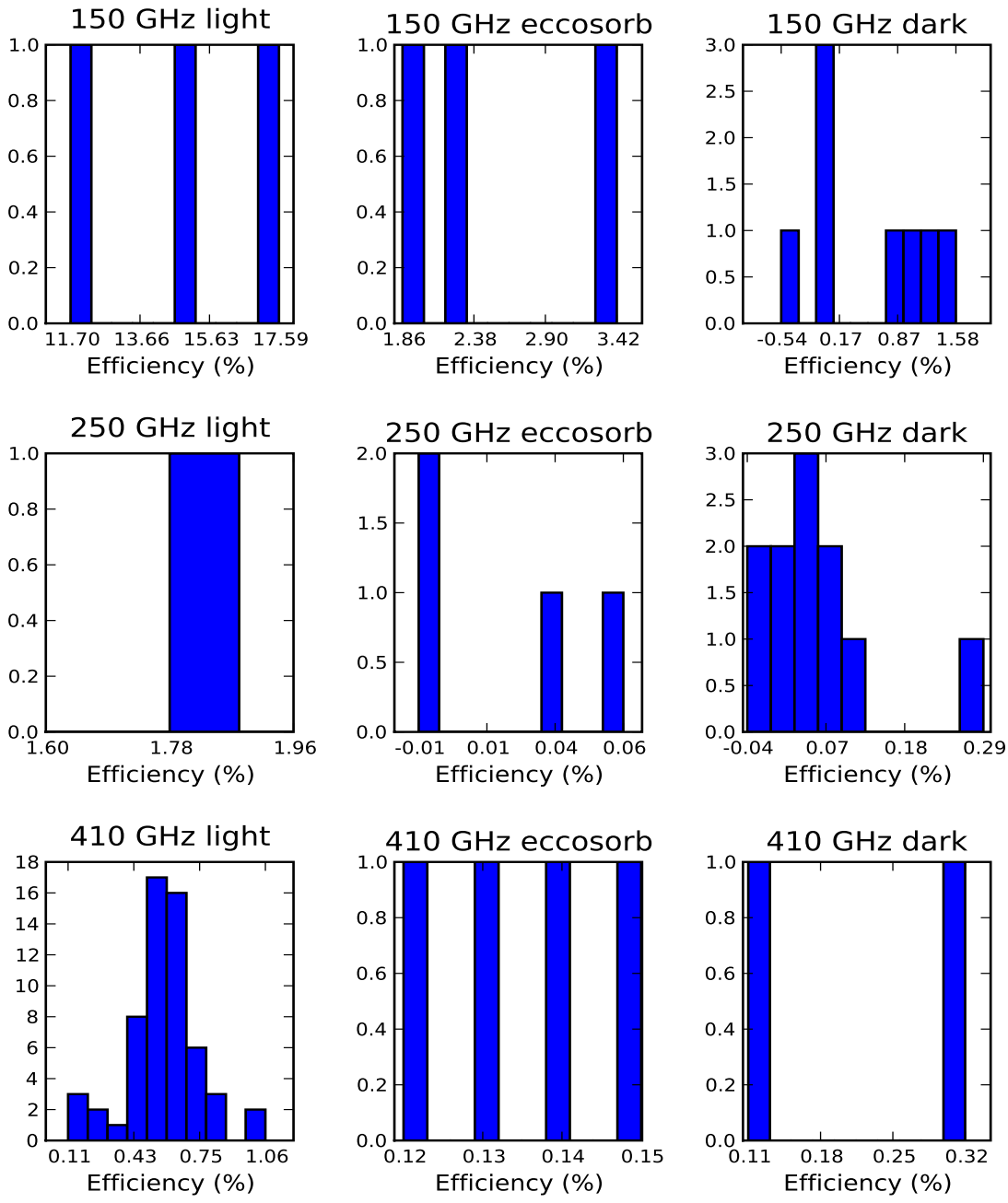

Figure 8.5: EBEX NAF optical efficiency histograms determined from a chopped thermal load.

ν	type	ϵ_r (%)	# of bolos
150	light	15.5 ± 2.4	3
	eccosorb	2.9 ± 0.7	3
	dark	0.94 ± 0.71	8
250	light	1.8	1
	eccosorb	0.02 ± 0.03	4
	dark	0.03 ± 0.1	11
410	light	0.58 ± 0.18	58
	eccosorb	0.13 ± 0.01	4
	dark	0.12 ± 0.22	2

Table 8.7: Weighted mean and standard deviation of the distribution of the measured optical efficiency ϵ_r for bolometers in a given frequency band and type.

8.3.4 Discussion

We find the end-to-end receiver efficiency is 15.5, 1.8 and .58% at 150, 250 and 410 GHz determined by the thermal chop method. The low efficiency is in large part caused by reflection from the non-AR coated HWP and lenses. The increased attenuation at the higher frequency bands is due to the focal plane NDFs and the higher absorption at these frequencies. We point out that using our definition of efficiency, the highest attainable efficiency is 50% due to the reflection from the grid. Also, the shape of the filter response is considered an inefficiency, we assumed a top hat response to calculate the input power.

The two independent methods give consistent results at 150 and 250 GHz, whereas the loading method yields a factor of two higher efficiency then the chop method at 410 GHz. One plausible explanation is that we under-estimated the absorption of the polystyrene cooler which held the ice water eccosorb. No data exists for the attenuation of expanded polystyrene above 250 GHz. To estimate the attenuation, we perform a linear extrapolation and determine the loss is 10%; however, the data hints at a sharper increase of attenuation above 300 GHz [78]. Increased attenuation will decrease ΔP_{in} and increase ϵ_r by the same factor. In

future optical efficiency measurements, this attenuation can easily be calibrated by placing an additional slab of polystyrene in front of the receiver window while observing a load colder than room temperature and measuring the bolometer response.

Within a bolometer class, the distribution has substantial spread. For example, the 410 GHz light bolometer distribution resembles a Gaussian distribution but with a full width at half maximum (FWHM) 30% of the mean value. The random error on an individual measurement is low (0.03% in percent efficiency units), but we expect a few sources of systematic error that smear out the distribution. The hypothesized largest contributor to the spread is due to the approximation that the responsivity $S_I = 1/v$. This factor is used to convert the bolometer response to power units. However, the measurements reported in Sec. 7.2.4 show that at 410 GHz the distribution of the measured to expected responsivity has a FWHM at the 25% level.

Dark and eccosorb bolometers

The optical efficiency measured in the dark and eccosorb 250 GHz bolometers is consistent with zero within the noise of the measurement. This is as expected; however, this is not the case for the 150 and 410 GHz wafers. The 150 GHz dark bolometers have a bi-modal distribution. Four bolometer are consistent with zero signal while four show $\sim 1\%$ optical efficiency. This suggests our method of making dark detectors can work but is unreliable. We make the bolometer dark by placing Al tape over the exit aperture of the waveguide. Perhaps light leaks exist in half the dark detectors. The 150 GHz eccosorb bolometers as well as both the 410 GHz eccosorb and dark detectors show signal only a factor of ~ 5 below light bolometers of the same frequency band. We expect zero signal in dark detectors and a factor of 100 less signal in eccosorb bolometers compared to light bolometers. These data suggest a sizable level of cross-talk between detectors. Optical cross-talk is expected at only the 1% level, and electrical cross-talk should be negligible. Upcoming measurements are designed to determine the level of optical cross-talk.

Bolometer absorption efficiency

The bolometer absorption efficiency ϵ_b has never been measured for EBEX bolometer wafers and is critical to the noise equivalent temperature (NET) of the telescope. The measured end-to-end receiver efficiency ϵ_r and the calculated optics efficiency ϵ_o can be used to determine ϵ_b since

$$\epsilon_r = \epsilon_o \epsilon_b. \tag{8.10}$$

Because the determination of ϵ_b relies on our calculation of ϵ_o, which has a factor of $\sim$2 uncertainty, we do not expect a high degree of accuracy on the determination of ϵ_b. Nevertheless, the values are still useful to determine roughly how well the bolometers absorb light. Using the weighted mean receiver efficiency of light bolometers and ϵ_o=15, 4, and 3.9%, we find ϵ_b = 118, 45 and 15% for 150, 250 and 410 GHz bands.

The value greater than 100% at 150 GHz suggests that we have under-estimated the transmission at 150 GHz. An alternative explanation is that we used the incorrect responsivity in the ϵ_r measurement determined from the chopped thermal load. Data from Sec. 7.2.4 shows that the measured responsivity is a factor 2, 1.2 and 1.7 higher than predicted by $S_I = 1/v$ at 150, 250 and 410 GHz. If the responsivity in the efficiency measurements is indeed larger by these factors, ϵ_r = 7.8, 1.5 and 0.34% and therefore ϵ_b = 59, 37.5 and 8.8% at 150, 250 and 410 GHz.

Knowledge from other experiments using spider-web, absorber coupled bolometers in conjunction with horn arrays informs us to expect $\epsilon_b \sim 40\%$. We conclude that there are no gross inefficiencies at 150 and 250 GHz. The 410 GHz wafer may suggest low bolometer coupling. Considering all points previously mentioned, 8.8% $< \epsilon_b$(410 GHz) <31%. Low absorption at 410 GHz may result from two factors. One, we use a $3/4\lambda$ back-short due to the prohibitively thin silicon that results from a $1/4\lambda$ back-short. Two, the 117 μm spider-web grid spacing at 410 GHz is a only a factor of six smaller than the wavelength, which may decrease

the absorption. The accurate determination of ϵ_b requires a more controlled optical setup, which is currently being pursued.

8.4 Loading discussion

With estimates of the receiver optics efficiency and bolometer absorption efficiency, we may now explain the results of bolometer loading. Throughout this discussion, we assume $\epsilon_o = 0.15$, 0.04 and 0.039 and $\epsilon_b = 0.6$, 0.4 and 0.2 at 150, 250 and 410 GHz.

We first ask what is the effective blackbody temperature of the aluminum lens cap needed to explain the receiver load configuration, and does this value make sense? The in-band power at the cryostat window is determined by

$$P_{in} = \frac{P_{abs} - P_{emit}\epsilon_b}{\epsilon_r}. \tag{8.11}$$

P_{abs} is the measured power absorbed in the bolometer determined by the mean and variance of the distribution from Table 8.4. P_{emit} is the power emitted by internal emissive components which enters the horn array. This value is calculated in Sec. 8.1.2. And again $\epsilon_r = \epsilon_o\epsilon_b$. We find that the power at the input to the receiver needed to explain the measured load is 61, 55 and 235 pW which corresponds to an effective blackbody temperature of $\sim$ 70 K. The magnitude is plausible given that the beams diverge at the cryostat window. The reflected part of the beam sees a sizable fraction of the 77, 240 and 300 K shells of the cryostat.

Repeating the analysis for flight loading, we find the effective sky temperature needs to be 100 K, 60 K and 75 K at 150, 250 and 410 GHz to explain the power absorbed in the bolometers. In this analysis, we include loading from the telescope primary and secondary mirrors assuming 270 K and an emissivity of 0.5%. Such sky temperatures are unrealistic, especially at balloon altitudes.

A possible explanation is beam size. The loading calculations include the throughput from $8'$ beams at all frequencies. However, Polsgrove shows beam maps produced from ground-based, artificial planet scans in which the main lobe is

$50'$, $33'$ and $20'$ at 150, 250 and 410 GHz [67], substantially larger than designed. If the area stays fixed and the solid angle increases, the larger throughput puts more power on the bolometers for a given sky temperature. If the ground-based beam measurements reflect the in-flight beam size, the effective temperature needed to produce the power absorbed in the bolometers is 6-20 K over the three frequency bands, a plausible sky temperature.

The beam size model is perhaps unphysical. A different explanation is that the thermal emission of the 50 K HWP leaks passed the focal plane low pass filters in the $\sim$ THz range. However, the emissivity of sapphire drastically increases at frequencies higher than $\sim$ 10 THz, beyond the peak emission frequency of a 50 K blackbody. An initial analysis does not explain the level of loading, but the result depends on the assumptions of the filter leak size, which may have been under-estimated.

References

[1] R. A. Alpher, H. Bethe, and G. Gamow. The Origin of Chemical Elements. *Phys Rev*, 73:803–804, April 1948.

[2] G. Gamow. The Origin of Elements and the Separation of Galaxies. *Phys Rev*, 74:505–506, August 1948.

[3] E. Hubble. A Relation between Distance and Radial Velocity among Extra-Galactic Nebulae. *Proceedings of the National Academy of Science*, 15:168–173, March 1929.

[4] D. J. Fixsen, E. S. Cheng, J. M. Gales, J. C. Mather, R. A. Shafer, and E. L. Wright. The Cosmic Microwave Background Spectrum from the Full COBE FIRAS Data Set. *ApJ*, 473:576–+, December 1996, arXiv:astro-ph/9605054.

[5] S. Hanany, P. Ade, A. Balbi, J. Bock, J. Borrill, A. Boscaleri, P. de Bernardis, P. G. Ferreira, V. V. Hristov, A. H. Jaffe, A. E. Lange, A. T. Lee, P. D. Mauskopf, C. B. Netterfield, S. Oh, E. Pascale, B. Rabii, P. L. Richards, G. F. Smoot, R. Stompor, C. D. Winant, and J. H. P. Wu. MAXIMA-1: A Measurement of the Cosmic Microwave Background Anisotropy on Angular Scales of 10'-5′. *ApJ Lett*, 545:L5–L9, December 2000, arXiv:astro-ph/0005123.

[6] S. Padin, J. K. Cartwright, B. S. Mason, T. J. Pearson, A. C. S. Readhead, M. C. Shepherd, J. Sievers, P. S. Udomprasert, W. L. Holzapfel, S. T. Myers, J. E. Carlstrom, E. M. Leitch, M. Joy, L. Bronfman, and J. May. First Intrinsic Anisotropy Observations with the Cosmic Background Imager. *ApJ Lett*, 549:L1–L5, March 2001, arXiv:astro-ph/0012211.

[7] C. B. Netterfield, P. A. R. Ade, J. J. Bock, J. R. Bond, J. Borrill, A. Boscaleri, K. Coble, C. R. Contaldi, B. P. Crill, P. de Bernardis, P. Farese, K. Ganga, M. Giacometti, E. Hivon, V. V. Hristov, A. Iacoangeli, A. H. Jaffe, W. C. Jones, A. E. Lange, L. Martinis, S. Masi, P. Mason, P. D. Mauskopf, A. Melchiorri, T. Montroy, E. Pascale, F. Piacentini, D. Pogosyan, F. Pongetti, S. Prunet, G. Romeo, J. E. Ruhl, and F. Scaramuzzi. A Measurement by BOOMERANG of Multiple Peaks in the Angular Power Spectrum of the Cosmic Microwave Background. *ApJ*, 571:604–614, June 2002, arXiv:astro-ph/0104460.

[8] N. W. Halverson, E. M. Leitch, C. Pryke, J. Kovac, J. E. Carlstrom, W. L. Holzapfel, M. Dragovan, J. K. Cartwright, B. S. Mason, S. Padin, T. J. Pearson, A. C. S. Readhead, and M. C. Shepherd. Degree Angular Scale Interferometer First Results: A Measurement of the Cosmic Microwave Background Angular Power Spectrum. *ApJ*, 568:38–45, March 2002, arXiv:astro-ph/0104489.

[9] A. Benoît, P. Ade, A. Amblard, R. Ansari, É. Aubourg, S. Bargot, J. G. Bartlett, J.-P. Bernard, R. S. Bhatia, A. Blanchard, J. J. Bock, A. Boscaleri, F. R. Bouchet, A. Bourrachot, P. Camus, F. Couchot, P. de Bernardis, J. Delabrouille, F.-X. Désert, O. Doré, M. Douspis, L. Dumoulin, X. Dupac, P. Filliatre, P. Fosalba, K. Ganga, F. Gannaway, B. Gautier, M. Giard, Y. Giraud-Héraud, R. Gispert, L. Guglielmi, J.-C. Hamilton, S. Hanany, S. Henrot-Versillé, J. Kaplan, G. Lagache, J.-M. Lamarre, A. E. Lange, J. F. Macías-Pérez, K. Madet, B. Maffei, C. Magneville, D. P. Marrone, S. Masi, F. Mayet, A. Murphy, F. Naraghi, F. Nati, G. Patanchon, G. Perrin, M. Piat, N. Ponthieu, S. Prunet, J.-L. Puget, C. Renault, C. Rosset, D. Santos, A. Starobinsky, I. Strukov, R. V. Sudiwala, R. Teyssier, M. Tristram, C. Tucker, J.-C. Vanel, D. Vibert, E. Wakui, and D. Yvon. The cosmic microwave background anisotropy power spectrum measured by Archeops. *Ast & Astphy*, 399:L19–L23, March 2003, arXiv:astro-ph/0210305.

[10] M. R. Nolta, M. J. Devlin, W. B. Dorwart, A. D. Miller, L. A. Page, J. Puchalla, E. Torbet, and H. T. Tran. The MAT/TOCO Measurement of the Angular Power Spectrum of the Cosmic Microwave Background at 30 and 40 GHz. *ApJ*, 598:97–101, November 2003.

[11] C. L. Kuo, P. A. R. Ade, J. J. Bock, C. Cantalupo, M. D. Daub, J. Goldstein, W. L. Holzapfel, A. E. Lange, M. Lueker, M. Newcomb, J. B. Peterson, J. Ruhl, M. C. Runyan, and E. Torbet. High-Resolution Observations of the Cosmic Microwave Background Power Spectrum with ACBAR. *ApJ*, 600:32–51, January 2004, arXiv:astro-ph/0212289.

[12] M. R. Nolta, J. Dunkley, R. S. Hill, G. Hinshaw, E. Komatsu, D. Larson, L. Page, D. N. Spergel, C. L. Bennett, B. Gold, N. Jarosik, N. Odegard, J. L. Weiland, E. Wollack, M. Halpern, A. Kogut, M. Limon, S. S. Meyer, G. S. Tucker, and E.L. Wright. Five-Year Wilkinson Microwave Anisotropy Probe (WMAP) Observations: Angular Power Spectra. *ApJ Sup*, 180:296–305, February 2009, 0803.0593.

[13] J. Dunkley, E. Komatsu, M. R. Nolta, D. N. Spergel, D. Larson, G. Hinshaw, L. Page, C. L. Bennett, B. Gold, N. Jarosik, J. L. Weiland, M. Halpern, R. S. Hill, A. Kogut, M. Limon, S. S. Meyer, G. S. Tucker, E. Wollack, and E. L. Wright. Five-Year Wilkinson Microwave Anisotropy Probe (WMAP) Observations: Likelihoods and Parameters from the WMAP data. *ApJ Sup*, 180:306–376, February 2009, 0803.0586.

[14] A. H. Guth. Inflationary universe: A possible solution to the horizon and flatness problems. *Phys Rev D*, 23:347–356, January 1981.

[15] A. A. Starobinsky. A new type of isotropic cosmological models without singularity. *Phys Lett B*, 91:99–102, March 1980.

[16] S. W. Hawking. The development of irregularities in a single bubble inflationary universe. *Phys Lett B*, 115:295–297, September 1982.

[17] J. M. Bardeen, P. J. Steinhardt, and M. S. Turner. Spontaneous creation of almost scale-free density perturbations in an inflationary universe. *Phys Rev D*, 28:679–693, August 1983.

[18] A. Albrecht and P. J. Steinhardt. Cosmology for grand unified theories with radiatively induced symmetry breaking. *Phys Rev Lett*, 48:1220–1223, April 1982.

[19] A. A. Starobinsky. Dynamics of phase transition in the new inflationary universe scenario and generation of perturbations. *Phys Lett B*, 117:175–178, November 1982.

[20] W. H. Kinney. The energy scale of inflation: is the hunt for the primordial B-mode a waste of time? *New Astr Rev*, 47:967–975, December 2003, arXiv:astro-ph/0307005.

[21] U. Seljak and M. Zaldarriaga. Signature of Gravity Waves in the Polarization of the Microwave Background. *Phys Rev Lett*, 78:2054–2057, March 1997, arXiv:astro-ph/9609169.

[22] M. J. Rees. Polarization and Spectrum of the Primeval Radiation in an Anisotropic Universe. *ApJ Lett*, 153:L1+, July 1968.

[23] M. Zaldarriaga and U. Seljak. All-sky analysis of polarization in the microwave background. *Phys Rev D*, 55:1830–1840, February 1997, arXiv:astro-ph/9609170.

[24] J. M. Kovac, E. M. Leitch, C. Pryke, J. E. Carlstrom, N. W. Halverson, and W. L. Holzapfel. Detection of polarization in the cosmic microwave background using DASI. *Nature*, 420:772–787, December 2002, arXiv:astro-ph/0209478.

[25] A. C. S. Readhead, S. T. Myers, T. J. Pearson, J. L. Sievers, B. S. Mason, C. R. Contaldi, J. R. Bond, R. Bustos, P. Altamirano, C. Achermann, L. Bronfman, J. E. Carlstrom, J. K. Cartwright, S. Casassus, C. Dickinson, W. L. Holzapfel, J. M. Kovac, E. M. Leitch, J. May, S. Padin, D. Pogosyan, M. Pospieszalski, C. Pryke, R. Reeves, M. C. Shepherd, and S. Torres. Polarization Observations with the Cosmic Background Imager. *Science*, 306:836–844, October 2004, arXiv:astro-ph/0409569.

[26] W. C. Jones, P. A. R. Ade, J. J. Bock, J. R. Bond, J. Borrill, A. Boscaleri, P. Cabella, C. R. Contaldi, B. P. Crill, P. de Bernardis, G. De Gasperis, A. de Oliveira-Costa, G. De Troia, G. di Stefano, E. Hivon, A. H. Jaffe, T. S. Kisner, A. E. Lange, C. J. MacTavish, S. Masi, P. D. Mauskopf, A. Melchiorri, T. E. Montroy, P. Natoli, C. B. Netterfield, E. Pascale, F. Piacentini, D. Pogosyan, G. Polenta, S. Prunet, S. Ricciardi, G. Romeo, J. E. Ruhl, P. Santini, M. Tegmark, M. Veneziani, and

N. Vittorio. A Measurement of the Angular Power Spectrum of the CMB Temperature Anisotropy from the 2003 Flight of BOOMERANG. *ApJ*, 647:823–832, August 2006, arXiv:astro-ph/0507494.

[27] J. H. P. Wu, J. Zuntz, M. E. Abroe, P. A. R. Ade, J. Bock, J. Borrill, J. Collins, S. Hanany, A. H. Jaffe, B. R. Johnson, T. Jones, A. T. Lee, T. Matsumura, B. Rabii, T. Renbarger, P. L. Richards, G. F. Smoot, R. Stompor, H. T. Tran, and C. D. Winant. Maxipol: Data analysis and results. *ApJ*, 665(1):55–66, 2007, arXiv:astro-ph/0611392.

[28] C. Bischoff, L. Hyatt, J. J. McMahon, G. W. Nixon, D. Samtleben, K. M. Smith, K. Vanderlinde, D. Barkats, P. Farese, T. Gaier, J. O. Gundersen, M. M. Hedman, S. T. Staggs, and B. Winstein. New Measurements of Fine-Scale CMB Polarization Power Spectra from CAPMAP at Both 40 and 90 GHz. *ApJ*, 684:771–789, September 2008, 0802.0888.

[29] H. C. Chiang, P. A. R. Ade, D. Barkats, J. O. Battle, E. M. Bierman, J. J. Bock, C. D. Dowell, L. Duband, E. F. Hivon, W. L. Holzapfel, V. V. Hristov, W. C. Jones, B. G. Keating, J. M. Kovac, C. L. Kuo, A. E. Lange, E. M. Leitch, P. V. Mason, T. Matsumura, H. T. Nguyen, N. Ponthieu, C. Pryke, S. Richter, G. Rocha, C. Sheehy, Y. D. Takahashi, J. E. Tolan, and K. W. Yoon. Measurement of CMB Polarization Power Spectra from Two Years of BICEP Data. *ArXiv e-prints*, June 2009, 0906.1181.

[30] C. Pryke, P. Ade, J. Bock, M. Bowden, M. L. Brown, G. Cahill, P. G. Castro, S. Church, T. Culverhouse, R. Friedman, K. Ganga, W. K. Gear, S. Gupta, J. Hinderks, J. Kovac, A. E. Lange, E. Leitch, S. J. Melhuish, Y. Memari, J. A. Murphy, A. Orlando, R. Schwarz, C. O. Sullivan, L. Piccirillo, N. Rajguru, B. Rusholme, A. N. Taylor, K. L. Thompson, A. H. Turner, E. Y. S. Wu, and M. Zemcov. Second and Third Season QUaD Cosmic Microwave Background Temperature and Polarization Power Spectra. *ApJ*, 692:1247–1270, February 2009.

[31] L. Knox and Y.-S. Song. Limit on the Detectability of the Energy Scale of Inflation. *Phys Rev Lett*, 89(1):011303–+, July 2002, arXiv:astro-ph/0202286.

[32] E. Komatsu, J. Dunkley, M. R. Nolta, C. L. Bennett, B. Gold, G. Hinshaw, N. Jarosik, D. Larson, M. Limon, L. Page, D. N. Spergel, M. Halpern, R. S. Hill, A. Kogut, S. S. Meyer, G. S. Tucker, J. L. Weiland, E. Wollack, and E. L. Wright. Five-Year Wilkinson Microwave Anisotropy Probe (WMAP) Observations: Cosmological Interpretation. *ApJ Sup*, 180:330–376, February 2009, 0803.0547.

[33] K. M. Smith, W. Hu, and M. Kaplinghat. Weak lensing of the CMB: Sampling errors on B modes. *Phys Rev D*, 70(4):043002–+, August 2004, arXiv:astro-ph/0402442.

[34] Arthur Kosowsky and Michael S. Turner. Cbr anisotropy and the running of the scalar spectral index. *Phys Rev D*, 52(4):R1739–R1743, Aug 1995.

[35] B. R. Johnson, J. Collins, M. E. Abroe, P. A. R. Ade, J. Bock, J. Borrill, A. Boscaleri, P. de Bernardis, S. Hanany, A. H. Jaffe, T. Jones, A. T. Lee, L. Levinson, T. Matsumura, B. Rabii, T. Renbarger, P. L. Richards, G. F. Smoot, R. Stompor, H. T. Tran, C. D. Winant, J. H. P. Wu, and J. Zuntz. Maxipol: Cosmic microwave background polarimetry using a rotating half-wave plate. *ApJ*, 665(1):42–54, 2007, arXiv:astro-ph/0611394.

[36] N. Schneider, Joachim Urban, and P. Baron. Potential of radiotelescopes for atmospheric line observations: I. observation principles and transmission curves for selected sites. *Planetary and Space Science*, 57:1419–1433, 2009.

[37] S. Chase. *Two-stage sub-Kelvin ^3He cooler*. Chase Research Cryogenics Ltd., 140 Manchester Road, Sheffield S10 5DL, England.

[38] S. Hanany, J. Hubmayr, B. R. Johnson, T. Matsumura, P. Oxley, and M. Thibodeau. Millimeter-wave achromatic half-wave plate. *Appl Opt*, 44:4666–4670, August 2005, arXiv:physics/0503122.

[39] T. Matsumura, S. Hanany, B. R. Johnson, T. J. Jones, and P. Jonnalagadda. Analysis of performance of three- and five-stack achromatic half-wave plates at millimeter wavelengths. *ArXiv e-prints*, June 2008, 0806.1518.

[40] S. Hanany, T. Matsumura, B. Johnson, T. Jones, J. R. Hull, and K. B. Ma. A Cosmic Microwave Background Radiation Polarimeter Using Superconducting Bearings. *IEEETAS*, pages 2128–2133, April 2003, arXiv:astro-ph/0304312.

[41] Peter A.R. Ade, Giampoalo Pisano, Carole Tucker, and Samuel Weaver. A review of metal mesh filters. *SPIEMM*, 6275, 2006.

[42] K. D. Irwin, G. C. Hilton, D. A. Wollman, and J. M. Martinis. Thermal-response time of superconducting transition-edge microcalorimeters. *J Appl Phys*, 83:3978–3985, April 1998.

[43] M. E. Huber, P. A. Neil, R. G. Benson, D. A. Burns, A. M. Corey, C. S. Flynn, Y.Kitaygorodskaya, O. Massihzadeh, J. M. Martinis, and G. C. Hilton. DC SQUID series array amplifiers with 120 MHz bandwidth (corrected). *IEEE Trans Appl Sup*, 11(2):4048–4053, 2001.

[44] M. Dobbs, E. Bissonnette, and H. Spieler. Digital Frequency Domain Multiplexer for Millimeter-Wavelength Telescopes. *IEEE Trans on Nucl Sci*, 55:21–26, 2008, 0708.2762.

[45] S. Lee, J. M. Gildemeister, W. Holmes, A. T. Lee, and P. L. Richards. Voltage-biased superconducting transition-edge bolometer with strong electrothermal feedback operated at 370 mK. *Appl Opt*, 37:3391–3397, 1998.

[46] S.P. Langley. The bolometer. *Nature*, 25(14), 1881.

[47] K. D. Irwin. An application of electrothermal feedback for high resolution cryogenic particle detection. *Appl Phys Lett*, 60(15):1998–2000, Apr 1995.

[48] K.D. Irwin and Hilton G. Cryogenic particle detection. *Top. Appl. Phys.*, pages 63–150, 2005.

[49] M. Razeti. A large signal analysis for transition edge sensors operating in electrothermal feedback. *Nuc Inst & Meth in Phys A*, 556:209–214, 2006.

[50] K. Rostem, S. Withington, and D. J. Goldie. Multitone large-signal analysis of superconducting transition-edge sensors for astronomy. *J Appl Phys*, 102(3):034511–+, August 2007.

[51] J.C. Mather. Bolometer noise: nonequilibrium theory. *Appl Opt*, 21(6):1125–1129, 1982.

[52] P. L. Richards. Bolometers for infrared and millimeter waves. *J Appl Phys*, 76:1–24, July 1994.

[53] B.D. Josephson. Possible new effects in superconductive tunneling. *Phys. Lett.*, 1:251, 1962.

[54] B.D. Josephson. Coupled superconductors. *Adv. in Phys.*, 14:419, 1965.

[55] Michael Tinkham. *Introduction to Superconductivity.* Dover Publications, Inc., Mineola, NY, 2nd, edition, 1996.

[56] W.C. Stewart. Current-voltage characteristics of josephson junctions. *Appl Phys Lett*, 12:277, 1968.

[57] D.E. McCumber. Effect of ac impedance on dc voltage-current characteristics of superconductor weak-link junctions. *J Appl Phys*, 39:3113, 1968.

[58] Charles Kittel. *Introduction to Solid State Physics.* John Wiley and Sons, Inc., Hoboken, NJ, 7th, edition, 1996.

[59] T. M. Lanting. *Multiplexed readout of superconducting bolometers for cosmological observations.* PhD thesis, AA(University of California, Berkeley), 2006.

[60] T. M. Lanting, K. Arnold, H.-M. Cho, J. Clarke, M. Dobbs, W. Holzapfel, A. T. Lee, M. Lueker, P. L. Richards, A. D. Smith, and H. G. Spieler. Frequency-domain readout multiplexing of transition-edge sensor arrays. *Nucl Inst and Meth in Phys Research A*, 559:793–795, April 2006.

[61] T. M. Lanting, H.-M. Cho, J. Clarke, W. L. Holzapfel, A. T. Lee, M. Lueker, P. L. Richards, M. A. Dobbs, H. Spieler, and A. Smith. Frequency-domain multiplexed readout of transition-edge sensor arrays with a superconducting quantum interference device. *Appl Phys Lett*, 86(11):112511–+, March 2005.

[62] T. M. Lanting, H.-M. Cho, J. Clarke, M. Dobbs, A. T. Lee, M. Lueker, P. L. Richards, A. D. Smith, and H. G. Spieler. Frequency domain multiplexing for

bolometer arrays. *Nucl Inst and Meth in Phys Research A*, 520:548–550, March 2004.

[63] T. M. Lanting, H.-M. Cho, J. Clarke, M. Dobbs, A. T. Lee, P. L. Richards, H. Spieler, and A. Smith. Frequency-domain multiplexing for large-scale bolometer arrays. In T. G. Phillips & J. Zmuidzinas, editor, *Society of Photo-Optical Instrumentation Engineers (SPIE) Conference Series*, volume 4855 of *Presented at the Society of Photo-Optical Instrumentation Engineers (SPIE) Conference*, pages 172–181, February 2003.

[64] T. M. Lanting, H. Cho, J. Clarke, M. Dobbs, A. T. Lee, P. L. Richards, A. D. Smith, and H. G. Spieler. A frequency-domain squid multiplexer for arrays of transition-edge superconducting sensors. *IEEE Trans Appl Sup*, 13(2):626, 2003.

[65] K. MacDermid, P. Hyland, F. Aubin, E. Bissonnette, M. Dobbs, J. Hubmayr, G. Smecher, and S. Warraich. Tuning of Kilopixel Transition Edge Sensor Bolometer Arrays with a Digital Frequency Multiplexed Readout System. *ArXiv e-prints*, November 2009, 0911.4448.

[66] T.M. Lanting. private communication, 2006.

[67] D.E. Polsgrove. *Calibration of the E and B EXperiment, A Balloon-Borne Cosmic Microwave Background Polarimeter*. PhD thesis, AA(University of Minnesota, Twin Cities), 2009.

[68] J. Hubmayr, F. Aubin, E. Bissonnette, M. Dobbs, S. Hanany, A. T. Lee, K. MacDermid, X. Meng, I. Sagiv, and G. Smecher. Design and characterization of TES bolometers and SQUID readout electronics for a balloon-borne application. In *Society of Photo-Optical Instrumentation Engineers (SPIE) Conference Series*, volume 7020 of *Presented at the Society of Photo-Optical Instrumentation Engineers (SPIE) Conference*, August 2008, 0908.1997.

[69] W. Holmes, J. M. Gildemeister, P. L. Richards, and V. Kotsubo. Measurements of thermal transport in low stress silicon nitride films. *Appl Phys Lett*, 72:2250–+, May 1998.

[70] Panasonic. *ECJ series*.

[71] H. Spieler. Frequency domain multiplexing for large scale bolometer arrays. *Monterey Far-IR, Sub-mm and mm Detector Technology Workshop proceedings*, pages 243–249, 2002.

[72] A. T. Lee, P. L. Richards, S. W. Nam, B. Cabrera, and K. D. Irwin. A superconducting bolometer with strong electrothermal feedback. *Appl Phys Lett*, 69(12):1801–1803, 1996.

[73] H. B. G. Casimir. Note on the conduction of heat in crystals. *Physica*, 5:495–500, June 1938.

[74] M. Lueker, B. A. Benson, C. L. Chang, H.-M. Cho, M. Dobbs, W. L. Holzapfel, T. Lanting, A. T. Lee, J. Mehl, T. Plagge, E. Shirokoff, H. G. Spieler, and J. D. Vieira. Thermal Design and Characterization of Transition-Edge Sensor (TES) Bolometers for Frequency-Domain Multiplexing. *IEEE Trans Appl Sup*, 19:496–500, June 2009.

[75] J. W. Lamb. Miscellaneous data on materials for millimetre and submillimetre optics. *International Journal of Infrared and Millimeter Waves*, 17:1997–2034, December 1996.

[76] C. E. Tucker and P. A. R. Ade. Thermal filtering for large aperture cryogenic detector arrays. In *Society of Photo-Optical Instrumentation Engineers (SPIE) Conference Series*, volume 6275 of *Presented at the Society of Photo-Optical Instrumentation Engineers (SPIE) Conference*, July 2006.

[77] J. B. Peterson and P. L. Richards. A cryogenic blackbody for millimeter wavelengths. *International Journal of Infrared and Millimeter Waves*, 5:1507–1515, December 1984.

[78] A.R. Kerr, N.J. Bailey, D.E. Boyd, and N. Horner. A study of materials for a braodband millimeter-wave quasi-optical vacuum window. *Electronics Division Internal Report No. 292*, August 1992.

Appendix A

NAF detector configuration

Table A.1 tallies the number of live bolometers for the NAF in each category.

ν_c	light	dark	eccosorb	resistor
150	64	9	3	3
250	32	11	4	3
410	71	2	6	2
total	167	22	13	8

Table A.1: Number of live bolometers for the NAF determined from ground-based measurements during the field campaign.

Dark bolometers have 2 mil Al tape covering the waveguide exit aperture. Six bolometers on each wafer had MF-110 eccosorb plugs inserted into the horn array directly above the detector in order to attenuate 99% of the signal for ground based testing during the field campaign. Three 1 Ω resistor channels per wafer were soldered on the LC board electrically in place of the bolometer for systematic error checks. The bolometer position of these special bolometers is listed in Table A.2.

The bolometer position labeling scheme is:

$$< \text{frequency band} >< \text{row} >< \text{column} >$$

as viewed with the wire-bonding pads facing down.

dark	eccosorb	resistor
150-06-13	150-03-05	150-07-01
150-08-13	150-04-07	150-08-05
150-12-03	150-06-10	150-13-02
150-12-04	150-08-04	250-07-01
150-12-06	150-08-10	250-08-05
150-12-07	150-09-03	250-13-02
150-12-08	250-03-09	410-07-01
150-12-09	250-04-07	410-08-05
150-13-05	250-04-10	410-13-02
150-13-06	250-08-10	
150-13-07	250-09-04	
150-14-04	250-10-08	
150-14-05	410-02-02	
250-12-06	410-05-02	
250-12-07	410-05-10	
250-12-08	410-08-06	
250-12-09	410-08-10	
250-13-05	410-12-04	
250-13-06		
250-13-07		
250-13-08		
250-14-01		
250-14-04		
250-14-05		
410-11-01		
410-11-02		
410-12-02		
410-13-01		
410-14-01		

Table A.2: Dark and eccosorb bolometers in the NAF

Appendix B

Transfer functions

B.1 Mixer Transfer functions

The digital demodulator of the DfMUX uses a mixer to transfer signals down to base band. Noise and signal transfer differently through the demodulator, which must be accounted for when determining the noise equivalent power of the bolometers. As an example, consider a square wave mixer in which for half a period of the mixer frequency the pre-demodulated signal is multipled by +1 and the other half by -1. The rms of broadband noise σ_{rms} is unchanged by this multiplication, and hence the mixer transfer function is unity. However, sky signals are modulations of the carrier amplitude A_c, which transfers through the mixer as

$$\frac{1}{2\pi}\int_0^{\pi} +1 \times A_c \sin\theta \, d\theta + \int_{\pi}^{2\pi} -1 \times A_c \sin\theta \, d\theta = \frac{2}{\pi} A_c. \tag{B.1}$$

We see that signals get multipled by $2/\pi$ through the square wave mixer.

Early firmware version of the DfMUX demodulator used a square wave mixer, and current versions (such as the NAF version) use a pseudo-sine wave mixer. Table B.1 lists the transfer function through both sine wave and square wave demodulators for signal, broadband noise and narrow band noise. Narrow band noise sources refer to noise sources which are attenuated by the LC filter in series

with the bolometer.

source	example	square wave	sine wave
signal	sky signal	$2/\pi$	$A_c/2$
broadband noise	SQUID noise	1	$A_c/\sqrt{2}$
narrow band noise	bolometer Johnson	$2/\pi$	$A_c/\sqrt{2}$

Table B.1: Transfer functions through a square and sine wave demodulator. A_c is the amplitude of the carrier wave input to the demodulator.

B.2 DfMUX conversions

B.2.1 Voltage bias

The following equation is used to convert the DfMUX carrier settings to voltage across the bolometer for the rev.3 mezzanine with 16 channel firmware,

$$v = a \times \frac{dv}{da}\frac{G(0)}{G(x)}\frac{R_b}{200\Omega + R_x}.$$

a is the percent of full scale carrier setting, $\frac{dv}{da}$ converts the carrier amplitude setting to voltage across a 100Ω load, $G(x)$ is the mezzanine gain setting, $R_b = 0.03\Omega$ is the bias resistor in parallel with the TES and R_x is the 300 K to 4 K stray wiring resistance. $\frac{dv}{da}$ is determined from a calibration. Table B.2 lists full scale voltage bias for the four gain settings.

	$G(0)$	$G(1)$	$G(2)$	$G(3)$
v (μV_{rms})	0.71	1.59	4.80	13.86

Table B.2: Voltage bias across the full scale amplitude setting for DfMUX mezzanine rev 3, 16 channel firmware assuming $R_b = 0.03\Omega$ and $R_x = 10\Omega$.

B.2.2 Current conversion

The number of demodulator counts *cnt* for the current I at the SQUID input coil is determined by

$$\frac{d(cnt)}{dA} = Z_{trans} G_2 \frac{G(x)}{G(0)} \frac{d(cnt)}{dv}.$$

Z_{trans} is the SQUID feedback loop transimpedence ($Z_{trans} = -R_{fb}$ for high SQUID loopgain), G_2 is the gain of the 2^{nd} stage amplifier on the SQUID controller board, $G(x)$ is a selectable demodulator gain on the DfMUX mezzanine and $\frac{d(cnt)}{dv}$ converts the voltage to demodulator counts. This factor is determined from a calibration and includes gain factors in the DfMUX demodulator chain before digitization and the mixer transfer function. Table B.3 lists the conversion factors for each gain setting determined from a calibration and assuming $Z_{trans} = 5\ k\Omega$.

To convert the current at the SQUID coil to power absorbed in the bolometer, divide the current by the bolometer responsivity. In the limit of high TES loopgain, $S_I = 1/v$, and the current at the SQUID coil is multipled by the bolometer voltage bias in order to obtain the power absorbed in the bolometer.

	G(0)	G(1)	G(2)	G(3)
$\frac{dA}{d(cnt)}$ (pA)	2792	573	83.4	29.3

Table B.3: Demodulator count to current at the SQUID coil conversion factors for each gain setting assuming $Z_{trans} = 5k\Omega$.

Appendix C

NIST series array SQUIDs

Table C.1 lists the NIST 8-turn series array SQUID parameters. These are the SQUIDs used in EBEX.

parameter	value
L_{in}	160 nH
M	$1\phi_o/26\mu A$
I_c	85 μA
R_n	80 Ω
V_{pp}	4 mV_{pp}
WNL	2.5 $pA_{rms}/\sqrt{Hz}$

Table C.1: NIST 100 series array SQUID parameters. L_{in}, M, I_c, R_n and V_{pp} are the input coil inductance, mutual inductance critial current, normal resistance and peak to peak voltage of the V-ϕ curve respectively.